

Real light curves of FK Comae Berenices: Farewell flip-flop^{*}

L. Jetsu

Department of Physics, P.O. Box 64, FI-00014 University of Helsinki, Finland (e-mail: lauri.jetsu@helsinki.fi)

Received / Accepted

ABSTRACT

Context. For seven decades, the widely held view has been that the formation, the migration and the decay of short-lived starspots explain the observed constantly changing photometric light curves of chromospherically active stars.

Aims. We argue that these observed deceptive light curves are interference of two real constant period light curves of long-lived starspots. The relative slow motion of these long-lived starspots with respect to each other causes the observed light curve changes. In the end of our Introduction, we make six specific questions which undermine our argument, because it contradicts the current views about stellar surface differential rotation and starspots in general. Our main aim is to answer these six questions. The surface images and the light curves are used to estimate the surface differential rotation of chromospherically active stars. These two approaches give contradicting results even for the same individual star. We aim to solve this problem for good. Our last aim is to model the puzzling light curves of FK Com.

Methods. We formulate a period finding method that detects the two real light curves behind the observed light curve.

Results. We solve the real light curves of FK Com. The long-lived structure predicted by our argument is present on the surface of FK Com. The two periodicities of this structure are also present in the long-term mean light curves of FK Com. We show that the one-dimensional period finding methods, like the Lomb-Scargle periodogram, give spurious results because a simple sinusoid is an incompatible model for the light curves of chromospherically active stars.

Conclusions. We begin our Conclusions by giving compact answers to all the above mentioned six specific questions. Our argument explains numerous spurious phenomena: the observed rapid light curve changes, the short starspot life-times, the rapid rotation period changes, the active longitudes, the starspot migration, the period cycles, the amplitude cycles and the minimum epoch cycles. It also explains why the surface images and the light curves give contradicting surface differential rotation estimates even for the same individual star, as well as the abrupt 180 degrees shifts of activity (the flip-flop events) and the long-term mean light curves. We argue that the current views of starspots need to be revised.

Key words. Methods: statistical, data analysis, Stars: starspots, activity, individual: FK Comae Berenices (HD117555)

1. Introduction

The ancient Egyptian papyrus Cairo 86637, which contains the calendar of lucky and unlucky days, is the oldest preserved historical document of the discovery of a variable star, Algol (Porceddu et al. 2008; Jetsu et al. 2013; Jetsu & Porceddu 2015; Porceddu et al. 2018). The Sun is also a variable star. The luminosity changes of Algol can be observed with naked eye, but those of the Sun can be reliably confirmed only with satellite observations (Willson & Hudson 1991; Radick et al. 2018). The oldest preserved drawing of a sunspot was made by John of Worcester in the year 1128 (Van Helden 1996). Schwabe (1844) discovered the eleven years cycle in the number of sunspots. The Zeeman effect caused by the solar magnetic field was discovered by Hale (1908), who also found out that this magnetic field is stronger in the sunspots.

Kron (1947) discovered the starspots in the light curves of the eclipsing binary AR Lacertae. He observed short-term light curve changes “within a few weeks to a few months”. FK Comae Berenices (HD 117555, FK Com) was among the first late-type stars where the starspots were also discovered (Chugainov 1966). This chromospherically active single G4 giant (Strassmeier 2009) is the prototype

of a class of variable stars, the FK Com class, defined by Bopp & Stencel (1981) as rapidly rotating single G–K giants. Only a few stars belonging to this class have been found (Puzin et al. 2014; Howell et al. 2016; Puzin et al. 2017). The members of this class may represent recently coalesced W UMa binaries (Webbink 1976; Bopp & Stencel 1981; Eggen & Iben 1989; Welty & Ramsey 1994).

The starspots on the surface of FK Com seem to concentrate on two long-lived active longitudes separated by 180 degrees, and undergo abrupt shifts between these longitudes. These shifts are called the flip-flop events (Jetsu et al. 1991, 1993). This phenomenon has also been observed in the chromospherically active binaries (e.g. Jetsu 1996, σ Gem). Hackman et al. (2013) applied the Kuiper method (hereafter the K-method) to the seasonal light curve minimum epochs of FK Com. This analysis gave the active longitude period $P_{\text{act}} = 2.^{\text{d}}401155 \pm 0.^{\text{d}}000092$. Numerous photometric studies of FK Com have been made (e.g. Korhonen et al. 2002; Oláh et al. 2006; Panov & Dimitrov 2007; Hackman et al. 2013). The starspot distribution of FK Com has also been mapped with the surface imaging methods (e.g. Korhonen et al. 1999, 2000, 2004, 2007, 2009; Hackman et al. 2013; Vida et al. 2015).

Jetsu et al. (2017) presented a general light curve model for the Chromospherically Active Binary Stars (hereafter CABS). They studied the long-term Mean Light Curve (hereafter MLC) of fourteen CABSs as a function of orbital

^{*} Table 3 is only available via anonymous ftp to cdsarc.u-strasbg.fr (130.79.128.5) or via <http://cdsarc.u-strasbg.fr/viz-bin/qcat?J/A+A/...>

phase, and also showed how their new model can be applied to the photometry of Chromospherically Active Single Stars (hereafter CASS), like FK Com. Here, we present an improved period analysis method based on this model, and apply this new method to the photometry of FK Com.

Jetsu et al. (2017, JHL = Jetsu, Henry, Lehtinen) made the following argument

JHL-argument: “The *observed* light curves of chromospherically active binary and single stars are interference of two *real* constant period light curves of long-lived starspots. These constant periods are the non-stationary active longitude period P_{act} and the stationary rotation period $P_{\text{rot}} \approx P_{\text{orb}}$.”

At first sight, this JHL-argument would seem to contradict the current overwhelming observational evidence for stellar Surface Differential Rotation (hereafter SDR). There are two widely used observational methods for measuring stellar SDR (Strassmeier 2009, Sect. 7). In the first method, the rotation periods P_{rot} of starspots at different latitudes are measured from the Surface Images (hereafter the SI-method, e.g. Petit et al. 2004; Barnes et al. 2005; Collier Cameron 2007; Strassmeier 2009; Balona & Abedigamba 2016; Kővári et al. 2017). The second method measures the range of the photometric rotation period $P_{\text{phot}} \approx P_{\text{rot}}$ changes in the Light Curves (hereafter the LC-method, e.g. Hall & Busby 1990; Hall 1991; Reinhold & Reiners 2013; Reinhold et al. 2013; Reinhold & Gizon 2015; Lehtinen et al. 2016; Distefano et al. 2016). There are numerous studies, where the SI-method and the LC-method give *different* SDR estimates even for the *same* individual star. For example, the SI-method study by Korhonen et al. (2000) indicated “solid body rotation” in FK Com, but photometric rotation period changes of about 3.1% were measured with the LC-method by Hackman et al. (2013, $Z \approx 0.0308$).

If the JHL-argument is true, then we must be able to answer at least five of the six undermining questions made below. The validity our argument does not depend on the *3rd question*. On the contrary, the JHL-argument provides an answer to this question.

In our Abstract, we refer to these six specific questions:

- *1st question*: Why have these two constant periods, the non-stationary active longitude period P_{act} and the stationary rotation period $P_{\text{rot}} \approx P_{\text{orb}}$ of the JHL-argument, *not* been detected in the surface images?
- *2nd question*: Why have these two constant periods, the non-stationary active longitude period P_{act} and the stationary rotation period $P_{\text{rot}} \approx P_{\text{orb}}$ of the JHL-argument, *not* been detected in the light curves? Why are so *many different* $P_{\text{rot}} \approx P_{\text{phot}}$ periods *observed* in the light curves of the *same* star, if the photometric data contains only these two constant periods?
- *3rd question*: Why do the surface images and the light curves give *different* surface differential rotation estimates even for the *same* individual star?
- *4th question*: Hackman et al. (2013) applied the Kuiper method to the $t_{\text{min},1}$ light curve minima of FK Com. Does this kind of an analysis give an *unambiguous* estimate for the non-stationary active longitude period P_{act} of the JHL-argument?
- *5th question*: The Kuiper method detects the non-stationary active longitude period P_{act} of the JHL-argument from the seasonal $t_{\text{min},1}$ light curve minima

of chromospherically active binary stars (Jetsu et al. 2017) and single stars (Hackman et al. 2013). Why does this method *not* detect the stationary rotation period $P_{\text{rot}} \approx P_{\text{orb}}$ of the JHL-argument? The long-term mean light curves of chromospherically active binary stars in Jetsu et al. (2017) follow the stationary rotation period $P_{\text{rot}} \approx P_{\text{orb}}$ of the JHL-argument. Why do these long-term mean light curves *not* follow the non-stationary active longitude period P_{act} of the JHL-argument?

- *6th question*: What explains the observed *abrupt* flip-flop events in the chromospherically active stars, if the long-lived starspots rotate with the two *regular constant* periods, the non-stationary active longitude period P_{act} and the stationary rotation period $P_{\text{rot}} \approx P_{\text{orb}}$?

We will answer these six questions. The compact answers are given in the beginning of our Conclusions (Sect. 17).

Our abbreviations are

- K-method: Kuiper method (Sect. 1)
- CABS: Chromospherically Active Binary Star (Sect. 1)
- MLC: Mean Light Curve (Sect. 1)
- CASS: Chromospherically Active Single Star (Sect. 1)
- SDR: Surface Differential Rotation (Sect. 1)
- JHL-argument: Jetsu et al. (2017) argument (Sect. 1)
- SI-method: Surface Images measure SDR (Sect. 1)
- LC-method: Light Curves measure SDR (Sect. 1)
- CPS-method: Continuous Period Search method (Sect. 2)
- CPS-model: Continuous Period Search model (Sect. 2)
- 2P-model: Two Period model (Sect. 3.1)
- 1P-model: One Period model (Sect. 3.2)
- LS-method: Lomb-Scargle method (Sect. 7)
- LS-model: Lomb-Scargle model (Sect. 7)
- TEST $_{a_1=a_2}$: 2P-model test $A_1 = A_2$ (Sect. 7.3.1)
- TEST $_{a_1 < a_2}$: 2P-model test $A_1 < A_2$ (Sect. 7.3.2)
- 2P-method: Two period method (Sect. 8.1)
- 1P-method: One period method (Sect. 8.2)
- WK-method: Weighted Kuiper method (Sect. 11)

We introduce these abbreviations in the sections given above in the parenthesis. Except for the JHL-argument abbreviation, we do not use any other abbreviations in our six specific questions or in our answers to these six questions, because this makes our Introduction (Sect. 1) and Conclusions (Sect. 17) easier to read.

2. Data

We analyse the standard Johnson V photometry of FK Com published by Hackman et al. (2013). These observations were made with the “T7” and “Ph10” telescopes. We denote these separate samples of observations with TEL=1 (“T7”) and TEL=2 (“Ph10”). Hackman et al. (2013) stored them as two separate files into the CDS database. We analyse these two files separately, to avoid bias, as Hackman et al. (2013) also did. The accuracy of this photometry is between 0.^m004 and 0.^m008 in good photometric nights (Henry 1995; Strassmeier et al. 1997). All observations where the standard deviation of three measurements exceeds 0.^m020 are automatically discarded.

We discard $n = 68$ observations (Table 1). The number of remaining analysed observations is $n = 3807$.

The *isolated* first segment of TEL=2 data in Hackman et al. (2013) contains too few observations for reliable modelling, and it is discarded (Table 1: C=1, $n = 23$).

Table 1. Discarded data. Observing time (HJD), magnitude (V), telescope (TEL), segment (SEG) and discarding criterion (C)

HJD	V	TEL	SEG	C
2449876.7555	8.213	2	–	1
2449878.6786	8.109	2	–	1
2449882.6775	8.192	2	–	1
2449883.6783	8.158	2	–	1
2449883.7229	8.155	2	–	1
2449886.7003	8.309	2	–	1
2449886.7292	8.304	2	–	1
2449887.6784	8.180	2	–	1
2449888.6833	8.203	2	–	1
2449891.6809	8.346	2	–	1
2449893.6815	8.260	2	–	1
2449894.6718	8.250	2	–	1
2449896.6696	8.330	2	–	1
2449898.6701	8.308	2	–	1
2449900.6693	8.217	2	–	1
2449901.6691	8.289	2	–	1
2449902.6708	8.139	2	–	1
2449903.6705	8.318	2	–	1
2449904.6692	8.167	2	–	1
2449905.6591	8.210	2	–	1
2449906.6593	8.217	2	–	1
2449907.6589	8.161	2	–	1
2449908.6573	8.329	2	–	1
2450130.0134	8.094	2	1	5
2450504.8958	8.799	2	2	4
2450866.8368	8.154	1	1	3
2450934.6557	8.264	1	1	4
2450955.7222	8.144	1	1	3
2450974.6695	8.284	1	1	4
2450979.6702	8.322	1	1	4
2450986.7320	8.315	1	1	4
2451278.7070	8.104	1	2	3
2451278.7273	8.120	1	2	3
2451593.8157	8.217	2	5	5
2451706.7363	8.353	1	3	2
2451731.6859	8.195	2	5	2
2452251.0008	8.383	2	7	4
2452258.0132	8.386	2	7	4
2452348.8437	8.190	2	7	5
2452460.7124	8.324	2	7	2
2452461.6795	8.195	2	7	2
2452790.7993	8.248	1	6	5
2452807.6800	8.104	2	8	3
2452815.7371	8.288	1	6	2
2452824.7039	8.179	1	6	2
2452826.6991	8.171	1	6	2
2452828.6936	8.249	1	6	2
2453046.8944	8.013	2	9	5
2453070.8216	8.298	1	7	5
2453074.7515	7.999	2	9	3
2453139.6703	8.088	1	7	2
2453140.7700	8.379	2	9	4
2453144.6940	8.135	1	7	2
2453182.6611	8.060	1	7	2
2453184.6607	8.232	1	7	2
2453185.7171	8.155	1	7	2
2453709.0464	8.256	1	9	2
2453711.0410	8.346	1	9	2
2453711.0474	8.345	1	9	2
2453922.6616	8.243	1	9	2
2453922.6978	8.254	1	9	2
2454540.7813	8.087	1	11	3
2454807.0399	8.220	1	12	2
2454811.0305	8.260	1	12	2
2454822.0034	8.205	1	12	2
2454822.0349	8.254	1	12	2
2454999.7593	8.341	1	12	2
2455004.7444	8.298	1	12	2

Table 2. Standard Johnson V photometry of FK Com. Telescope (TEL), segments (SEG), first and last observing time (t_1 and t_n), time span and number of observations (ΔT and n)

TEL	SEG	t_1 HJD	t_n HJD	ΔT d	n
1	1	2450850.875	2450997.687	146.8	221
1	2	2451153.047	2451360.673	207.6	378
1	3	2451534.046	2451694.803	160.8	67
1	4	2451883.044	2452078.743	195.7	88
1	5	2452248.044	2452461.698	213.7	220
1	6	2452614.048	2452790.765	176.7	170
1	7	2452978.048	2453144.694	166.6	127
1	8	2453343.046	2453565.681	222.6	192
1	9	2453721.051	2453907.661	186.6	189
1	10	2454075.045	2454285.686	210.6	181
1	11	2454440.049	2454643.730	203.7	187
1	12	2454807.040	2455004.744	197.7	129
1	13	2455172.044	2455297.831	125.8	111
2	1	2450085.055	2450265.674	180.6	111
2	2	2450412.038	2450636.678	224.6	209
2	3	2450778.042	2450997.706	219.7	205
2	4	2451144.039	2451362.728	218.7	179
2	5	2451508.043	2451712.687	204.6	157
2	6	2451873.042	2452089.727	216.7	193
2	7	2452242.033	2452448.752	206.7	188
2	8	2452613.009	2452826.679	213.7	159
2	9	2452972.029	2453194.682	222.7	154

We divide the remaining data into seasonal segments (Table 2: SEG). These segment numbers are also used for the rest of the discarded data in Table 1.

Some *isolated* observations are discarded in the beginning or in the end of a few segments (Table 1: $C=2$, $n=24$). These isolated observations would mislead the second order polynomial fits which are used to eliminate the changes of the mean brightness within segments (Sect. 3: Eq. 1). The fraction of all *isolated* discarded observations, $n=47$, is 1.2% in all data.

We use a sliding window to identify the first group of *outliers*. The mean (m) and the standard deviation (s) is computed for all observations that are within $t \pm 30$ days of each individual observation $V(t)$. We discard those individual $V(t)$ observations that are below $m - 2.5s$ or above $m + 2.5s$. Some observations below the $m - 2.5s$ limit may represent photometric flares (Table 1: $C=3$, $n=7$). These events have been observed earlier in FK Com (Jetsu et al. 1993). All observations above the $m + 2.5s$ limit are very probably erroneous (Table 1: $C=4$, $n=8$).

If two observations made during the *same* night with the *same* telescope deviate more than $0.^m06$, we discard one of them as an *outlier*. This second group of outliers contains only $n=6$ observations (Table 1: $C=5$). The fraction of all *outliers*, $n=21$, is 0.5% in all data.

All the above mentioned outliers are identified *before* our analysis. This analysis will reveal that there are many other outliers (Sects. 9 and A). However, we do not reject those outliers, because they are identified only *after* the analysis.

Hackman et al. (2013) applied the Continuous Period Search method (hereafter the CPS-method) to this photometry. We refer to the model of this method as the CPS-model (Lehtinen et al. 2012, their Eq. 3). Hackman

et al. (2013) modelled 1464 subsets of photometry, but they did not publish their numerical values. Their light curve periods, amplitudes, primary minimum epochs and secondary minimum epochs are now published in electronic form (Table 3).

3. Models

Our notation for a $V(t)$ magnitude observation made at an observing time $t = t_i$ is $y_i = y(t_i)$. The time span of these n observations is $\Delta T = t_n - t_1$. We fit a second order polynomial $h(t)$ to the y_i data of each individual segment. This polynomial is used to eliminate the seasonal changes of the mean brightness of FK Com. The analysed data are $y_i = y(t_i) - h(t_i) = y_i - h_i$. (1)

We use this second order polynomial $h(t)$ in all segments, because higher orders tend to fluctuate at the ends of some segments. It would not be consistent or objective to vary the order of this polynomial in different segments. However, we will mention if this second order polynomial can, or can not, reproduce the changes of the mean brightness in individual segments (Sects. 9, and A.1-A.21).

The abbreviation $\text{DATA}_{x,y}$ is hereafter used for the $\text{TEL}=x$ observations in segment $\text{SEG}=y$. Our notations for the mean and the standard deviation of y_i are $m_{y'}$ and $\sigma_{y'}$. We model each segment of the y_i data with the two and one period models.

3.1. Two period model (2P-model)

The complex 2P-model has two parts. The first part is

$$g_1(t) = g_1(t, \bar{\beta}_1) = \sum_{k=1}^{K_1} B_k \cos(k2\pi f_1 t) + C_k \sin(k2\pi f_1 t), \quad (2)$$

where $K_1 = 2$. Higher K_1 values are unnecessary, because the detection of three minima in the photometric light curve is practically impossible (e.g. Lehtinen et al. 2011, their Sect. 3.2). The five free parameters are the amplitudes B_1, B_2, C_1 and C_2 , and the frequency f_1 . The frequency units are $[f] = \text{d}^{-1}$. The vector of free parameters is $\bar{\beta}_1 = [B_1, B_2, C_1, C_2, f_1]$. In every segment, we determine the following parameters of the $g_1(t)$ function

$$\begin{aligned} P_1 &= \text{period} = f_1^{-1} \\ A_1 &= \text{peak to peak amplitude} \\ t_{g1,\min,1} &= \text{epoch of primary (i.e. deeper) minimum} \\ t_{g1,\min,2} &= \text{epoch of secondary minimum (if present)} \end{aligned}$$

The units are $[P_1] = \text{d}$, $[A_1] = \text{mag}$ and $[t_{g1,\min,1}] = [t_{g1,\min,2}] = \text{HJD} - 2\,400\,000$. We use the epoch of the first primary and secondary minimum within each individual segment. The phases of $g_1(t)$ are computed from

$$\phi_1 = \text{FRAC}[(t - t_0)/P_1], \quad (3)$$

where $\text{FRAC}[x]$ removes the integer part of its argument x , and $t_0 = t_1$ = the first observing time of the segment data.

The second part of the 2P-model is

$$g_2(t) = g_2(t, \bar{\beta}_2) = \sum_{k=1}^{K_2} D_k \cos(k2\pi f_2 t) + E_k \sin(k2\pi f_2 t), \quad (4)$$

where $K_2 = 2$ and $\bar{\beta}_2 = [D_1, D_2, E_1, E_2, f_2]$. The following parameters

$$\begin{aligned} P_2 &= \text{period} = f_2^{-1} \\ A_2 &= \text{peak to peak amplitude} \\ t_{g2,\min,1} &= \text{epoch of primary minimum} \\ t_{g2,\min,2} &= \text{epoch of secondary minimum (if present)} \end{aligned}$$

of the $g_2(t)$ function are determined for every segment. The units are the same as those used for the $g_1(t)$ function. We compute the phases of $g_2(t)$ from

$$\phi_2 = \text{FRAC}[(t - t_0)/P_2], \quad (5)$$

where $t_0 = t_1$, as in Eq. 3.

These two parts are combined in the complex 2P-model

$$g_C(t) = g_C(t, \bar{\beta}_C) = g_1(t, \bar{\beta}_1) + g_2(t, \bar{\beta}_2). \quad (6)$$

This nonlinear model has $p_C = 10$ free parameters $\bar{\beta}_C = [\bar{\beta}_1, \bar{\beta}_2]$. Note that the functions $g_1(t)$ and $g_2(t)$ have unique phases (Eqs. 3 and 5), but no such phases exist for the $g_C(t)$ function which is constantly changing in time.

3.2. One period model (1P-model)

The simple 1P-model is

$$g_S(t) = g_S(t, \bar{\beta}_S) = \sum_{k=1}^{K_3} F_k \cos(k2\pi f_3 t) + G_k \sin(k2\pi f_3 t), \quad (7)$$

where $K_3 = 2$ and $\bar{\beta}_S = [F_1, F_2, G_1, G_2, f_3]$. There are $p_S = 5$ free parameters in this nonlinear model.

We determine the following parameters

$$\begin{aligned} P_3 &= \text{period} = f_3^{-1} \\ A_3 &= \text{peak to peak amplitude} \\ t_{S,\min,1} &= \text{epoch of primary minimum} \\ t_{S,\min,2} &= \text{epoch of secondary minimum (if present)} \end{aligned}$$

of the $g_S(t)$ function. The units are the same as those of the $g_1(t)$ and $g_2(t)$ functions. The phases of $g_S(t)$ are

$$\phi_3 = \text{FRAC}[(t - t_0)/P_3], \quad (8)$$

where $t_0 = t_1$, as in Eq. 3.

The 1P-method is a ‘‘one-dimensional’’ period finding method because it searches for only one periodicity in the data. We will consistently use the notations f_3, P_3 and A_3 also for the frequencies, the periods and the amplitudes of all other one-dimensional period finding methods that are mentioned in this study.

3.3. Nested models

The complex model of Eq. 6 and the simple model of Eq. 7 are nested. They represent the same model if

$$\begin{aligned} \text{CASE}_1: & f_1 = f_2 \text{ in Eqs. 2 and 4} \\ \text{CASE}_2: & B_1 = B_2 = C_1 = C_2 = 0 \text{ in Eq. 2} \\ \text{CASE}_3: & D_1 = D_2 = E_1 = E_2 = 0 \text{ in Eq. 4} \end{aligned}$$

We denote the cases where the complex model approaches the simple model with

$$g_C \rightarrow g_S. \quad (9)$$

The 2P-model ‘‘breaks down’’ when this happens. The alternatives when the 2P-model and the 1P-model are the same model occur in these three cases

$$f_1 - f_2 \rightarrow 0 \quad (10)$$

$$A_1/A_2 \rightarrow 0 \quad (11)$$

$$A_2/A_1 \rightarrow 0. \quad (12)$$

Table 3. CPS-method results from Hackman et al. (2013). The first column gives the telescope (TEL). The remaining columns give the same subset parameters as described in the Appendix of Lehtinen et al. (2011, their Table A.1): first observing time (t_1), last observing time (t_n), mean observing time (τ), statistically independent estimates (IND: 1=Yes, 0=No), number of observations (n), period ($P \pm \sigma_P$), peak to peak light curve amplitude ($A \pm \sigma_A$), epochs of primary and secondary minima ($t_{\min,1} \pm \sigma_{t_{\min,1}}, t_{\min,2} \pm \sigma_{t_{\min,2}}$). The dummy value “-1.000” denotes the cases where no estimate was obtained. The units of Heliocentric Julian Days are HJD-2 400 000. Note that we show only the ten first lines of this table. The full table is published only in electronic form. It contains 1464 lines (TEL=1: 760 lines) and (TEL=2: 704 lines).

TEL	t_1 HJD	t_n HJD	τ HJD	IND	n	P d	σ_P d	A mag	σ_A mag	$t_{\min,1}$ HJD	$\sigma_{t_{\min,1}}$ d	$t_{\min,2}$ HJD	$\sigma_{t_{\min,2}}$ d
1	50850.875	50874.887	50863.555	1	29	2.4129	0.0036	0.059	0.006	50851.594	0.032	-1.000	-1.000
1	50851.871	50875.883	50865.793	0	28	2.4154	0.0029	0.059	0.004	50854.043	0.034	-1.000	-1.000
1	50852.867	50876.883	50867.895	0	29	2.4141	0.0036	0.051	0.004	50853.980	0.031	-1.000	-1.000
1	50855.867	50878.809	50870.176	0	31	2.4196	0.0033	0.050	0.003	50856.395	0.027	-1.000	-1.000
1	50856.863	50880.867	50872.070	0	32	2.4155	0.0034	0.047	0.003	50858.812	0.029	-1.000	-1.000
1	50861.852	50885.855	50876.176	0	39	2.3930	0.0037	0.044	0.002	50863.754	0.029	-1.000	-1.000
1	50867.836	50891.840	50878.883	0	43	2.3923	0.0078	0.042	0.003	50868.613	0.042	50870.176	0.060
1	50868.828	50892.840	50880.621	0	43	2.3852	0.0051	0.041	0.003	50871.016	0.035	50870.215	0.057
1	50872.820	50896.828	50884.023	0	49	2.3699	0.0059	0.040	0.004	50875.008	0.041	50873.477	0.036
1	50873.820	50897.832	50885.551	0	49	2.3732	0.0061	0.039	0.004	50875.004	0.051	50875.844	0.037

The residuals of the complex model

$$\epsilon_i = y_i - g_C(t_i) \quad (13)$$

give the sum of squared residuals $R_C = \sum_{i=1}^n \epsilon_i^2$. The simple model $g_S(t)$ residuals

$$\epsilon_i = y_i - g_S(t_i) \quad (14)$$

give $R_S = \sum_{i=1}^n \epsilon_i^2$. We compute the test statistic

$$F = \left(\frac{R_S}{R_C} - 1 \right) \left(\frac{n - p_C - 1}{p_C - p_S} \right). \quad (15)$$

The null hypothesis is

H_0 : “The complex model $g_C(t)$ does not provide a significantly better fit than the simple model $g_S(t)$.”

Under H_0 , the test statistic of Eq. 15 has an F distribution with (ν_1, ν_2) degrees of freedom, where $\nu_1 = p_C - p_S$ and $\nu_2 = n - p_C$ (Draper & Smith 1998). The probability that F reaches or exceeds a fixed level F_0 is called the critical level $Q_F = P(F \geq F_0)$. We will reject H_0 , if and only if

$$Q_F < \gamma_F = 0.001, \quad (16)$$

where γ_F is a pre-assigned significance level. It represents the probability of falsely rejecting H_0 when it is in fact true.

4. Earlier 2P-model analysis

If the frequencies f_1 and f_2 in Eqs. 2 and 4 are unknown free parameters, the $g_C(t)$ model of Eq. 6 is nonlinear and there is no unique least squares fit solution. This $g_C(t)$ model becomes linear, if these f_1 and f_2 frequencies are fixed to some known numerical constant values, like $f_1 = 1/P_{\text{act}}$ and $f_2 = 1/P_{\text{orb}}$ in Jetsu et al. (2017). In this case, the solutions for the eight remaining free parameters of a least squares fit, the amplitudes $B_1, B_2, C_1, C_2, D_1, D_2, E_1$ and E_2 of the $g_1(t, \bar{\beta}_1)$ and $g_2(t, \bar{\beta}_2)$ functions, are unique.

Jetsu et al. (2017) studied the long-term photometry of 14 CABSS with the 2P-model. They showed that the long-term MLC of all these CABSS followed the orbital period

P_{orb} (Jetsu et al. 2017, Figs. 1-14: panels “b-g”). These CABSS rotate synchronously, $P_{\text{orb}} \approx P_{\text{rot}}$. This means that the starspot distribution causing the MLC of these stars is stationary in the rotating reference frame. It was also shown that the line connecting the centres of the two binary components intersects the longitudes of this stationary part.

Jetsu et al. (2017) analysed the epochs of the primary minima $t_{\min,1}$ of the seasonal light curves of CABSS with the Kuiper method. This analysis revealed the presence of long-lived active longitudes rotating with a constant period of P_{act} . Due to the inequality $P_{\text{act}} \neq P_{\text{orb}}$, the seasonal light curve minima connected to the former period migrate to the rotating reference frame, while the minima connected to the latter period do not (Jetsu et al. 2017, Figs. 15-27: tilted non-stationary and horizontal stationary lines in panels “a”).

Two segments of the photometry of RS CVn binary σ Gem were modelled by using $f_1 = 1/P_{\text{act}}$ and $f_2 = 1/P_{\text{orb}}$ in Eqs. 2 and 4 (Jetsu et al. 2017, Figs. 30 and 31). It was argued that *all* observed light curves of CABSS may be interference of two real light curves with periods of P_{act} (non-stationary in rotating reference frame) and $P_{\text{orb}} \approx P_{\text{rot}}$ (stationary in rotating reference frame).

Jetsu et al. (2017, Fig. 32) also modelled one segment of FK Com data with the 2P-model. They first fixed $f_1 = 1/P_{\text{act}}$ in Eq. 2. Their numerical value was $P_{\text{act}} = 2.^{\text{d}}401155 \pm 0.^{\text{d}}000092$ (Hackman et al. 2013). Then, they tested P_{rot} values which were $\pm 15\%$ at both sides of P_{act} . For each of these tested $f_2 = 1/P_{\text{rot}}$ in Eq. 4, they computed a test statistic $z_{\text{test}}(f_2)$ (Jetsu et al. 2017). For their chosen tested $f_1 = 1/P_{\text{act}}$ and $f_2 = 1/P_{\text{rot}}$ values, their test statistic z_{test} was equal to the test statistic that we will introduce later in Sect. 8.1 (Eq. 53).

5. Measuring surface differential rotation (SDR)

5.1. Solar SDR

Howard (1994) discussed the uncertainties in all measurements of solar SDR. He emphasized that these measure-

ments are averages of *many* features over latitude, and he then gave an example of the *real* SDR of *individual* features. His “sobering reminder” illustrated the solar SDR measurements of 36 708 sunspot groups made at Mount Wilson between the years 1917 and 1985 (Howard 1994, his Fig. 2). He emphasized that the latitude of any *individual* sunspot group did not predict its rotation period.

5.2. Stellar SDR

If the *individual* sunspot groups do not follow the law of solar SDR (see Eq. 22), then why should the *individual* starspots or starspot groups do so? More than ten *individual* SI-method surface temperature maps are available only for a few stars (see Strassmeier 2009, Table 2). The most extensive LC-method studies are typically based on about one hundred *individual* statistically independent light curve P_{phot} values (e.g. Jetsu et al. 1999; Lehtinen et al. 2016). Our intention is not to undermine the previous SI-method and LC-method studies, but it is fair to remind about the uncertainties in these stellar SDR measurements, if they truly rely on the “solar-stellar connection”.

6. SI-method

The compact answer to the *1st question* in our conclusions is based on results presented in the next Sects. 6.1-6.3.

6.1. SI-method parameters

In the SI-method, the aim is to determine the rotation periods of recognizable starspot distribution patterns at different latitudes. There are numerous different approaches (see Strassmeier 2009, 2011; Kochukhov 2016). For example, the rotation periods can be estimated directly from the surface images (e.g. Barnes et al. 2005; Balona & Abedigamba 2016), or simultaneous photometry can be used as an additional inversion constraint, or the latitudes of starspots in the surface images can be compared to the simultaneous light curves (e.g. Berdyugina et al. 1998; Korhonen et al. 2000; Hackman 2004; Korhonen et al. 2007; Cole et al. 2015).

The SI-method inversion represents an “ill posed problem”, because an infinite number of different solutions can fit the spectroscopic observations. Several stellar physical parameters are fixed *before* these inversions, e.g. inclination, rotation period and local spectral line profiles. This introduces additional uncertainty to the SI-method results (see Kochukhov 2016, his Sect 9.2.3.). One of the crucial fixed parameters in these inversions is the stellar rotation period P_{rot} value. It is fixed to some constant numerical value, like P_{phot} or P_{orb} .

The SI-method results for stellar SDR are usually measured by using the angular velocity difference

$$\Delta\Omega = \Omega_{\text{max}} - \Omega_{\text{min}} = \frac{2\pi}{P_{\text{min}}} - \frac{2\pi}{P_{\text{max}}} \quad (17)$$

(e.g. Barnes et al. 2005, their Table 1). For solar SDR, these values are $\Omega_{\text{max}} = \Omega_{\text{eq}} = 2\pi/P_{\text{eq}}$ and $\Omega_{\text{min}} = \Omega_{\text{pole}} = 2\pi/P_{\text{pole}}$, where $P_{\text{eq}} \approx 25^{\text{d}}$ and $P_{\text{pole}} \approx 35^{\text{d}}$ are the periods at the equator and the pole, i.e. the Sun has $P_{\text{eq}} < P_{\text{pole}}$.

6.2. SI-method general results

In this section, we discuss the *1st question* in the *general* context. Let us assume that the SI-method would be used to measure SDR from the observed difference between the periods of non-stationary starspots (P_{act}) and stationary starspots (P_{rot}). We compute the stellar surface differential coefficient (see Eqs. 22, 24 and 25) values from

$$|k| = \left| \frac{P_{\text{act}} - P_{\text{rot}}}{(P_{\text{act}} + P_{\text{rot}})/2} \right| \quad (18)$$

for the thirteen CABSs where the active longitude period P_{act} was detected in Jetsu et al. (2017, their Tables 1 and 3). The angular velocity range is

$$|\Delta\Omega| = \left| \frac{2\pi}{P_{\text{act}}} - \frac{2\pi}{P_{\text{rot}}} \right|. \quad (19)$$

The results are given in the order of increasing $|\Delta\Omega|$ in Table 4. The lower and upper limits are $|\Delta\Omega| = 0.0002 \text{ rad d}^{-1}$ (DM UMa) and $|\Delta\Omega| = 0.042 \text{ rad d}^{-1}$ (V711 Tau), respectively. Our lower limit, $|\Delta\Omega| \approx 0$, agrees with the results of the earlier SI-method studies because weak SDR has been observed in several stars. However, our $|\Delta\Omega|$ upper limit is about three times smaller than in Barnes et al. (2005, Table 1: 0.14 rad d^{-1}) and over ten times smaller than in Balona & Abedigamba (2016, Table 2: 0.47 rad d^{-1}).

Barnes et al. (2005) and Balona & Abedigamba (2016) give several $|\Delta\Omega|$ values for the *same* star. Even if the 2P-model were correct, the SI-methods are not so accurate that they would always give exactly the same $|\Delta\Omega|$, or equivalently the same P_{act} and P_{orb} , value for the starspots of the *same* star. This must have increased the scatter (i.e. the range) of these earlier published upper $|\Delta\Omega|$ limits. In addition to the previously mentioned inversion uncertainties, the identification of the *same* structure in temporally separated different images of the *same* star is not always unambiguous (see Sect 7.4.4: map-incompatibility). Finally, there are several additional reasons why our $|\Delta\Omega| = 0.042 \text{ rad d}^{-1}$ upper limit is certainly an underestimate, as will be explained later in Sects. 7.7. In this *general* context, the earlier published SI-method $|\Delta\Omega|$ estimates of SDR do not contradict the idea that the observed light curves of CABSs and CASSs could be interference of the two constant period (P_{act} and $P_{\text{orb}} \approx P_{\text{rot}}$) “real” light curves of the JHL-argument.

6.3. SI-method particular results

Here, we discuss the *1st question* in the *particular* context of the SI-method results presented by Berdyugina et al. (1998, II Peg) and Korhonen et al. (2000, FK Com).

Berdyugina et al. (1998) published nine surface images of II Peg between the years 1992 and 1997. Their orbital phase ephemeris was

$$\text{HJD } 2449582.9268 + 6.724333\text{E}. \quad (20)$$

Their zero epoch was equal to that given in Jetsu et al. (2017, “Ac” epoch in their Table 2). Berdyugina et al. (1998) used the P_{orb} value of Eq. 20 in the SI-method inversions. Our Fig. 1a reproduces their phase plot for the larger and smaller starspots identified with the SI-method. Berdyugina et al. (1998) concluded that this diagram shows

Table 4. Sample of thirteen CABSs in Jetsu et al. (2017). Rotation period ($P_{\text{rot}} \approx P_{\text{orb}}$), active longitude rotation period (P_{act}), difference ($|P_{\text{rot}} - P_{\text{act}}|$), differential rotation coefficient (Eq. 18: $|k|$) and angular velocity difference (Eq. 19: $|\Delta\Omega|$). Note that the parameters are given in the order of increasing $|\Delta\Omega|$.

Star	$P_{\text{rot}} \approx P_{\text{orb}}$ d	P_{act} d	$ P_{\text{rot}} - P_{\text{act}} $ d	$ k $	$ \Delta\Omega $ rad d ⁻¹
DM UMa	7.492 ± 0.009	7.4898 ± 0.0008	0.0022 ± 0.0090	0.0003 ± 0.0012	0.0002 ± 0.0010
HK Lac	24.4284 ± 0.0005	24.40 ± 0.01	0.028 ± 0.010	0.00116 ± 0.00041	0.00030 ± 0.00011
V1149 Ori	53.57465 ± 0.00072	53.14 ± 0.06	0.435 ± 0.060	0.0081 ± 0.0011	0.00096 ± 0.00013
EL Eri	48.263 ± 0.206	47.69 ± 0.02	0.57 ± 0.21	0.0119 ± 0.0043	0.00156 ± 0.00056
BM CVn	20.6252 ± 0.0018	20.513 ± 0.006	0.1122 ± 0.0063	0.00545 ± 0.00031	0.001666 ± 0.000093
II Peg	6.724333 ± 0.000010	6.7119 ± 0.0007	0.01243 ± 0.00070	0.00185 ± 0.00010	0.001731 ± 0.000098
σ Gem	19.604471 ± 0.000022	19.497 ± 0.005	0.1075 ± 0.0050	0.00550 ± 0.00026	0.001767 ± 0.000083
HU Vir	10.387522 ± 0.000031	10.419 ± 0.001	0.0315 ± 0.0010	0.003026 ± 0.000096	0.001827 ± 0.000058
XX Tri	23.96924 ± 0.00092	23.77 ± 0.01	0.199 ± 0.010	0.00835 ± 0.00042	0.00220 ± 0.00011
V1762 Cyg	28.58973 ± 0.00002	28.17 ± 0.02	0.420 ± 0.020	0.01479 ± 0.00071	0.00327 ± 0.00016
FG UMa	21.35957 ± 0.00040	21.12 ± 0.01	0.240 ± 0.010	0.01128 ± 0.00047	0.00334 ± 0.00014
EI Eri	1.947227 ± 0.000008	1.9545 ± 0.0008	0.00727 ± 0.00080	0.00373 ± 0.00041	0.0120 ± 0.0013
V711 Tau	2.83774 ± 0.00001	2.8924 ± 0.0002	0.05466 ± 0.00020	0.019078 ± 0.000069	0.04184 ± 0.00015

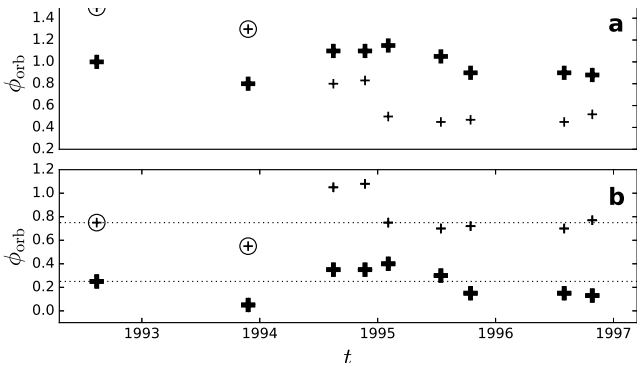


Fig. 1. Orbital phases for starspots of II Peg detected with the SI-method. (a) Larger starspots (heavier crosses) and smaller starspots (lighter crosses) with the ephemeris of Eq. 20 (Berdyugina et al. 1998, their Fig. 4). The two highlighted lighter crosses are shifted one orbital round downwards in the next panel. (b) Same data with the ephemeris of Eq. 21. The horizontal dotted lines show the orbital phases $\phi_{\text{orb}} = 0.25$ and 0.75 . Otherwise as in (a).

two active longitudes, and that a flip–flop event occurred in the year 1994.

Jetsu et al. (2017) used the orbital period ephemeris

$$\text{HJD } 2449581.246 + 6.724333E \quad (21)$$

for II Peg. Their P_{orb} was the same as in Eq. 20, but their zero epoch was $\Delta t = P_{\text{orb}}/4 \equiv \Delta\phi_{\text{orb}} = 0.25$ earlier than in Eq. 20 (Jetsu et al. 2017, “Ab” epoch in their Table 2). One of their main results was that all photometric minima of II Peg concentrated close to $\phi_{\text{orb}} = 0.25$ between the years 1988 and 1997 (Jetsu et al. 2017, their Fig. 27a). In other words, the stationary part of the light curve ($P_{\text{orb}} = P_{\text{rot}}$) dominated during this nine year time interval which overlaps the four year time interval of the SI-method images in Berdyugina et al. (1998).

Our Fig. 1b shows the phases of the same starspots as in Fig. 1a, except that we use the ephemeris of Eq. 21. Unlike Berdyugina et al. (1998), we do not deliver evidence for a flip–flop event by adding one extra orbital round to the two first ϕ_{orb} values of smaller starspots (Figs. 1ab: two highlighted lighter crosses). The starspots of the first

image in the year 1992 are exactly at $\phi_{\text{orb}} = 0.25$ and $\phi_{\text{orb}} = 0.75$, respectively. All larger starspots are at both sides of phase $\phi_{\text{orb}} = 0.25$. Most of the smaller starspots concentrate close to $\phi_{\text{orb}} = 0.75$. The simultaneous MLC of II Peg also confirms that the main activity concentrated on the longitude coinciding with the line connecting the centres of the two binary components (Jetsu et al. 2017, Fig. 14d–e: $\phi_{\text{orb}} = 0.25$). Berdyugina et al. (1998) noted that the mean latitudes of these starspots discovered with the SI-method remained approximately the same in all images. This is a convincing *particular* case, where the SI-method detects a stationary starspot of II Peg rotating with a constant period $P_{\text{orb}} = P_{\text{rot}}$ during a time interval of over four years.

Korhonen et al. (2000) published six surface images of FK Com between the years 1994 and 1997. They used the period $P_{\text{phot}} = 2.^{\text{d}}4002466 \pm 0.^{\text{d}}0000056$ in the SI-method image inversions. Comparison of their six images revealed the presence of long-lived starspots rotating with a constant period $P_{\text{SI}} = 2.^{\text{d}}4037 \pm 0.^{\text{d}}0005$. The dates of these images overlap the time interval of our photometry between the years 1995 and 1997, except for the year 1994. The thirteen first statistically independent $t_{\text{min},1}$ epochs in our Table 3 (IND=1) are between the years 1995.43 and 1997.41. The K-method analysis of these thirteen epochs gives $P_{\text{act}} = 2.^{\text{d}}4035 \pm 0.^{\text{d}}0005$. The $P_{\text{SI}} - P_{\text{act}}$ difference is only $0.^{\text{d}}0002 \pm 0.^{\text{d}}0007$. The latitude range of the starspots detected with the SI-method was between 45° and 70° , and the migration of these starspots followed “solid body rotation” (Korhonen et al. 2000). In this *particular* case, the SI-method undoubtedly detects a long-lived non-stationary starspot of FK Com rotating with a constant period P_{act} .

The starspots detected in the above two *particular* SI-method studies by Berdyugina et al. (1998) and Korhonen et al. (2000) were long-lived and rotated with a constant angular velocity, as predicted by the JHL-argument. This type of stability quite common in surface images. For example, the sequence 37 consecutive surface images during 57 nights show that the strongest starspot in HR1009 appears to be nearly stationary in the rotating reference frame (Strassmeier & Bartus 2000, their Fig. 8: starspot “A”). Our answer to the *1st question* is that the *general* and the *particular* evidence strongly indicates that the P_{act} and

$P_{\text{rot}} \approx P_{\text{orb}}$ periods of the JHL-argument have already been detected with the SI-method.

7. LC-method

We give compact answers to the *2nd question* and the *3rd question* in the conclusions (Sect. 17). These answers are based on the results presented in Sects. 7.3-7.4.1.

7.1. LC-method parameters

In the LC-method approach, the most widely used period finding method is the Lomb-Scargle periodogram (hereafter the LS-method, Lomb 1976; Scargle 1982). It is equivalent to finding the best least squares sinusoidal model for the data (hereafter LS-model). The LS-method is a one-dimensional period finding method because it determines only one period value for the data. There are numerous other one-dimensional period finding methods that can search for more complex models in the data (e.g. Lehtinen et al. 2011, the CPS-method).

The LC-methods usually use the following approximation for the law of solar SDR

$$P(b) = \frac{P_{\text{eq}}}{1 - k \sin^2 b}, \quad (22)$$

where b is the latitude, P_{eq} is the rotation period at the equator and k is the SDR coefficient (e.g. Hall & Busby 1990; Hall 1991, solar $k = k_{\odot} = 0.186$). A useful parameter is

$$h = \sin^2(b_{\text{max}}) - \sin^2(b_{\text{min}}), \quad (23)$$

where b_{min} and b_{max} are the minimum and maximum latitudes of starspot formation. The largest possible latitude range, $b_{\text{min}} = 0^\circ$ and $b_{\text{max}} = \pm 90^\circ$, gives $h = 1$. All other latitude ranges give $h < 1$. This leads to the relation

$$k = \frac{\Delta P}{h P_{\text{eq}}}, \quad (24)$$

where $\Delta P = |P(b_{\text{max}}) - P(b_{\text{min}})| = P_{\text{phot,max}} - P_{\text{phot,min}}$ is the difference between the largest and smallest observed photometric rotation period P_{phot} in any particular star. Since $h \leq 1$, the LC-methods use the lower limit

$$|k| \geq \frac{P_{\text{phot,max}} - P_{\text{phot,min}}}{P_{\text{phot,mean}}} \quad (25)$$

for the absolute value of stellar SDR coefficient, where $P_{\text{phot,mean}}$ is the mean of all observed values of P_{phot} . There are four uncertainties in this relation. Firstly, $P_{\text{phot,mean}} \approx (P_{\text{phot,max}} + P_{\text{phot,min}})/2$ must to be used as an approximate estimate for P_{eq} of Eq. 24, because it is not known whether $P_{\text{phot,min}}$ or $P_{\text{phot,max}}$ represents P_{eq} . Some LC-methods use $P_{\text{eq}} = P_{\text{phot,max}}$ (e.g. Reinhold et al. 2013). Secondly, the sign of k is unknown, where $k > 0$ represents solar and $k < 0$ represents anti-solar SDR. Thirdly, the latitude range of starspot formation, the value of h in Eqs. 23 and 24, is unknown. Fourthly, it is not known if the full range of period changes has already been observed, or does the observed $P_{\text{phot,max}} - P_{\text{phot,min}}$ difference represent an underestimate of the real range.

Another approach for measuring the range of changes for n photometric rotation periods $P_{\text{phot},i}$ (e.g. Lehtinen et al. 2016) is to use the weighted mean

$$P_w = \frac{\sum_{i=1}^n w_i P_{\text{phot},i}}{\sum_{i=1}^n w_i} \quad (26)$$

and the weighted standard deviation

$$\Delta P_w = \sqrt{\frac{\sum_{i=1}^n w_i (P_{\text{phot},i} - P_w)^2}{\sum_{i=1}^n w_i}}, \quad (27)$$

where $\sigma_{P_{\text{phot},i}}$ is the error of $P_{\text{phot},i}$ and the weights are $w_i = \sigma_{P_{\text{phot},i}}^{-2}$. Equal weights $w_i = 1$ give $P_w = m_P$ and $\Delta P_w = \sigma_P$, where m_P and σ_P are the mean and standard deviation of all observed $P_{\text{phot},i}$ values. In this case, the ‘‘three sigma’’ upper limit for the $P_{\text{phot},i}$ changes is

$$Z = \frac{6\Delta P_w}{P_w} = \frac{6\sigma_P}{m_P}. \quad (28)$$

The relation

$$|k| \approx Z/h \quad (29)$$

is valid, if $P_{\text{phot,max}} - P_{\text{phot,min}} \approx 6\Delta P_w$ (Jetsu et al. 2000).

7.2. LC-method results

The idea that the value of P_{phot} is connected to the stellar rotation period P_{rot} is logical. In the SDR context, the observed value of P_{phot} could tell something about the latitude of the spot. If the *observed* P_{phot} has changed, it is logical to assume that the latitude of the spot has changed. Thus, the range of P_{phot} changes could measure SDR.

Hall (1991) applied the LC-method to the photometry of 277 late-type stars. He concluded that the stellar SDR correlates strongly with $P_{\text{phot}} \approx P_{\text{rot}}$. It decreases when P_{phot} decreases. He showed that SDR was so weak in some rapidly rotating stars that it approached solid-body rotation. This general relation between P_{phot} and SDR has been amply confirmed by subsequent LC-method studies of much larger samples (e.g. Reinhold et al. 2013, 24 124 stars). We have also formulated our own LC-methods, and used them to measure stellar SDR (e.g. Jetsu & Pelt 1999; Jetsu et al. 1999; Lehtinen et al. 2011, 2016, the TSPA-method and the CPS-method). Considering all these findings, our JHL-argument runs into its next problem: what is the answer to the *2nd question*. Note that we have very good reasons for emphasizing the words *many*, *different*, *observed* and *same* in this particular question, as will become evident in the next Sects. 7.3-7.4.1.

7.3. Simulated 2P-model data

Here, we assume that the 2P-model is correct and we simulate artificial photometric data of two different cases. The model used in creating the simulated data is the sum of two sinusoidal light curves

$$s_1(t) = a_1 \sin(2\pi f_1 t) \quad (30)$$

$$s_2(t) = a_2 \sin(2\pi f_2 t). \quad (31)$$

This model has $s_1(t) = g_1(t)$ in Eq. 2, $s_2(t) = g_2(t)$ in Eq. 4 and $s(t) = s_1(t) + s_2(t) = g_C(t)$ in Eq. 6. The peak to peak

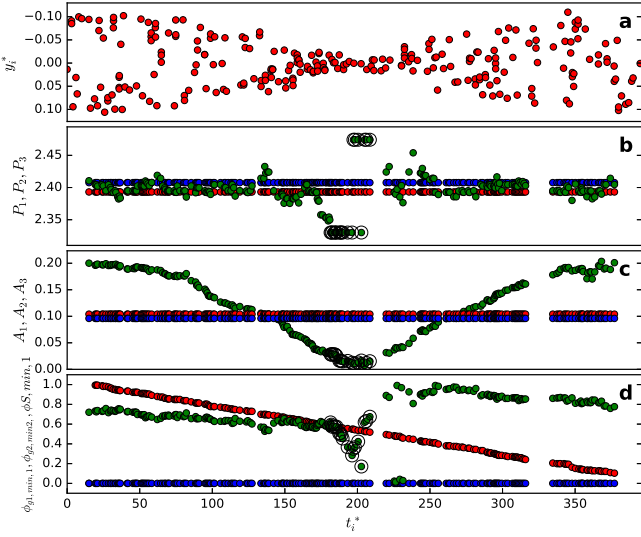


Fig. 2. (a) Simulated y_i^* data of Eq. 33 for equal amplitudes $a_1 = a_2 = 0.^m05$ in Eqs. 30 and 31. (b) Periods $P_1 = 2.^d39313$ and $P_2 = 2.^d40762$ of the 2P-model are denoted with red and blue circles. The green circles show the periods P_3 detected with the LS-method. The large black circles around some green circles highlight the cases, where the highest z_{LS} periodogram value is in the beginning or in the end of the tested period interval. (c) Amplitudes $A_1 = 2a_1$ and $A_2 = 2a_2$ of the 2P-model are denoted with red and blue circles. Note that these red and blue symbols are slightly shifted apart, because they would otherwise overlap. The green circles show the peak to peak amplitudes A_3 of the LS-model sinusoids. The same models as in "b" are highlighted again. (d) The red and blue circles show the light curve minimum phases of $g_1(t) = s_1(t)$ and $g_2(t) = s_2(t)$ with P_2 in Eq. 3. The green circles show the light curve minima of the LS-method sinusoids. The highlighted models are the same as in "bc".

amplitudes are $A_1 = 2a_1$ and $A_2 = 2a_2$. The frequencies are fixed to $f_1 = P_1^{-1}$ and $f_2 = P_2^{-1}$, where the periods are $P_1 = 2.^d39313$ and $P_2 = 2.^d40762$ (see Eqs 69 and 70). We compute the lap cycle period

$$P_{\text{lap}} = |P_1^{-1} - P_2^{-1}|^{-1} = |f_1 - f_2|^{-1} \approx 398^d \quad (32)$$

of these periodicities (Jetsu et al. 2017, their Eq. 4). The interference pattern of $s(t) = s_1(t) + s_2(t)$ is repeated regularly after every $\Delta T = P_{\text{lap}}$. Hence, the time span of the simulated data segment is fixed to $\Delta T = P_{\text{lap}}$. We use multiples of sidereal day $P_{\text{sid}} = 0.^d99726958$ to create $n^* = 250$ time points

$$t_i^* = i^* P_{\text{sid}} + \delta t_i^*,$$

where i^* are a random sample of integers $1 \leq i^* \leq 398$. Any particular integer i^* value is used as many times as the random selection favours it. The simulated random shifts δt_i^* at both sides of the mid-nights $i^* P_{\text{sid}}$ are evenly distributed between $-0.^d2$ and $0.^d2$. The simulated data are

$$y_i^* = s(t_i^*) + \epsilon_i^*, \quad (33)$$

where ϵ_i^* are a random sample of $n^* = 250$ residuals drawn from a Gaussian distribution with a zero mean and a standard deviation of $0.^m008$.

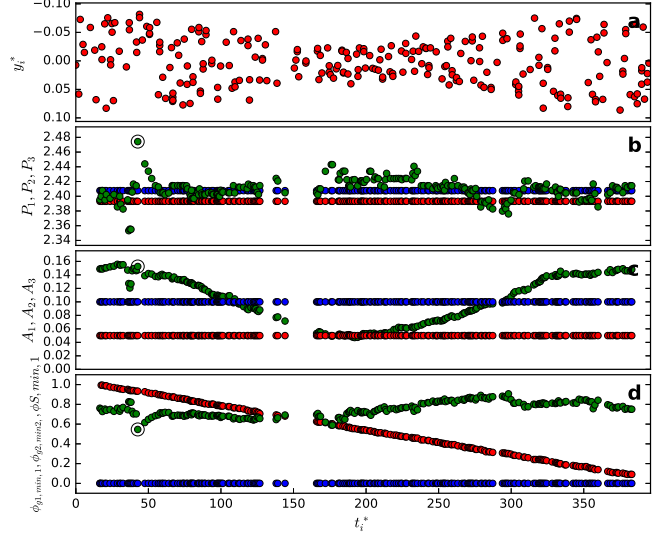


Fig. 3. Simulated y_i^* data of Eq. 33 for unequal amplitudes $a_1 = 0.^m025$ in Eq. 30 and $a_2 = 0.^m050$ in 31, otherwise as in Fig. 2.

Inside the simulated segment, we select datasets containing all y_i^* that are within a sliding window of $\Delta T = 30^d$. We apply the LS-method to all those datasets that contain at least $n = 12$ values of y_i^* . Similar sliding window one-dimensional period analysis has been applied to real photometry, e.g. by Distefano et al. (2016, the LS-method) or Lehtinen et al. (2016, the CPS-method). The maximum and minimum values of tested $f_3 = P_3^{-1}$ frequencies of the LS-model are

$$f_{\text{min}} = (1 - a)f_{\text{mid}}, \quad f_{\text{max}} = (1 + a)f_{\text{mid}}, \quad (34)$$

where $P_{\text{mid}} = (P_1 + P_2)/2$, $f_{\text{mid}} = P_{\text{mid}}^{-1}$, and $a = 0.03$. This is the $\pm 3\%$ range at both sides of f_{mid} .

The same interference pattern of $s(t) = s_1(t) + s_2(t)$ is repeated regularly after every P_{lap} of Eq. 32. Thus, any constant zero epoch shift in Eqs. 30 and 31 will only shift the sum $s(t)$ curve within the time interval $\Delta T = P_{\text{lap}}$ of simulated data. We therefore use the time values $t - P_1/2$ in Eq. 30 and $t - P_2/2$ in Eq. 31 in the simulations shown in our Figs. 2 and 3. These zero epoch shifts do not alter the simulation results. With these shifts, however, the amplitude of the sum $s(t)$ is lowest in the middle of the simulated segment where the most interesting phenomena occur. We do not use these zero epoch shifts in the time values t of Eqs. 30 and 31, because this provides an easy connection to the results presented later in Sect. 7.6.

7.3.1. $a_1 = a_2$ simulation (TEST $_{a_1=a_2}$)

In the first case, we use equal amplitudes $a_1 = a_2 = 0.^m05$ in Eqs. 30 and 31. We will hereafter refer to these simulations as TEST $_{a_1=a_2}$. The results are shown in Fig. 2.

The amplitude of the simulated data decreases to zero during the first half of the segment and then increases back to its original level during the last half (Fig. 2a). This pattern is repeated during every lap cycle $\Delta T = P_{\text{lap}}$ (Eq. 32), because the interference of these two sinusoids is regular. The periods P_1 and P_2 of the simulated model do not change (Fig. 2b: red and blue circles). However, the periods detected with the LS-method show large variation (Fig. 2b:

green circles), especially when the amplitude of the simulated data approaches zero in the middle of the segment. There are cases where the highest LS-method periodogram z_{LS} value is at the end of the tested period interval (Fig. 2b: highlighted green circles). This is a clear sign of that the tested period interval is too narrow for this particular period finding method. The amplitudes A_1 and A_2 of the 2P-model remain unchanged (Fig. 2c: red and blue circles). The peak to peak amplitudes A_3 of the sinusoidal LS-models vary between $0.^m0$ and $0.^m2$ (Fig. 2c: green circles). The phases of the light curve minima of $s_2(t)$ are stable with P_2 in Eq. 3 (Fig. 2d: blue circles), while those of $s_1(t)$ show regular linear migration (Fig. 2d: red circles). Finally, the minima of the sinusoidal models detected with the LS-method show minor linear changes and an abrupt 0.5 phase shift in the middle of the segment (Fig. 2d: green circles). This phase shift occurs when the amplitude A_3 approaches zero, and this event coincides with the cases when no periodicity is detected with the LS-method (Figs. 2bcd: highlighted green circles). We emphasize that this half a rotation phase shift occurs in *every* simulated artificial data sample of Eq. 33 when $a_1 = a_2$.

7.3.2. $a_1 < a_2$ simulation (TEST $_{a_1 < a_2}$)

In the second case, the amplitudes are unequal: $a_1 = 0.^m025$ in Eq. 30 and $a_2 = 0.^m05$ in Eq. 31. These simulations are hereafter referred to as TEST $_{a_1 < a_2}$.

The amplitude of the simulated data first decreases from $0.^m15$ to $0.^m05$, and then increases back to $0.^m15$ (Fig. 3a). The periods P_1 and P_2 do not, of course, change (Fig. 3b: red and blue circles). There is large variation in the P_3 periods detected with the LS-method (Fig. 3b: green circles). This variation is largest in the middle of the segment when the amplitude is lowest. The amplitudes A_1 and A_2 of the 2P-model do not change (Fig. 3c: red and blue circles). The peak to peak amplitudes A_3 of the LS-models vary regularly between $0.^m05$ and $0.^m15$ (Fig. 3c: green circles). The same phases of the light curve minima of $s_1(t)$ and $s_2(t)$ as in the previous Fig. 2d are shown again in Fig. 3d (red and blue circles). The phases of the minima of the sinusoidal LS-models fluctuate (Fig. 3d: green circles). The cases when the LS-method detects no periodicity do not occur as often as in TEST $_{a_1 = a_2}$, because the amplitude does not decrease to zero in the middle of the segment (Figs. 3bcd: one highlighted circle).

7.4. Incompatibility

The TEST $_{a_1 = a_2}$ and TEST $_{a_1 < a_2}$ simulations reveal something that we will hereafter refer to as “incompatibility”. If the JHL-argument is true, this incompatibility manifests itself in the *observed* light curve periods, amplitudes and minima determined with any one-dimensional period finding method, like e.g. the LS-method or the CPS-method.

The amplitudes A_1 and A_2 of the simulated light curves are constant in the above mentioned TEST $_{a_1 = a_2}$ and the TEST $_{a_1 < a_2}$ simulations. All incompatibility effects described in the next Sects. 7.4.1-7.4.4 are even stronger in the real data, because these A_1 and A_2 amplitudes are changing. These effects are nicely illustrated in the periodogram of all data which resembles a patchwork quilt (see Sect. 13: Fig. 14).

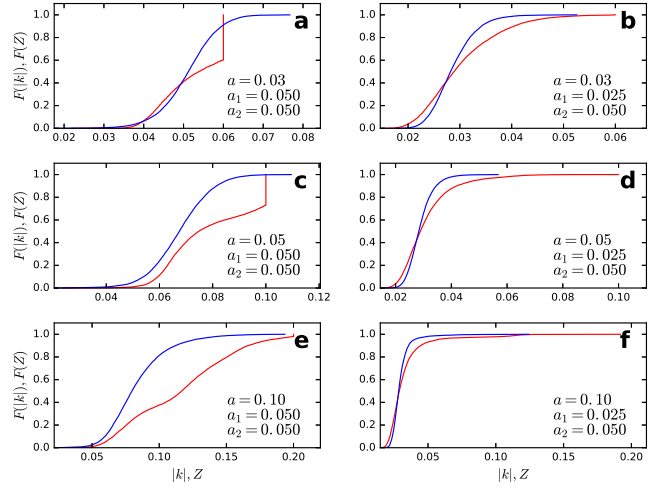


Fig. 4. (a) Cumulative distribution functions $F(|k|)$ (red) and $F(Z)$ (blue) in 10 000 simulations of TEST $_{a_1 = a_2}$ with $a = 0.03$ in Eq. 34 (b) same as in “a” for TEST $_{a_1 < a_2}$. (c) $a = 0.05$ in Eq. 34, otherwise as in “a”. (d) $a = 0.05$ in Eq. 34, otherwise as in “b”. (e) $a = 0.10$ in Eq. 34, otherwise as in “a”. (f) $a = 0.10$ in Eq. 34, otherwise as in “b”.

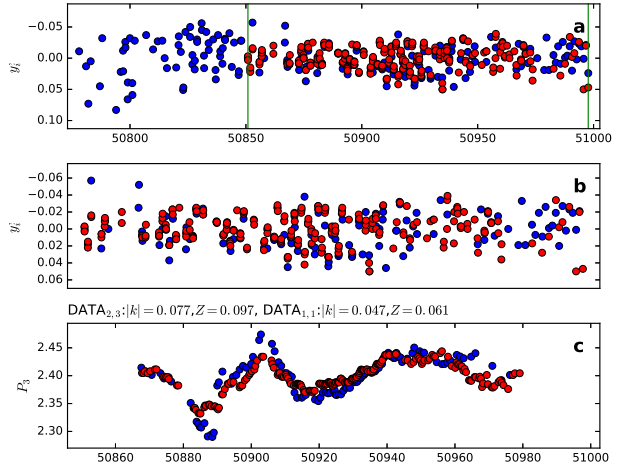


Fig. 5. (a) Overlapping DATA $_{2,3}$ and DATA $_{1,1}$ photometry (red and blue filled circles). Vertical green lines show the beginning and the end of fully overlapping observations. (b) Fully overlapping photometry. (c) Red and blue filled circles denote P_3 periods detected from the fully overlapping photometry with the LS-method. The $|k|$ and Z results are given above this panel.

7.4.1. Period-incompatibility

The TEST $_{a_1 = a_2}$ and TEST $_{a_1 < a_2}$ simulations both show that the LS-method detects spurious P_3 periods and spurious P_3 changes although the 2P-model periods P_1 and P_2 do not change.

The P_3 period results in Fig. 2b represent only one particular simulated TEST $_{a_1 = a_2}$ case where $a = 0.03$ in Eq. 34, and $a_1 = a_2 = 0.050$ in Eqs. 30 and 31. We simulated 10 000 such cases having this same a , a_1 and a_2 combination. Each case gave us one estimate of $|k|$ (Eq. 25) and Z (Eq. 28). The cumulative distribution functions $F(|k|)$ and $F(Z)$ of these parameters are shown in Fig. 4a (red and blue

continuous lines). The parameter ranges are approximately $0.035 \leq |k| \leq 0.06$ and $0.03 \leq Z \leq 0.07$. A steep rise of $F(|k|)$ occurs at $2a = 0.06$. The probability for $F(|k| \geq 2a)$ is nearly 0.5. The $|k|$ values can not exceed this $2a$ limit, because the maxima and the minima of detected P_3 values have to be within the tested period interval (Eq. 34). In nearly half of the 10 000 cases, the LS-method detects P_3 periods over the whole tested period interval $(1 \pm a)P_{\text{mid}}$. The shape of $F(Z)$ resembles that of a Gaussian cumulative distribution function.

The results for 10 000 simulated $\text{TEST}_{a_1 < a_2}$ cases with $a = 0.03$, $a_1 = 0.025$ and $a_2 = 0.050$ are shown in Fig. 4b. The approximate ranges are $0.02 \leq |k| \leq 0.06$ and $0.02 \leq Z \leq 0.05$. The minimum peak to peak amplitude of the simulated $s(t)$ light curve is $A_3 = 2a_1 = 0.050$ in these $\text{TEST}_{a_1 < a_2}$ simulations. Since A_3 does not decrease to zero, as in $\text{TEST}_{a_1 = a_2}$, the LS-method succeeds in detecting periodicities that are within the tested period interval.

The combination $a = 0.05$, $a_1 = 0.050$ and $a_2 = 0.050$ (Fig. 4c) shows what happens in $\text{TEST}_{a_1 = a_2}$ with a longer tested $\pm 5\%$ period interval. The $|k|$ and Z ranges increase, and the “expected” steep $F(|k|)$ rise occurs at $2a = 0.10$. The $\text{TEST}_{a_1 < a_2}$ combination $a = 0.05$, $a_1 = 0.025$ and $a_2 = 0.050$ shows no steep $F(|k|)$ rise at $|k| = 2a$ (Fig. 4d). The results for $a = 0.10 \equiv \pm 10\%$ are shown in Figs. 4e,f. The LS-method keeps on finding P_3 periods over the whole period interval in $\text{TEST}_{a_1 = a_2}$ simulations, because the $|k|$ maximum is at $2a = 0.20$. The general result is that the $|k|$ and Z ranges increase when the tested range, a in Eq. 34, increases.

The simulations shown in Figs. 4a–f also reveal that the relation $|k| \approx Z/h$ of Eq. 29 is a poor approximation. This is no surprise, because $|k|$ is computed from *two* individual P_3 values, while Z is computed from *all* P_3 values.

If the JHL-argument is correct, our simulations also predict that two observers *observing* the light curve of *same* star during the *same* time interval will get *different* P_3 , $|k|$ and Z values with the LS-method. We show the temporally overlapping $\text{DATA}_{2,3}$ and $\text{DATA}_{1,1}$ photometry in Fig. 5a. The fully overlapping data are shown in Fig. 5b. We divide these fully overlapping data into subsets using a sliding window of 30 days, and analyse all subsets having at least 12 observations with the LS-method (Eq. 34: $a = 0.05$). In Fig. 5c, we show the P_3 , $|k|$ and Z results for the fully overlapping data of segments $\text{DATA}_{2,3}$ and $\text{DATA}_{1,1}$. The respective results for all temporally overlapping pairs of segments are given in Table 5. These results confirm the above prediction.

If the JHL-argument is true, no-one ever gets the same LS-method analysis results from the simultaneous photometry of the same star. This general result applies to all one-dimensional period finding methods. All the above findings are amazing considering that the underlying 2P-model, $g_C(t) = s(t) = s_1(t) + s_2(t)$, does not change at all. Since this period incompatibility solves the *2nd question*, it is easy to the answer the *3rd question* (see Sect. 17).

7.4.2. Amplitude-incompatibility

The *observed* light curve amplitudes A_3 in Figs. 2c and 3c do not certainly tell anything about the *real* light curve amplitudes A_1 and A_2 of the 2P-model. We will hereafter refer to this problem as “amplitude-incompatibility”. It is common for all one-dimensional period finding methods.

Table 5. $|k|$ and Z for fully overlapping real observations. Columns 1 and 4 give the temporally overlapping segments. The other columns give the $|k|$ and Z values for fully overlapping data.

	$ k $	Z		$ k $	Z
$\text{DATA}_{2,3}$:	0.077	0.097	$\text{DATA}_{1,1}$:	0.047	0.061
$\text{DATA}_{2,4}$:	0.100	0.141	$\text{DATA}_{1,2}$:	0.063	0.085
$\text{DATA}_{2,5}$:	0.022	0.032	$\text{DATA}_{1,3}$:	0.012	0.016
$\text{DATA}_{2,6}$:	0.014	0.018	$\text{DATA}_{1,4}$:	0.010	0.012
$\text{DATA}_{2,7}$:	0.079	0.068	$\text{DATA}_{1,5}$:	0.070	0.096
$\text{DATA}_{2,8}$:	0.051	0.062	$\text{DATA}_{1,6}$:	0.025	0.032
$\text{DATA}_{2,9}$:	0.088	0.091	$\text{DATA}_{1,7}$:	0.048	0.038

The period analysis of the observed amplitudes A_3 can sometimes be used to determine the numerical value for the lap cycle period P_{lap} of Eq. 32. These P_{lap} cycles were clearly present in the observed A_3 amplitudes of thirteen CABSs (Jetsu et al. 2017, their Figs. 15–27). The numerical P_{lap} value can also be used to indirectly estimate other 2P-model parameters (see Sect. 7.7).

7.4.3. Minima-incompatibility

The one-dimensional period finding methods also suffer from something that we will hereafter refer to as “minima-incompatibility”. If we would analyse the light curve minima epochs of Figs. 2d and 3d with the K-method, we would not detect the P_1 period or the P_2 period. We could detect P_2 when $A_1 = 0$ (CASE₂) or P_1 when $A_2 = 0$ (CASE₃). Unfortunately, the observed light curve does not give us any unambiguous information of when $A_1 = 0$ or when $A_2 = 0$. Thus, the next logical step is to begin to search for the answers to the *4th question*, the *5th question* and the *6th question*.

7.4.4. Map-incompatibility

If the JHL-argument is true, the non-stationary and stationary starspots migrate with different Ω angular velocities. In this case, the comparison of surface images from different years can lead to false identifications of the non-stationary (P_{act}) and the stationary (P_{orb} or P_{rot}) starspots. In general, there is no unique period in the $g_C(t)$ model for comparing the longitudinal difference between two starspots, say A and B, over a longer period of time. It is also uncertain, if A moves forwards or backwards with respect to B. The 2P-model predicts that one can reliably compare two surface images of the *same* star with the *same* constant period only if the time difference of these surface images is much shorter than $P_{\text{lap}}/2$. For example, the lap cycle period of FK Com is only $P_{\text{lap}} = 398^{\text{d}}$. This is comparable to the typical one year gap between observing seasons. We will hereafter refer to this problem as “map-incompatibility”. This effect resembles the shuffling of cards. The current order of cards (i.e. longitudes of starspots A and B) does not give any information about the order before the shuffling. This effect has certainly been overlooked or underestimated in earlier SI-method studies, like Washuettl et al. (2009, EI Eri: eleven years), Lindborg et al. (2011, II Peg: six years) or Hackman et al. (2013, FK Com: 13 years). This map incompatibility must have

caused numerous misidentifications of the rotating structures, because there are no unique phases or longitudes in the constantly changing 2P-model. Such misidentifications have increased the range of $|\Delta\Omega|$ estimates, e.g. in Barnes et al. (2005) or Balona & Abedigamba (2016), which were discussed earlier in Sect 6.

7.5. Dead end

Jetsu et al. (2017) assumed that the K-method analysis of the $t_{\min,1}$ minima epochs of Table 3 would give an unambiguous P_{act} value for FK Com (the 4th question). The next step in their reasoning was to use this P_{act} value in solving an unambiguous P_{rot} value for FK Com. However, we have just shown that *if* the $t_{\min,1}$ minima epochs are determined with any one-dimensional period analysis method, *then* the minima-incompatibility prevents a unique P_{act} solution. Any particular $t_{\min,1}$ value in our Table 3 may, or may not, be connected to P_{act} and/or P_{rot} (see Sect. 7.7: MIGRATION₁, MIGRATION₂ and MIGRATION₃ alternatives). This problem could be at least partly solved, if we knew the time intervals *when* the interference caused by the other periodicity is absent, and *only* the P_{act} or P_{rot} period totally dominates the light curves of FK Com (CASE₂ or CASE₃). However, we have no way of knowing when takes place.

We could try to use the known orbital period $P_{\text{orb}} \approx P_{\text{rot}}$ to solve P_{act} , if FK Com were a binary, like the 14 CABSs studied in Jetsu et al. (2017). This *certainly known* P_{rot} could then be used to solve P_{act} in a similar way, as P_{rot} was solved by using the *presumably known* P_{act} (Jetsu et al. 2017, their Fig. 32). Unfortunately, we do not have the “luxury” of knowing the P_{rot} period of FK Com *before* the analysis.

If the JHL-argument is true, we must conclude that all our earlier one-dimensional period analyses have given spurious results, because these results suffer from incompatibility. The same applies to all one-dimensional period finding analyses of starspots done by others during the past 70 years since Kron (1947) published his first observations of starspots. Due to this incompatibility, neither one of the two P_{act} and P_{rot} periods of FK Com can be fixed before the analysis. These two periods must be solved simultaneously. At this point, we have a serious problem, because our current study of FK Com photometry has arrived at a dead end: we can not use the $t_{\min,1}$ minima epochs of Table 3 to get an unambiguous solution for the numerical P_{rot} or P_{act} period values of FK Com (the 4th question and the 5th question).

7.6. Sum of two different frequency sinusoids

In Sect. 7.3, we assumed that the 2P-model is correct and simulated artificial data with this model. Here, we show *how* these results could have been anticipated mathematically, and especially the incompatibility. The mathematical relations presented in this section explain all graphical results presented earlier in Figs. 2 and 3.

If $f_1 \approx f_2$, the solution for the sum $s(t)$ of sinusoidal light curves $s_1(t)$ and $s_2(t)$ of Eqs. 30 and 31 depends *only* on the amplitudes a_1 and a_2 . The solutions are different for

$$a_1 = a_2 \quad (35)$$

$$a_1 \neq a_2. \quad (36)$$

If Eq. 35 is true, then

$$s(t) = s_1(t) + s_2(t) = a_a(t) \sin(2\pi f_a t), \quad (37)$$

where the amplitude is

$$a_a(t) = a_1 \sqrt{2 + 2 \cos[2\pi(f_1 - f_2)t]} \quad (38)$$

and the frequency is

$$f_a = (f_1 + f_2)/2. \quad (39)$$

This frequency of the sum $s(t)$ remains constant $f = f_a$. Hence, the P_3 periods detected with the LS-method concentrate between P_1 and P_2 in Fig. 2b. The amplitude $a_a(t)$ of Eq. 38 varies between $a_{a,\min} = 0$ and $a_{a,\max} = 2a_1$ with the lap cycle period P_{lap} . This regularity is seen in Fig. 2c. Finally, an abrupt $f_a/2$ phase shift of $s(t)$ occurs when $a_a(t)$ goes to zero, as seen in Fig. 2d.

If Eq. 36 is true, we assume that $a_1 < a_2$. In this case, the sum is

$$s(t) = s_1(t) + s_2(t) = a_b(t) \sin[2\pi f_2 t + \phi_b(t)], \quad (40)$$

where the amplitude is

$$a_b(t) = \sqrt{a_1^2 + a_2^2 + 2a_1 a_2 \cos[2\pi(f_1 - f_2)t]} \quad (41)$$

and the phase shift is

$$\phi_b(t) = \arctan \left[\frac{a_1 \sin[2\pi(f_1 - f_2)t]}{a_1 \cos[2\pi(f_1 - f_2)t] + a_2} \right]. \quad (42)$$

The $[\phi_b(t)]$ units are radians.

The amplitude $a_b(t)$ of Eq. 41 varies regularly between

$$a_{b,\min} = a_2 - a_1 \quad (43)$$

and

$$a_{b,\max} = a_1 + a_2 \quad (44)$$

during the lap cycle period P_{lap} , as seen in Fig. 3c.

The phase modulation $\phi_b(t)$ induces frequency changes of $s(t)$ between

$$f_{b,\max} = f_2 + \frac{a_1(f_1 - f_2)}{a_2 + a_1} \quad (45)$$

at the $a_{b,\max}$ epochs, and

$$f_{b,\min} = f_2 - \frac{a_1(f_1 - f_2)}{a_2 + a_1} \quad (46)$$

at the $a_{b,\min}$ epochs. These frequency changes of $s(t)$ at both sides of f_2 are repeated regularly during P_{lap} . The frequency f_2 of the stronger $s_2(t)$ sinusoid ($a_1 < a_2$) dominates these frequency changes of $s(t)$. The P_3 changes in Fig. 3b concentrate on the level of the stronger P_2 periodicity.

The maximum $\phi_b(t)$ phase shift is

$$\phi_{b,\max} = \arcsin(a_1/a_2) \quad (47)$$

to both directions. The $[\phi_{b,\max}]$ units are radians. For $a_1 = a_2$, the maximum phase shift $\phi_{b,\max}$ is $\pi/2$ radians, or equivalently $(\pi/2)/(2\pi) = 1/4$ in dimensionless phase units with f_2 . Since this shift at $a_{b,\min}$ occurs to both directions, its full range is

$$\Delta\phi_b = [\arcsin(a_1/a_2)]/\pi \quad (48)$$

in dimensionless phase units. This gives $\Delta\phi_b = 0.5$ when $a_1 = a_2$. No phase shift can exceed this limit. This abrupt phase shift occurs also when $a_1 \neq a_2$, but it is smaller. For example, the $a_1 = 0.^m048$ and $a_2 = 0.^m050$ combination causes an abrupt $\Delta\phi_b = 0.41$ phase shift at $a_{b,\min}$. The predicted phase shift in Fig. 3d is only $\Delta\phi_b = 0.17$.

In conclusion, the *observed* amplitude, period and minimum of the sum $s(t)$ fluctuate regularly with the lap period cycle P_{lap} when the condition of Eq. 36 is true.

7.7. Indirect approach

Now that we know all these different mathematical relations for the sum $s(t) = s_1(t) + s_2(t)$ presented in the previous Sect. 7.6, it is still next to impossible to figure out what happens in some particular sample of photometry. These mathematical relations do, however, give us some hope in resolving the P_{act} and P_{rot} dilemma of FK Com, because they open up several indirect approaches. Here, indirect means that we do not solve the P_1 and P_2 periods simultaneously and directly. These indirect approaches are valid only if the real light curves $g_1(t)$ and $g_2(t)$ are sinusoids (Eqs. 30 and 31). For example, the relations of Eqs. 37 and 40 show that the shape of the sum curve $s(t)$ is sinusoidal with only one minimum and maximum. If this observed $s(t)$ light curve has two minima, the indirect approaches presented below are no longer valid because at least one of the real light curves $g_1(t)$ and $g_2(t)$ can not be a sinusoid.

It has already been mentioned in Sect. 7.4.2 that the period analysis of the observed light curve amplitudes A_3 may reveal the lap cycle period P_{lap} . The relation of Eq. 32 is easier to manipulate in the frequency domain, $f_{\text{lap}} = |f_1 - f_2| = \pm(f_1 - f_2)$. This gives

$$f_1 = \pm f_1 = f_{\text{lap}} \pm f_2 \quad (49)$$

We can use the equality $f_1 = \pm f_1$, because a negative f_1 value makes no sense in this particular context. Assuming that $f_2 = P_{\text{orb}}^{-1} \approx P_{\text{rot}}^{-1}$ in CABSs, the above relation gives two solutions for $f_1 = P_{\text{act}}^{-1}$ when $P_{\text{lap}} = f_{\text{lap}}^{-1}$ is known. If the signal of the P_{orb} period does not dominate the light curves, the migration of the light curve minimum epochs is tilted as a function of phase ϕ_2 with $P_2 = P_{\text{orb}} = f_2^{-1}$ (Eq. 5). During these time intervals, the forwards or backwards migration of these minima reveals if $P_{\text{act}}^{-1} = f_1 = f_{\text{lap}} + f_2$ or $P_{\text{act}}^{-1} = f_1 = f_{\text{lap}} - f_2$. Unfortunately, this relation of Eq. 49 does not help with any CASS, like FK Com.

There are three migration alternatives for the observed $s(t) = s_1(t) + s_2(t)$ light curve minima

- MIGRATION₁: If $a_1 \approx a_2$ (Eqs. 30 and 31), the migration is linear with $(f_1 + f_2)/2$ (Eq. 39)
- MIGRATION₂: If $a_1 < a_2$ (Eqs. 30 and 31), the migration is linear with f_2 and fluctuating (Eqs. 45 and 46)
- MIGRATION₃: If $a_1 > a_2$ (Eqs. 30 and 31), the migration is linear with f_1 and fluctuating (Eqs. 45 and 46)

It is not easy to unambiguously separate these three alternatives from each other in the real photometric observations. Nevertheless, we know at least that the stronger signal usually dominates the linear fluctuating migration (Eqs. 45-46), because it is reasonable to assume that the cases $a_1 \approx a_2$ occur less frequently than the cases $a_1 < a_2$ or $a_1 > a_2$. When the observed $s(t)$ light curve minima

$t_{\min,1}$ are analysed, e.g. with the K-method, the result can be f_1 , f_2 or $(f_1 + f_2)/2$, or none of these. Different migration alternatives of CABSs were displayed in Jetsu et al. (2017, Figs. 15-27: tilted non-stationary and horizontal stationary lines in panels “a”). We know now that there are at least three different migration alternatives even in the most simple case of two interacting sinusoids $s_1(t)$ and $s_2(t)$. For example, the minima of II Peg first concentrated close to $\phi_{\text{orb}} = 0.25$ between the years 1988 and 1997, and then these minima began to wander regularly away from this phase (Jetsu et al. 2017, their Fig. 27a). All available $t_{\min,1}$ light curve minima were used to determine the P_{act} value of this CABS. However, we know now that the result for P_{act} was not correct, because some $t_{\min,1}$ values, like those between the years 1988 and 1997, were certainly connected P_{orb} , but not to $P_{\text{act}} \neq P_{\text{orb}}$. For any particular star, the K-method may detect f_1 , f_2 or $(f_1 + f_2)/2$ depending of which one of the MIGRATION₁, MIGRATION₂ or MIGRATION₃ modes dominates. The long-term photometry of any CABS or CASS is a mixture of all these three migration alternatives, because the amplitudes $A_1 = 2a_1$ and $A_2 = 2a_2$ can change.

It may be possible to identify the time intervals when one of the above mentioned three migration modes dominates. For example, it is usually easy to notice the *particular* time intervals when P_{orb} dominates the $s(t)$ light curve minima of some CABS (Jetsu et al. 2017, e.g. II Peg). It may be possible to solve P_{act} by analysing the $t_{\min,1}$ values of the *other* remaining time intervals with the K-method. Finally, the observing seasons displaying a flip-flop event represent the MIGRATION₁ case having an exceptional amplitude and periodicity combination. It is very difficult to detect P_{orb} or P_{act} during these observing seasons when $A_1 \approx A_2$

In Sect. 6.2, we noted that our $|\Delta\Omega|$ values in Table 4 may be underestimates. The P_{act} values of some stars published by Jetsu et al. (2017) are too close to P_{orb} , because they used *all* $t_{\min,1}$ values in their K-method analysis. *Had* they excluded the $t_{\min,1}$ values connected to the P_{orb} periodicity before their K-method analysis, some $|P_{\text{orb}} - P_{\text{act}}|$ differences would have been larger. Hence, we have underestimated the $|\Delta\Omega|$ values in our Table 4. In some cases, the K-method may even have detected only the P_{orb} periodicity, because P_{act} never dominated the observed light curve. This may have happened for example with DM UMa (Jetsu et al. 2017, Fig. 15a).

Regardless of the minima-incompatibility, the three migration alternatives MIGRATION₁, MIGRATION₂ and MIGRATION₃ do provide the *qualitative* answers to the *4th question*, the *5th question* and the *6th question*, which are given in our conclusions (Sect. 17).

There are other indirect ways to obtain less important additional information. Firstly, the ratio a_1/a_2 can be estimated from the range of $\phi_{\min,1}$ fluctuation (Eq. 47). Secondly, if the observed $s(t)$ light curve amplitude A_3 repeats some regular pattern, the amplitudes $A_1 = 2a_1$ and $A_2 = 2a_2$ can be solved from Eqs. 43 and 44. This gives

$$A_1 = (A_{3,\max} - A_{3,\min})/2 \quad (50)$$

$$A_2 = (A_{3,\max} + A_{3,\min})/2 \quad (51)$$

where $A_{3,\max}$ and $A_{3,\min}$ are the maximum and minimum values of the *observed* amplitude A_3 .

Although the number of possible $g_1(t)$ and $g_2(t)$ combinations is infinite, the above indirect approaches give us

some hope of detecting the P_{act} and P_{rot} periodicities of FK Com. However, these indirect approaches rely on the assumption that the observed $s(t)$ light curve is a sum of two sinusoids. Even if this assumption were true, the interpretation of the observed light curves of FK Com would remain ambiguous, especially due to incompatibility. We have obtained *qualitative* answers to the *4th question*, the *5th question* and the *6th question*, but the *quantitative* estimates for the numerical values of P_{act} and P_{rot} are still missing. Hence, our current study is still at the dead encountered in Sect. 7.5.

8. New period analysis method

We do not have to rely on indirect solutions, like those presented in the previous Sect 7.7, because we can formulate an unambiguous solution for the P_{act} and P_{rot} periods of FK Com. Both periods can be solved simultaneously. This *quantitative* solution of the *4th question* and the *5th question* is presented here in Sects. 8-9.

8.1. Two period method (2P-method)

Let us assume that the correct periods for the 2P-model $g_C(t)$ are P_1 and P_2 . Their mean $P_{\text{mid}} = (P_1 + P_2)/2$ gives the frequency $f_{\text{mid}} = P_{\text{mid}}^{-1}$. A suitable range for the tested f_1 and f_2 values of the $g_C(t)$ model is between $f_{\text{min}} = (1-a)f_{\text{mid}}$ and $f_{\text{max}} = (1+a)f_{\text{mid}}$, where $P_{\text{mid}} = 2.4$ and $a = 0.03$, as in Eq. 34. This is the $\pm 3\%$ range at both sides of f_{mid} for both tested frequencies f_1 and f_2 . Our step in tested frequencies is

$$f_{\text{step}} = f_0/\text{OFAC}, \quad (52)$$

where $f_0 = 1/\Delta T$ and OFAC = 60 is the over-filling factor. For both f_1 and f_2 , we test all integer multiples of f_{step} between f_{min} and f_{max} . We have performed numerous tests to confirm that the above high OFAC value in Eq. 52 gives reasonably accurate values for the correct periods P_1 and P_2 , as well as for their errors.

For a pair of tested f_1 and f_2 values, the 2P-method periodogram is

$$z_C(f_1, f_2) = \sqrt{\left(\frac{1}{n}\right) \sum_{i=1}^n \epsilon_i^2} = \sqrt{R_C/n}, \quad (53)$$

where ϵ_i are the residuals of Eq. 13 ($[z_C] = \text{mag}$). When the numerical values of the tested f_1 and f_2 are fixed, the $g_C(t)$ model has only eight free parameters. These are the amplitudes B_1, B_2, C_1 and C_2 of Eq. 2, and D_1, D_2, E_1 and E_2 of Eq. 4. This model is linear, and the least squares fit solutions for these eight amplitudes are unambiguous. The frequencies $1/P_1$ and $1/P_2$ of the best periods for the data are at the *global* minimum of the $z_C(f_1, f_2)$ periodogram.

The errors of the model parameters with the best periods P_1 and P_2 are determined with the bootstrap procedure (Efron & Tibshirani 1986; Jetsu & Pelt 1999). During each bootstrap round, we select a random sample $\bar{\epsilon}^*$ from the residuals $\bar{\epsilon}$ of the best model $g_i = g_C(t_i)$ for the *original* data \bar{y} (Eq. 13). Any particular ϵ_i value of all n values can enter into this sample $\bar{\epsilon}^*$ as many times as the random selection happens to favour it. This random sample of residuals gives the sample of *artificial* data

$$y_i^* = g_i + \epsilon_i^* \quad (54)$$

during each bootstrap round. The 2P-method analysis of this artificial \bar{y}^* data sample gives one estimate for the model parameters $P_1, P_2, A_1, A_2, t_{g1,\text{min},1}, t_{g1,\text{min},2}, t_{g2,\text{min},1}$ and $t_{g2,\text{min},2}$. Our error estimate for each particular model parameter is the standard deviation of all estimates obtained for this model parameter in all bootstrap samples. We compute these standard deviations only from those bootstrap estimates, where the frequencies $1/P_1$ and $1/P_2$ of the best periods are inside the circle of Eq. 57 (see Sect 9.1.3). We neglect the cases where the solution for the best model for the bootstrap sample \bar{y}^* is outside this circle, because these solutions are not connected to the global minimum of $z_C(f_1, f_2)$. Such events are rare (see Sect. 9.1.7).

8.2. One period method (1P-method)

The range of the tested frequencies f_3 in the 1P-method is the same as that used for f_1 and f_2 in Sect. 8.1. The 1P-method periodogram is

$$z_S(f_3) = \sqrt{\left(\frac{1}{n}\right) \sum_{i=1}^n \epsilon_i^2} = \sqrt{R_S/n}, \quad (55)$$

where ϵ_i are the residuals of Eq. 14. The units are $[z_S] = \text{mag}$. The $P_3, A_3, t_{S,\text{min},1}$ and $t_{S,\text{min},2}$ error estimates are determined with a similar bootstrap procedure as already explained in the previous Sect. 8.1.

9. General notes of new period analysis method

For every segment, we show and discuss the following three period analysis figures

- The $z_C(f_1, f_2)$ periodogram giving the best periods P_1 and P_2 (e.g. Fig. 6)
- The $g_C(t)$ model results with P_1 and P_2 (e.g. Fig. 7)
- The $z_S(f_3)$ periodogram giving the best period P_3 and the $g_S(t)$ model results with P_3 (e.g. Fig. 8)

These three figures of the first segment, DATA_{2,1}, are used as examples of *how* the period analysis results are presented. Therefore, the period analysis results for DATA_{2,1} are not rediscussed in the Appendix, where we discuss the results for all other 21 segments.

9.1. 2P-method periodograms $z_C(f_1, f_2)$

Here, we discuss the general characteristics of *all* $z_C(f_1, f_2)$ periodograms. Our aim is to formulate as precise and objective characteristics as possible. We have to create these new concepts, because our period analysis results would be ambiguous without this transparent formulation. Our Table 6 summarizes which particular characteristics actualise in the $z_C(f_1, f_2)$ periodograms of individual segments.

The small blue-white rectangular area in the upper left corner of Fig. 6 displays the full $z_C(f_1, f_2)$ periodogram of DATA_{2,1}. This small rectangle is symmetric with respect to the diagonal $f_1 = f_2$ line because $z_C(f_1, f_2) = z_C(f_2, f_1)$. In other words, the same information is presented twice, i.e. once above or once below this diagonal line. Hence, we test only the triangular area below the diagonal line $f_1 = f_2$, where $f_1 > f_2$, or equivalently $P_1 < P_2$. The larger blue-white triangle shows the $z_C(f_1, f_2)$ values for

Table 6. Summary of $z_C(f_1, f_2)$ periodogram characteristics. The first three columns give the telescope (TEL), the segment (SEG) and the figure number (Fig.). The presence of a cross shape or white arms is tabulated in columns 4 and 5 (Sects. 9.1.1 and 9.1.2). The cases when $\pm f_0/2$ or $\pm 3\sigma_{f_1, f_2}$ limit hits $f_1 = f_2$ are given in columns 6 and 7 (Sects. 9.1.3 and 9.1.4). The $g_C(t)$ models having amplitude dispersion or high amplitude ratio are given in columns 8 and 9 (Sects. 9.1.5 and 9.1.6). The cases having bootstrap sample results outside $\pm f_0/2$ are tabulated in the column 10 (Sect. 9.1.7). The last five columns denote when the 2P-model breaks down (Sect. 9.1.8), conservative model periods (Sect. 9.4), liberal model periods (Sect. 9.4), critical level Q_F (Eq. 16) and when the stronger periodicity of the entire segment is present in the 1st or 2nd part of the segment (Sect. 9.5: Eq. 60).

1.	2.	3.	4.	5.	6.	7.	8.	9.	10.	11.	12.	13.	14.	15.
TEL	SEG	Fig.	cross shape	white arms	$\pm f_0/2$ limit hits $f_1 = f_2$	$\pm 3\sigma_{f_1, f_2}$ limit hits $f_1 = f_2$	amplitude dispersion	high amplitude ratio	bootstrap outside $\pm f_0/2$	2P-model breaks down	conservative model periods	liberal model periods	Q_F	stronger period same in $\Delta T/2$
2	1	6	Yes	No	Yes	Yes	Yes	No	No	CASE ₁	P_3	P_3	No	1st, 2nd
2	2	A.1	Yes	Yes	Yes	Yes	Yes	No	Yes	CASE ₁	P_3	P_3	No	1st, 2nd
2	3	A.4	Yes	No	Yes	Yes	Yes	No	No	CASE ₁	P_3	P_3	No	No, No
1	1	A.7	Yes	No	No	No	No	Yes	No	CASE ₂	P_3	P_1, P_2	6.6×10^{-8}	1st, 2nd*
2	4	A.10	No	No	No	No	No	No	No	No	P_1, P_2	P_1, P_2	8.7×10^{-15}	1st, 2nd*
1	2	A.13	No	No	No	No	No	No	No	No	P_1, P_2	P_1, P_2	$\ll 10^{-16}$	1st*, 2nd
2	5	A.16	Yes	Yes	No	No	No	Yes	No	CASE ₂	P_3	P_1, P_2	2.7×10^{-10}	1st, 2nd*
1	3	A.19	Yes	Yes	No	No	No	Yes	Yes	CASE ₃	P_3	P_1, P_2	9.6×10^{-4}	–
2	6	A.22	Yes	Yes	Yes	No	No	Yes	No	CASE ₁ , CASE ₂	P_3	P_1, P_2	$\ll 10^{-16}$	No, 2nd
1	4	A.25	Yes	Yes	Yes	Yes	Yes	No	No	CASE ₁	P_3	P_3	No	1st, 2nd
2	7	A.28	Yes	No	No	No	No	No	No	No	P_1, P_2	P_1, P_2	$\ll 10^{-16}$	1st*, No
1	5	A.31	Yes	No	No	No	No	No	No	No	P_1, P_2	P_1, P_2	$\ll 10^{-16}$	1st, No
1	6	A.34	Yes	Yes	No	No	No	Yes	No	CASE ₃	P_3	P_1, P_2	2.8×10^{-8}	1st*, 2nd
2	8	A.37	Yes	Yes	No	No	No	Yes	Yes	CASE ₃	P_3	P_1, P_2	8.6×10^{-4}	1st, 2nd
1	7	A.40	Yes	No	Yes	No	No	No	No	CASE ₁	P_3	P_1, P_2	7.8×10^{-10}	1st, 2nd*
2	9	A.43	Yes	No	Yes	Yes	Yes	No	Yes	CASE ₁	P_3	P_3	No	1st, 2nd
1	8	A.46	Yes	No	Yes	No	No	No	No	CASE ₁	P_3	P_1, P_2	$\ll 10^{-16}$	1st, No
1	9	A.49	No	No	Yes	No	No	No	No	CASE ₁	P_3	P_1, P_2	$\ll 10^{-16}$	1st*, 2nd*
1	10	A.52	Yes	No	Yes	No	Yes	No	No	CASE ₁	P_3	P_1, P_2	$\ll 10^{-16}$	1st*, 2nd*
1	11	A.55	Yes	No	No	No	No	No	No	CASE ₁	P_1, P_2	P_1, P_2	$\ll 10^{-16}$	No, 2nd
1	12	A.58	No	No	Yes	Yes	Yes	No	No	CASE ₁	$(P_1 + P_2)/2$	$(P_1 + P_2)/2$	No	1st, 2nd
1	13	A.61	Yes	No	Yes	Yes	Yes	No	No	CASE ₁	P_3	P_3	No	1st, 2nd

$f_2 < (1 - b)f_1$, where the $b = 0.01$ prevents the testing of CASE₁ when the least squares fit of Eq. 6 becomes unstable. The weak diagonal stripe seen in the small rectangle in the upper corner of Fig. 6 shows that this instability is indeed present.

All $z_C(f_1, f_2)$ periodograms are displayed in blue-white colour scale using ten different shades. The white colour denotes the minimum level $z_{C, \min}$, while the dark blue colour denotes the maximum level $z_{C, \max}$ of this two-dimensional periodogram. If there is no periodicity with the tested f_1 and f_2 pair, a suitable model for y_i^j is the mean $g_C(t) = m_{y^j}$, and in this case the dark blue “continuum level” of the $z_{C, \max}$ periodogram of Eq. 53 is equal to σ_{y^j} . The numerical value of the white level at $z_{C, \min}$ depends on, e.g. the quality of data, the stability of the light curve or the length ΔT of the segment. Hence, the dark blue $z_{C, \max}$ and the white $z_{C, \min}$ colour levels are different in every segment.

The large green cross in Fig. 6 denotes the location of the frequencies $1/P_1$ and $1/P_2$ of the two best periods for DATA_{2,1}. The phase difference with these two frequencies is only $\Delta\phi_{1,2} = 0.03$ during ΔT . The locations of the first 50 bootstrap estimates for $1/P_1$ and $1/P_2$ are shown with filled red circles. The frequency level of the best period P_3 (see Fig. 8) detected with the 1P-method is denoted with vertical and horizontal continuous red lines.

9.1.1. Characteristic: cross shape

A cross shape of $z_C(f_1, f_2)$ can be seen in the small blue-white rectangle in the upper left corner of Fig. 6. Two of the four arms of this cross are visible in the larger blue-white triangle of the same figure. This characteristic is present in numerous other periodograms (Table 6: cross shape=“Yes”). The continuous red vertical and horizontal lines denoting the frequency level for the best period P_3 of the 1P-model coincide with this cross shape in Fig. 6. This geometrical consistence between the arms of the cross and these red lines indicates that the best value for $f_1 = 1/P_1$ or $f_2 = 1/P_2$ is close to $f_3 = 1/P_3$. If the frequency f_1 is fixed to $1/P_3$, nearly all tested values of f_2 give a reasonable fit to the data (vertical arm). Or, if the frequency f_2 is fixed to $1/P_3$, then nearly all tested values of f_1 give a reasonable fit to the data (horizontal arm). The presence of this cross shape indicates that the 1P-model may be the best model for the segment. The absence of this cross shape characteristic means that the 2P-model may be a better choice (Table 6: cross shape=“No”).

9.1.2. Characteristic: white arms

The arms of the cross of $z_C(f_1, f_2)$ periodogram in Fig. 6 get a bit bluer further away from the diagonal line $f_1 = f_2$.

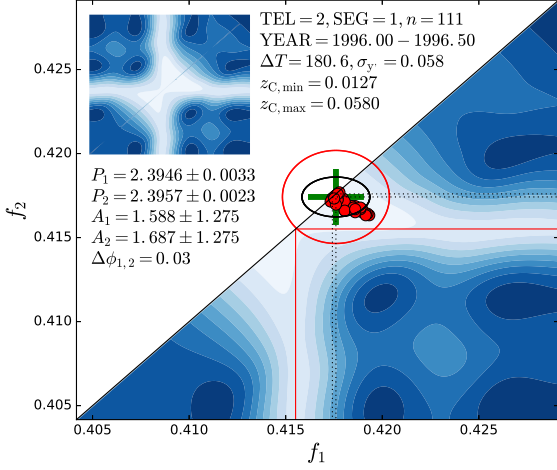


Fig. 6. DATA_{2,1}. The $n = 111$ observations y_i between 1996.00 and 1996.50 have $\Delta T = 180.^d6$ and $\sigma_{y'} = 0.^m058$. The small blue-white rectangle in the upper left corner shows the full $z_C(f_1, f_2)$ periodogram of Eq. 53. The colour scale of $z_C(f_1, f_2)$ has ten different shades between minimum and maximum values $z_{C,\min} = 0.^m0127$ (white) and $z_{C,\max} = 0.^m0580$ (dark blue). The large blue-white triangle shows the same $z_C(f_1, f_2)$ periodogram for $f_2 < (1 - b)f_1$, where $b = 0.01$. The diagonal continuous black line shows the $f_1 = f_2$ level. The large green cross denotes the frequencies of the best periods $1/P_1$ and $1/P_2$, i.e. the location of the best $g_C(t)$ model. The red circle of Eq. 57 and the black ellipse of Eq. 58 surround this location. The frequency levels $1/P_1$ and $1/P_2$ of the best periods are shown with vertical and horizontal dark dotted lines. The small filled red circles denote the estimates for these periods in the first 50 bootstrap samples. The amplitudes A_1 and A_2 are also given, as well as the phase difference $\Delta\phi_{1,2}$ with the periods P_1 and P_2 during ΔT . The frequency level $1/P_3$ for the best period of the 1P-model from Fig. 8 is shown with a continuous vertical and horizontal red line.

However, there are several cases where these arms are white all the way from the diagonal to the edge of the periodogram (Table 6: white arms=“Yes”). These white arms are an even stronger indication of that the 1P-model is the correct model for the data. In these cases, either the A_1 amplitude is much weaker than the A_2 amplitude, or vice versa. This means that the $g_1(t)$ or the $g_2(t)$ part dominates the best $g_C(t)$ solution, or equivalently $g_C \rightarrow g_S$ (Eq. 11 or 12). On the other hand, the absence of white arms indicates that the 1P-model is not necessarily the best model (Table 6: white arms=“No”).

9.1.3. Characteristic: $\pm f_0/2$ limit hits $f_1 = f_1$

In many period finding methods, the distance between independent tested frequencies is

$$f_0 = 1/\Delta T, \quad (56)$$

where $\Delta T = t_n - t_1$. The relation $(f \pm f_0)\Delta T = f\Delta T \pm 1$ shows what happens if f_0 is added to, or subtracted from, any tested frequency f . This equals one round more or less during ΔT . When the data are modelled as a function of phase (e.g. Eqs. 3, 5 or 8), a shift from any tested f to $f + f_0$ or $f - f_0$ completely rearranges these phases. For this

reason, the values of many periodograms correlate within an interval of $\pm f_0/2$, and the presence of this correlation can even be checked (e.g. Jetsu & Pelt 1996, Fig. 2). We will display all $z_C(f_1, f_2)$ periodograms together with the superimposed red circle

$$[(f_1 - P_1^{-1})/(f_0/2)]^2 + [(f_2 - P_2^{-1})/(f_0/2)]^2 = 1, \quad (57)$$

where f_1 and f_2 are the tested periods of the model, and P_1 and P_2 are the two best periods for the 2P-model (e.g. Fig. 6). It is also geometrically evident that the distance between independent frequencies is about $\pm f_0/2$, because the width of the cross shape in our $z_C(f_1, f_2)$ periodograms is of the same order as the diameter of this red circle.

The segments where the red circle of Eq. 57 intersects the diagonal line $f_1 = f_2$ are given in Table 6 ($\pm f_0/2$ limit hits $f_1 = f_2$ =“Yes”). In this case, the 2P-method can not necessarily detect both periods P_1 and P_2 simultaneously, even if these periods were the correct periods for the data. This $\pm f_0/2$ relation also means that the closer the two best periods P_1 and P_2 of the 2P-model are to each other, the longer is the required time span ΔT to detect these periods.

9.1.4. Characteristic: $\pm 3\sigma_{f_1, f_2}$ limit hits $f_1 = f_1$

We also compute and show the curve

$$[(f_1 - P_1^{-1})/(3\sigma_{f_1})]^2 + [(f_2 - P_2^{-1})/(3\sigma_{f_2})]^2 = 1. \quad (58)$$

where σ_{f_1} and σ_{f_2} are their errors of the frequency levels of the best periods P_1 and P_2 . This curve is displayed as a black ellipse in all our 2P-method periodograms (e.g. Fig. 6). We use a compact notation “ $\pm 3\sigma_{f_1, f_2}$ ” for this black ellipse of Eq. 58. The segments where this black ellipse intersects the diagonal line $f_1 = f_2$ are given in Table 6 ($\pm 3\sigma_{f_1, f_2}$ limit hits $f_1 = f_2$ =“Yes”). When this happens, the quality of the data may prevent the simultaneous detection of periods P_1 and P_2 even if these were the correct real periods.

9.1.5. Characteristic: amplitude dispersion

The amplitudes A_1 and A_2 in Fig. 6, as well as their errors, are unrealistic because the best $g_C(t)$ model is so close to the $f_1 = f_2$ line. We shall hereafter refer to this characteristic as amplitude dispersion in Table 6 (amplitude dispersion=“Yes”). In this particular case of Fig. 6, the A_1 and A_2 values are unreasonably large, and their bootstrap error estimates σ_{A_1} and σ_{A_2} also disperse. There are other cases, where the A_1 and A_2 estimates are reasonable, and only the error estimates σ_{A_1} and σ_{A_2} disperse (see Sect. A.2: Fig. A.4). This amplitude dispersion characteristic is connected to CASE₁ (Eq. 10).

9.1.6. Characteristic: high amplitude ratio

The amplitude ratio

$$R_A = \max[A_1/A_2, A_2/A_1] \quad (59)$$

measures the relative strength of the $g_1(t)$ and $g_2(t)$ parts of the 2P-model. This ratio is high when $g_C \rightarrow g_S$ in CASE₂ or CASE₃ (Eqs. 11 and 12). The segments where this occurs are given in Table 6 (high amplitude ratio=“Yes”).

9.1.7. Characteristic: bootstrap outside $\pm f_0/2$

There are a few cases where the best model of some bootstrap sample is outside the red circle of Eq. 57. This does not occur in Fig. 6. The cases where this occurs are marked with large red “x” in some figures (Table 6: bootstrap outside $\pm f_0/2$ =”Yes”). Only eleven such events occur in the first 50 bootstrap samples of 22 segments. These are displayed in Figs. A.1 (two red “x”), Figs. A.19 (five red “x”), Figs. A.37 (one red “x”) and Figs. A.43 (four red “x”). This gives the probability $0.011 = 12/(22 \times 50)$ for these events. The 2P-model does not break down in such cases. These events only indicate that the *global* $z_C(f_1, f_2)$ minimum is so shallow that the best solution for some bootstrap samples may occur outside the red circle of Eq. 57 at some other *local* $z_C(f_1, f_2)$ minimum. As explained earlier in Sect 8.1, these bootstrap models outside this red circle are not used in computing the errors of the 2P-model parameters $P_1, P_2, A_1, A_2, t_{g1,min,1}, t_{g1,min,2}, t_{g2,min,1}$ and $t_{g2,min,2}$.

9.1.8. Characteristic: 2P-model breaks down

The $g_C(t)$ model in Fig. 6 breaks down (Eq. 9), because the best solution is so close to the $f_1 = f_2$ diagonal line (Table 6: 2P-model breaks down=”CASE₁”). In this particular break down of Eq. 10, there is amplitude dispersion, the $\pm f_0/2$ limit hits $f_1 = f_2$ and the $\pm 3\sigma_{f_1, f_2}$ limit hits $f_1 = f_2$ (see Table 6).

There are other segments where the 2P-model breaks down due to CASE₂ (Eq. 11) or CASE₃ (Eq. 12). These segments are denoted as 2P-model breaks down=”CASE₂” or “CASE₃” in Table 6. The first such segments are DATA_{1,1} (Sect. A.3: CASE₂) and DATA_{1,3} (Sect. A.7: CASE₃).

There is one segment, DATA_{2,6} (Sect. A.8), where both CASE₁ and CASE₂ break down take place (Table 6: 2P-model breaks down=”CASE₁,CASE₂”).

9.2. $g_C(t)$ model results

The original data y_i and a second order polynomial fit h_i to these data are shown in Fig. 7a (red and blue filled circles). The mean brightness is removed in Fig. 7b which shows the y'_i of Eq. 1 (red filled circles) and the best 2P-model $g_C(t)$ (blue continuous line). Except for a few outliers, the residuals ϵ_i of Eq. 13 indicate that this model would fit the data quite nicely (Fig. 7c: red filled circles). This $g_C(t)$ model has $z_{C,min} = 0.^m0127$ (Fig. 6) which would be a very good result considering that the $n = 111$ observations cover a time interval of six months. However, we have already concluded that the $g_C(t)$ model breaks down (Eq. 10: CASE₁), and therefore the solutions for the $g_1(t)$ and $g_2(t)$ light curves with $A_1 \approx 1.^m6$ and $A_2 \approx 1.^m7$ are unrealistic (Fig. 7d: green and red continuous lines). These light curves and the data are also displayed as function of phase (Eqs. 3 and 5) in Figs. 7ef, where we give the first epochs of the primary minima $t_{g1,min,1}$ and $t_{g2,min,1}$ of these two curves. In this particular segment, neither one of these two light curves has a secondary minimum.

9.3. $z_S(f_3)$ periodogram and $g_S(t)$ model results

The 1P-method periodogram $z_S(f_3)$ of Eq. 55 is shown in Fig. 8a (continuous red line). The location of the best period P_3 is denoted with a red vertical line. This pe-

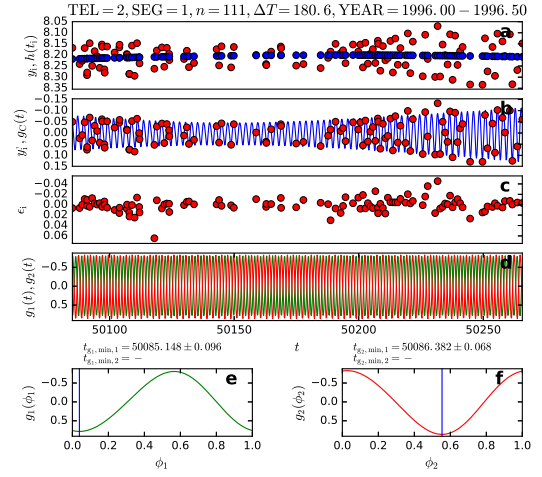


Fig. 7. DATA_{2,1}. (a) Original y_i data (filled red circles) and a second order polynomial fit h_i (filled blue circles). (b) Analysed y'_i data of Eq. 1 (filled red circles) and the model $g_C(t)$ (continuous blue line) with the best periods P_1 and P_2 from Fig. 6. (c) Residuals ϵ_i of the $g_C(t)$ model (Eq. 13). (d) $g_1(t)$ of Eq. 2 (continuous green line) and function $g_2(t)$ of Eq. 4 (continuous red line). (e) $g_1(\phi_1)$ as a function of phase of Eq. 3 (continuous green line). The epoch of the primary minimum, $t_{g1,min,1}$, is given above the panel. Vertical blue line denotes its phase. In this segment, the $g_1(\phi_1)$ function has no secondary minimum ($t_{g1,min,2} = "-"$). (f) $g_2(\phi_2)$ as a function of phase of Eq. 5 (continuous red line). The epoch of the primary minimum, $t_{g2,min,1}$, is given above the panel. Vertical blue line denotes its phase. This $g_2(\phi_2)$ function has no secondary minimum ($t_{g2,min,2} = "-"$).

riod deviates considerably from the best periods P_1 and P_2 determined with the 2P-method (dotted vertical lines). The amplitude of the best $g_S(t)$ model is high, $A_1 = 0.^m149 \pm 0.^m005$. The LS-method periodogram $z_{LS}(f_3)$ is shown in Fig. 8b (continuous blue line). The result for the best period (vertical blue line) overlaps the red vertical line denoting P_3 (i.e. not visible). In other words, the 1P-method and the LS-method period analysis of DATA_{2,1} give the same results. The y'_i data and the $g_S(t)$ model are shown in Fig. 8c (red filled circles and blue continuous line). It is evident that this constant amplitude 1P-model can not adjust to the changes of the light curve of FK Com during six months. For this reason, the scatter of the residuals ϵ_i of Eq. 14 increases towards the end of this segment (Fig. 8d). Hence, the $z_{S,min} = 0.^m0209$ value of this 1P-model in Fig. 8 clearly exceeds the $z_{C,min} = 0.^m0127$ value of the 2P-model in Fig. 6. The same $z_{S,min}(t)$ model and the data are shown as function of phase ϕ_3 in Fig. 6e, where we also give the epoch of the primary minimum $t_{S,min,1}$. This particular 1P-model has no secondary minimum $t_{S,min,2}$.

No temporally overlapping TEL=1 data is available for checking the results presented here for DATA_{2,1}.

9.4. Conservative and liberal models

There are limitations for the simultaneous detection of two periodic signals in the photometry of a variable star. We use the distance between independent frequencies, $f_0 = \Delta T^{-1}$ (Eq. 56), in the CASE₁ break down of the 2P-model (Sect. 9.1.3). For example, Loumos & Deeming (1978) have ar-

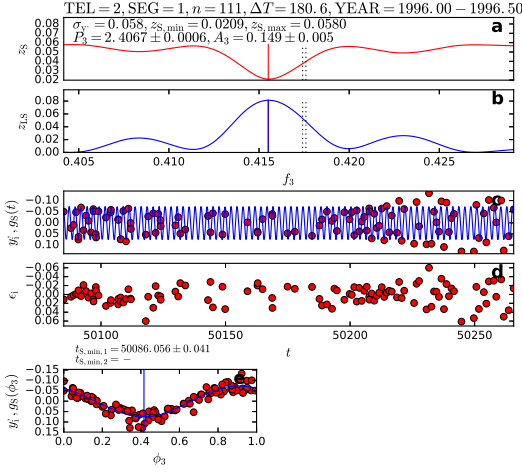


Fig. 8. DATA_{2,1}. (a) Periodogram $z_S(f_3)$ of Eq. 55 (continuous red line). Parameters n , ΔT , YEAR and σ_y are the same as in Fig. 6. Minimum and maximum levels of $z_S(f_3)$ are $z_{S,\min} = 0.^m0209$ and $z_{S,\max} = 0.^m0580$. The best period P_3 is denoted with a red vertical line. The amplitude A_3 is also given. Vertical dotted lines show the locations of P_1 and P_2 from Fig. 6. (b) The LS-method periodogram $z_{LS}(f_3)$ of Scargle (1982, Eqs. 10 and 11: blue continuous line). Blue vertical line denotes the location of the best period. Vertical dotted lines denote the locations of P_1 and P_2 from Fig. 6. Location of P_3 (red vertical line) is not seen in this particular segment because it coincides with the vertical blue line, i.e. the frequency of $z_S(f_3)$ minimum coincides with the frequency of $z_{LS}(f_3)$ maximum. (c) Data y'_i (filled red circles) and $g_S(t)$ model with P_3 (continuous blue line). (d) Residuals ϵ_i of Eq. 14. (e) $g_S(\phi_3)$ curve as a function of phase of Eq. 8 (continuous blue line). The epoch of the primary minimum, $t_{S,\min,1}$, is given above the panel and a vertical blue line denotes its phase. There is no secondary minimum $t_{S,\min,2}$ in this $g_S(\phi_3)$ curve.

gued that an even larger value, $1.5f_0 = 1.5(\Delta T)^{-1}$, should be used. The $\pm 3\sigma_{f_1, f_2}$ black ellipse of Eq. 58 is inside the $\pm f_0/2$ red circle of Eq. 57 in the $z_C(f_1, f_2)$ periodograms of *all* segments. Intuitively, this is logical. If the data samples are large, the parameters of the 2P-model can be estimated very accurately. In the extreme case, one could obtain such a large sample of accurate data that the $\pm 3\sigma_{f_1, f_2}$ black ellipse of Eq. 58 is reduced into a single point. This accuracy argument applies also to the other 2P-model parameters $A_1, A_2, t_{g1,\min,1}, t_{g1,\min,2}, t_{g2,\min,1}$ and $t_{g2,\min,2}$. The argument by Loumos & Deeming (1978) referred to the limitations in unambiguously separating two peaks of the LS-method periodogram from each other, i.e. they discussed this problem in the Fourier transformation context. Their argument is not connected to finding the unambiguous *global* minimum of a least squares fit of a linear model, where the tested frequencies f_1 and f_2 are fixed to known numerical values.

In fact, there are numerous sound statistical alternatives that could be used to choose the above mentioned limiting values, e.g. $\pm f_0/2, \pm 1.5f_0/2, \pm 1\sigma_{f_1, f_2}, \pm 2\sigma_{f_1, f_2}$ or $\pm 3\sigma_{f_1, f_2}$. Since we do not want to tie ourselves down to only one interpretation, we select a conservative and a liberal correct model for every segment. We apply objective

preassigned criteria in deciding between these conservative and liberal models.

In choosing the *conservative* model for a segment, we reject the 2P-model if even one of the following criteria is fulfilled

- CASE₁: $\pm f_0/2$ limit hits $f_1 = f_2$ ="Yes", $\pm 3\sigma_{f_1, f_2}$ limit hits $f_1 = f_2$ ="Yes" or amplitude dispersion="Yes" in Table 6
- CASE₂: high amplitude ratio="Yes" in Table 6
- CASE₃: high amplitude ratio="Yes" in Table 6

If any of these rejections takes place, the correct conservative model for the segment is the 1P-model. In other words, we reject all statistically non-independent P_1^{-1} and P_2^{-1} frequencies (CASE₁: $\pm f_0/2$ limit hits $f_1 = f_2$), all inaccurate frequencies (CASE₁: $\pm 3\sigma_{f_1, f_2}$ limit hits $f_1 = f_2$), all unstable models (CASE₁: amplitude dispersion) and all weaker periodic signals (CASE₂ or CASE₃).

In choosing the *liberal* model for a segment, we reject the 2P-model if, and only if, the criterion

- CASE₁: $\pm 3\sigma_{f_1, f_2}$ limit hits $f_1 = f_2$ ="Yes" in Table 6

is fulfilled, or equivalently $P_1^{-1} \approx P_2^{-1}$. If this rejection takes place, the correct liberal model for the segment is the 1P-model.

If the 2P-model is the conservative or the liberal model, we give the critical level Q_F in Table 6. We do not discuss the critical level Q_F (Eq. 16) of every segment, because in every case these critical levels support the conclusion that the 2P-model is a better model than the 1P-model, i.e. the null hypothesis H_0 made in Sect. 3.3 must be rejected.

Since the $3 \pm \sigma_{f_1, f_2}$ limit hits the $f_1 = f_2$ diagonal in DATA_{2,1} (Fig. 6), we conclude that the 1P-model is both the conservative and the liberal model in this segment DATA_{2,1}. Therefore, the results for this particular segment are the same in Tables 7-8 and 9-10.

9.5. Stronger period same in $\Delta T/2$

We divide the data of every segment into two parts having approximately the same length $\Delta T/2$. Our aim is to check, if the same periodicity is present in the 1st and the 2nd part of the segment. The DATA_{1,3} segment is not divided into two parts, because it contains only $n = 69$ observations. Both parts of the other 21 segments are analysed separately. For obvious reasons, we do not display the corresponding $2 \times 3 \times 21 = 126$ additional figures here. We check if the stronger periodic signal detected in the liberal model of the entire segment is also present in the liberal models of both parts of the same segment. We compute the difference

$$\Delta P_{\text{ent,part}} = |P_{\text{ent}} - P_{\text{part}}| / \sigma_{P_{\text{part}}},$$

where P_{ent} is the strongest periodicity for the entire segment and $P_{\text{part}} \pm \sigma_{P_{\text{part}}}$ is a period detected in the 1st or the 2nd part of the segment. This parameter $\Delta P_{\text{ent,part}}$ measures the P_{ent} and P_{part} difference in units of $\sigma_{P_{\text{part}}}$. Our criterion for the detection of the same period is

$$\Delta P_{\text{ent,part}} \leq 3. \quad (60)$$

These detections are classified to the following five categories in our Table 6

- 1st = Criterion of Eq. 60 is fulfilled in the 1st part

Table 7. Conservative model mean, period and amplitude. The three first columns give the telescope (TEL), the segment (SEG) and the mean of all observing times (YEAR). The next column gives the mean and the error of the mean of all y_i within the segment (M). If the 2P-model is the conservative model, the periods and amplitudes of the $g_1(t)$ and $g_2(t)$ functions are given (Columns P_1, P_2, A_1 and A_2). If the 1P-model is the conservative model, we give its period and amplitude (Columns P_3 and A_3). All results given in this table are presented in Fig. 9.

TEL	SEG	YEAR	M	P_1	P_2	P_3	A_1	A_2	A_3
		[y]	[mag]	[d]	[d]	[d]	[mag]	[mag]	[mag]
2	1	1996.25	8.2060±0.0055	–	–	2.4067±0.0006	–	–	0.149±0.005
2	2	1997.23	8.2337±0.0037	–	–	2.4064±0.0005	–	–	0.140±0.003
2	3	1998.21	8.2036±0.0018	–	–	2.3951±0.0010	–	–	0.052±0.004
1	1	1998.28	8.2032±0.0012	–	–	2.3961±0.0014	–	–	0.041±0.003
2	4	1999.19	8.1792±0.0019	2.3810±0.0010	2.4208±0.0017	–	0.041±0.003	0.032±0.003	–
1	2	1999.22	8.1747±0.0011	2.3803±0.0007	2.4217±0.0008	–	0.040±0.002	0.032±0.002	–
2	5	2000.19	8.2623±0.0038	–	–	2.3959±0.0004	–	–	0.125±0.004
1	3	2000.24	8.2576±0.0054	–	–	2.3980±0.0009	–	–	0.118±0.005
2	6	2001.19	8.3019±0.0050	–	–	2.4023±0.0004	–	–	0.194±0.004
1	4	2001.26	8.2983±0.0076	–	–	2.4020±0.0004	–	–	0.198±0.005
2	7	2002.20	8.2998±0.0033	2.3903±0.0010	2.4136±0.0012	–	0.071±0.006	0.069±0.005	–
1	5	2002.24	8.2903±0.0034	2.3894±0.0007	2.4097±0.0008	–	0.054±0.004	0.084±0.004	–
1	6	2003.17	8.2394±0.0030	–	–	2.3961±0.0007	–	–	0.102±0.003
2	8	2003.21	8.2428±0.0032	–	–	2.3978±0.0009	–	–	0.092±0.005
1	7	2004.13	8.1844±0.0042	–	–	2.4019±0.0007	–	–	0.119±0.004
2	9	2004.23	8.1928±0.0050	–	–	2.4063±0.0008	–	–	0.136±0.007
1	8	2005.23	8.2483±0.0034	–	–	2.3961±0.0006	–	–	0.124±0.005
1	9	2006.22	8.2432±0.0034	–	–	2.4139±0.0006	–	–	0.107±0.005
1	10	2007.26	8.2548±0.0053	–	–	2.3936±0.0005	–	–	0.187±0.005
1	11	2008.21	8.3074±0.0045	2.3808±0.0012	2.4062±0.0008	–	0.077±0.005	0.137±0.005	–
1	12	2009.23	8.2816±0.0032	–	–	2.4043±0.0006	–	–	–
1	13	2010.12	8.2916±0.0037	–	–	2.3895±0.0010	–	–	0.115±0.005

- 2st = Criterion of Eq. 60 is fulfilled in the 2nd part
- 1st* = Criterion of Eq. 60 is fulfilled in the 1st part, but the 2P-model can not be the liberal model, because “ $\pm 3\sigma_{f_1, f_2}$ hits $f_1 = f_2$ ”.
- 2nd* = Criterion of Eq. 60 is fulfilled in the 2nd part, but the 2P-model can not be the liberal model, because “ $\pm 3\sigma_{f_1, f_2}$ hits $f_1 = f_2$ ”.
- No = Criterion of Eq. 60 is not fulfilled.

This kind of an analysis suffers from a trade-off. The simultaneous detection of two periodicities P_1 and P_2 is much more difficult when the time span of data is reduced to $\Delta T/2$. It is therefore no surprise, if only one, or neither one, of the periodicities of the entire segment is detected in the 1st or the 2nd part of the segment. However, it is logical to expect that some signs of the stronger periodicity of the entire segment are detected in both parts of the segment. The above mentioned trade-off is also the reason why we accept the two categories “1st*” and “2nd*” as detections.

The criterion of Eq. 60 is not fulfilled in only six parts out of a total of $21 \times 2 = 42$ parts (Table 6: stronger period same in $\Delta T/2 =$ “No”). There is only one segment where the criterion of Eq. 60 is not fulfilled in both parts of the segment. In this case of DATA_{2,3}, the two periods $P_1 = 2.^d4015$ and $P_1 = 2.^d4084$ shown in Fig. A.4 are present in the 1st and 2nd part of this segment. However, the 2P-model is not accepted as the liberal model for the entire segment because “ $\pm 3\sigma_{f_1, f_2}$ hits $f_1 = f_2$ ” (Sect. A.2). If the criterion “ $\pm 2\sigma_{f_1, f_2}$ hits $f_1 = f_2$ ” had been used, then the above two periodicities of the 2P-model would have been detected with criterion of Eq. 60 in the 1st and 2nd part of this segment. All the above mentioned detections, $(42 - 4)/42 \equiv 90.5\%$, strongly indicate that the detected

periodicities are stable *within* the segments that sometimes span over six or seven months.

In the previous Sects. 8-9, we use the results for DATA_{2,1} to illustrate *how* our new period analysis method works. Therefore, we remind the reader again that the 2P-method analysis results for all other 21 segments are discussed thoroughly in our Appendix (Sects. A.1-A.21).

10. Conservative model

The conservative model results are given in Tables 7-8 and Figs. 9a-f.

The long-term mean brightness M changes of FK Com are quasi-periodic (Fig. 9a). The maxima are about five years apart (1999 and 2004), while the time difference between the minima is about seven years (2001 and 2008). There is some uncertainty in the scale of these M changes, because Hackman et al. (2013) noticed that the magnitude difference between the photometric check star HD 117876 and the comparison star HD 117567 was not constant. However, they concluded that the brightness of the comparison star has remained constant and only the check star has varied, i.e. the scale of these M changes of FK Com should be correct.

The period changes are shown in Fig. 9b. The 1P-model is the conservative model in seventeen segments ($P_3 =$ green filled diamonds). In only five segments, the 2P-model is the conservative model ($P_1 =$ red filled circles, $P_2 =$ blue filled circles). These P_1 and P_2 periods are discussed later in the next Sect. 11.

The weighted mean of all P_3 values is

$$P_{w,1} \pm \Delta P_{w,1} = 2.^d4009 \pm 0.^d0055 \quad (n = 17). \quad (61)$$

Table 8. Conservative model minimum epochs. The three first columns TEL, SEG and YEAR are the same as in Table 7. If the 2P-model is the conservative model, the minimum epochs of the $g_1(t)$ and $g_2(t)$ functions are given on columns $t_{g1,\min,1}$, $t_{g1,\min,2}$, $t_{g2,\min,1}$ and $t_{g2,\min,2}$. If the 1P-model is the conservative model, the minimum epochs of the $g_S(t)$ function are given on columns $t_{S,\min,1}$ and $t_{S,\min,2}$.

TEL	SEG	YEAR	$t_{g1,\min,1}$	$t_{g1,\min,2}$	$t_{g2,\min,1}$	$t_{g2,\min,2}$	$t_{S,\min,1}$	$t_{S,\min,2}$
		[y]	[HJD - 2400000]					
2	1	1996.25	—	—	—	—	50086.056±0.041	—
2	2	1997.23	—	—	—	—	50412.955±0.032	—
2	3	1998.21	—	—	—	—	50779.712±0.100	—
1	1	1998.28	—	—	—	—	50851.002±0.059	—
2	4	1999.19	51145.492±0.055	51144.537±0.071	51146.438±0.112	—	—	—
1	2	1999.22	51155.039±0.038	—	51153.468±0.071	—	—	—
2	5	2000.19	—	—	—	—	51508.072±0.024	—
1	3	2000.24	—	—	—	—	51534.349±0.040	—
2	6	2001.19	—	—	—	—	51874.456±0.022	—
1	4	2001.26	—	—	—	—	51884.040±0.030	—
2	7	2002.20	52242.585±0.049	52243.378±0.079	52243.870±0.104	—	—	—
1	5	2002.24	52248.229±0.059	52249.835±0.050	52248.758±0.049	—	—	—
1	6	2003.17	—	—	—	—	52614.767±0.025	—
2	8	2003.21	—	—	—	—	52614.688±0.048	—
1	7	2004.13	—	—	—	—	52979.786±0.063	—
2	9	2004.23	—	—	—	—	52972.470±0.087	—
1	8	2005.23	—	—	—	—	53344.382±0.036	—
1	9	2006.22	—	—	—	—	53722.822±0.029	—
1	10	2007.26	—	—	—	—	54076.975±0.026	—
1	11	2008.21	54440.885±0.058	—	54442.056±0.054	—	—	—
1	12	2009.23	—	—	—	—	—	—
1	13	2010.12	—	—	—	—	55174.413±0.034	55173.029±0.051

The continuous green line shows this $P_{w,1}$ level in Fig. 9b, while the two dotted green lines show the $P_{w,1} \pm \Delta P_{w,1}$ levels. We will hereafter refer to these seventeen periods as the $P_{w,1}$ -group. For some reason, it seems as if these P_3 values “avoid” the $P_{w,1}$ level, and are closer to the two $P_{w,1} \pm \Delta P_{w,1}$ levels. The weighted mean values of these two P_3 concentrations below and above $P_{w,1}$ are

$$P_{w,2} \pm \Delta P_{w,2} = 2.^d3954 \pm 0.^d0018 \quad (n = 9) \quad (62)$$

$$P_{w,3} \pm \Delta P_{w,3} = 2.^d4048 \pm 0.^d0036 \quad (n = 8). \quad (63)$$

These samples are hereafter called the $P_{w,2}$ -group and the $P_{w,3}$ -group. We highlight the seven cases where the conservative model is also the liberal model. Two of these belong to the $P_{w,2}$ -group (Fig. 9b: square around green filled circle) and five to the $P_{w,3}$ -group (Fig. 9b: diamond around green filled circle).

The amplitudes are shown in Fig. 9c. The two largest values in the years 2001 and 2007 nearly coincide with the M minima in Fig. 9a. There is some correlation between the M and the A_3 values (Fig. 9d: $n = 17$ green filled circles), because their linear correlation coefficient $r = 0.547$ reaches a significance of $p = 0.028$.

The $P_{w,2}$ -group and $P_{w,3}$ -group period samples are shown again in Figs. 9ef. The mean brightness M does not correlate with these periods. However, the conservative model has two periodicities only during brightness minima and maxima (Fig. 9e: red and blue filled circles in the years 1999, 2002 and 2008). The scatter of periods is larger with smaller amplitudes, but this may be due to lower signal to noise ratio (Fig. 9f).

11. Liberal model

The 1P-model is both the conservative and the liberal model in seven segments which were already highlighted in Figs. 9bef. The 2P-model breaks down in these seven segments and it can not be compared to the 1P-model with the criterion of Eq. 16. The 2P-model is the liberal model in the remaining fifteen segments. Comparison between the 2P-model and the 1P-model shows that in all these fifteen segments the former model is the better model with the criterion of Eq. 16 (Table 6: column Q_F). This means that the 2P-model is a statistically better model than the 1P-model for the light curves of FK Com.

The results for the liberal models are given in Tables 9-10 and Figs. 10-11. Note that we give the same M values in both Tables 7 and 9, as well as show these values in both Figs. 9ade and 10ade, because this makes it is easier to compare these seasonal M values to the periods and amplitudes of the conservative and the liberal models. These M changes of FK Com are shown again in Fig. 10a.

The liberal model periods are shown in Fig. 10b. In general, the periodicities detected in the overlapping segments between 1998 and 2004 agree so well that it is impossible to separate many symbols from each other. The minor differences are discussed in greater detail in our Appendix (Sects. A.1-A.21). Note that the green filled circle denoting the P_3 period of DATA_{1,12} in the year 2009 is shown only in the “be” panels, but it is absent from the “f” panel, because no A_3 amplitude estimate is available (Sect. A.20).

The weighted mean levels of the P_1 and P_2 periods are

$$P_{w,4} \pm \Delta P_{w,4} = 2.^d3896 \pm 0.^d0063 \quad (n = 15) \quad (64)$$

$$P_{w,5} \pm \Delta P_{w,5} = 2.^d4053 \pm 0.^d0077 \quad (n = 15). \quad (65)$$

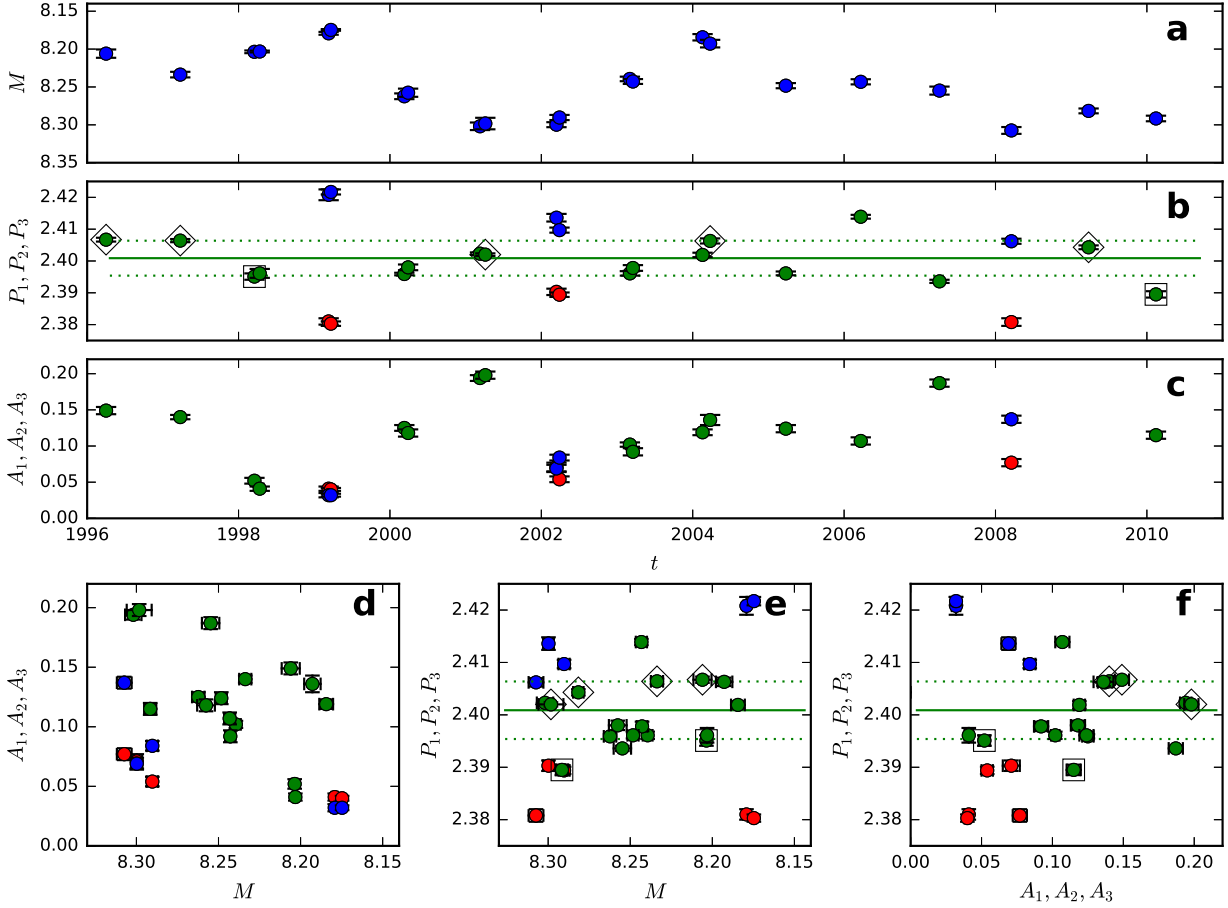


Fig. 9. Conservative model results of Table 7. (a) Mean M (blue filled circles). (b) Periods P_1 (red filled circles), P_2 (blue filled circles) and P_3 (green filled circles). The $P_{w,1}$ level (continuous line) and the $P_{w,1} \pm \Delta P_{w,1}$ levels (dotted green lines) of $P_{w,1}$ -group (Eq. 61). The seven cases when the 1P-model is also the liberal model are highlighted ($P_{w,2}$ -group: two squares around green filled circles, $P_{w,3}$ -group: five diamonds around green filled circles). (c) Amplitudes A_1 (red filled circles), A_2 (blue filled circles) and A_3 (green filled circles). (d) Amplitude versus mean: A_1 (red filled circles), A_2 (blue filled circles), A_3 (green filled circles) (e) Period versus mean: P_1 (red filled circles), P_2 (blue filled circles), P_3 (green filled circles) and green lines as in “b” (f) Period versus amplitude: P_1 (red filled circles), P_2 (blue filled circles), P_3 (green filled circles) and green lines as in “b”. Note that all symbols are filled circles, although some of them may appear to be squares, especially when the error bars are shown to both directions in correlation panels “def”.

These two period samples are hereafter referred to as the $P_{w,4}$ -group and the $P_{w,5}$ -group. These levels are shown with red and blue lines in Figs. 10bef. There are only two exceptions, where a blue filled circle is between the red dotted lines or a red filled circle is between the blue dotted lines. This happens in DATA_{2,5} and DATA_{1,3} in the year 2000. However, the amplitude of the weaker periodicity is so low in these segments that the “correct colour” for the symbol in these particular segments could also be the green colour, i.e. the two P_3 periods of the 1P-model are reasonable alternatives. The results for the 2P-model are nearly the same as those for the 1P-model in these two segments DATA_{2,5} and DATA_{1,3}. This is discussed in greater detail in our Appendix (Sects. A.6 and A.7). The red $P_{w,4}$ level is closer to the $P_3 = 2.^{\text{d}}3959 \pm 0.^{\text{d}}0004$ and $2.^{\text{d}}3980 \pm 0.^{\text{d}}0009$ periods of these two segments (Table 7).

The $P_{w,4}$ level of the P_1 periods is very close to the two highlighted P_3 values of $P_{w,2}$ -group (Figs. 9b and 10b: square around filled green circle). Although these two P_3 values were not used in computing the $P_{w,4}$ level, they fit

to this level surprisingly well. When we combine these two values with the $P_{w,4}$ -group, the weighted mean becomes

$$P_{w,6} \pm \Delta P_{w,6} = 2.^{\text{d}}3898 \pm 0.^{\text{d}}0061 \quad (n = 17). \quad (66)$$

This sample is hereafter called the $P_{w,6}$ -group.

The $P_{w,5}$ level coincides with the five highlighted P_3 values of $P_{w,3}$ -group (Figs. 9b and 10b: diamond around filled green circle). These five “independent” P_3 values are very close to the $P_{w,5}$ level which was computed from the fifteen P_2 periods. Combining these five values with the $P_{w,5}$ -group gives

$$P_{w,7} \pm \Delta P_{w,7} = 2.^{\text{d}}4050 \pm 0.^{\text{d}}0058 \quad (n = 20) \quad (67)$$

We will hereafter call this sample the $P_{w,7}$ -group.

Two P_1 values (circle around red filled circle) and three P_2 values (circle around blue filled circle) are also highlighted in Fig. 10b. These periods have the largest deviation from the red and the blue $P_{w,4}$ and $P_{w,5}$ levels. These five periodicities have two things in common. They have the largest errors and the lowest amplitudes in Table 9. In

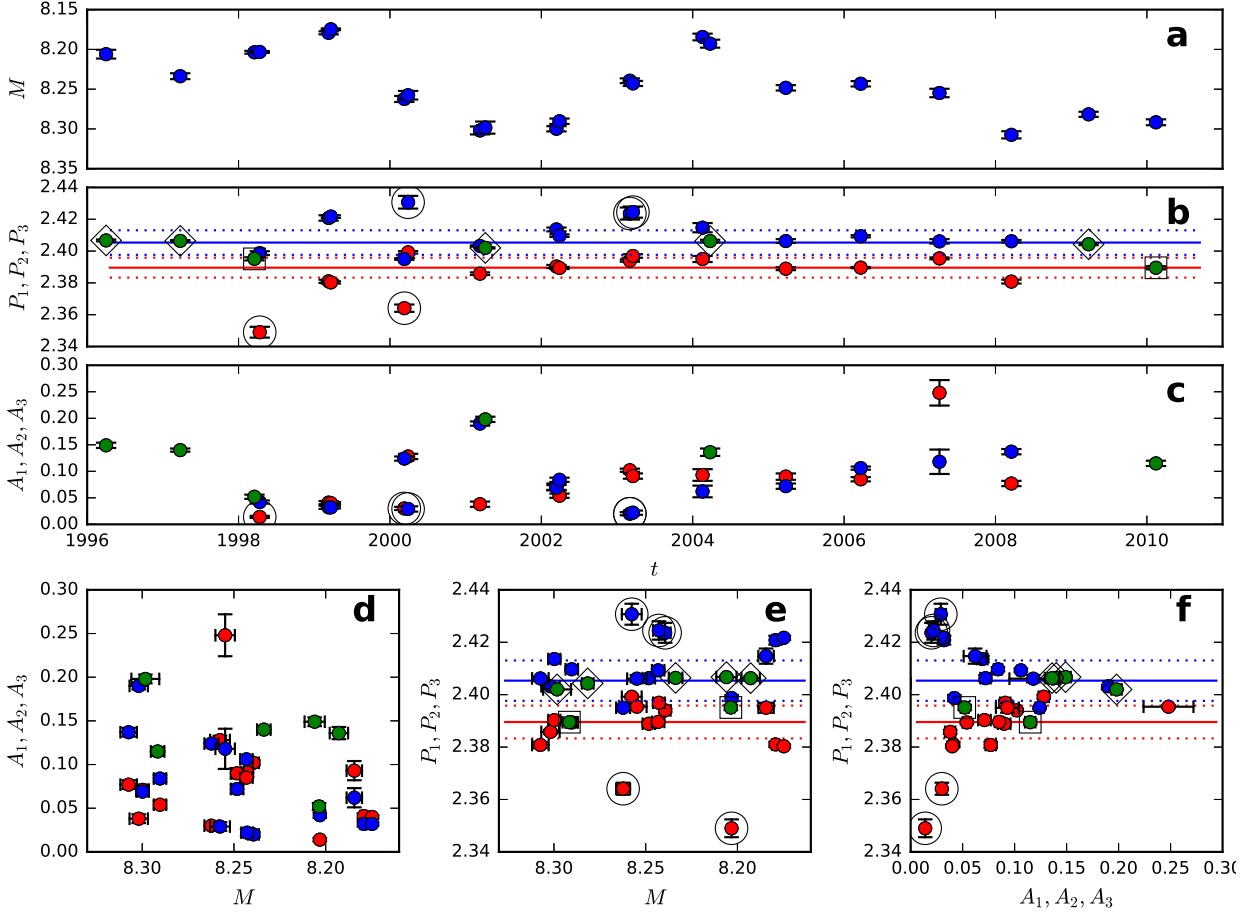


Fig. 10. Liberal model results of Table 9. (a) Mean M (b) Periods P_1 (red filled circles), P_2 (blue filled circles) and P_3 (green filled circles). The same seven cases as in Fig. 9b, where the 1P-model is the liberal model, are highlighted again ($P_{w,2}$ -group: two squares around green filled circles, $P_{w,3}$ -group: five diamonds around green filled circles). We also highlight two P_1 periodicities with a low amplitude A_1 (circles around red filled circles) and three P_2 periodicities with a low amplitude A_2 (circles around blue filled circles). The $P_{w,4}$ and $P_{w,4} \pm \Delta P_{w,4}$ levels are denoted with the continuous and dotted red lines (Eq. 64), and the $P_{w,5}$ and $P_{w,5} \pm \Delta P_{w,5}$ levels with the continuous and dotted blue lines (Eq. 65). (c) Amplitudes A_1 (red filled circles), A_2 (blue filled circles) and A_3 (green filled circles). The five lowest amplitudes already mentioned in “b” are highlighted. (d) Amplitude versus mean: A_1 (red filled circles), A_2 (blue filled circles), A_3 (green filled circles), (e) Period versus mean: P_1 (red filled circles), P_2 (blue filled circles), P_3 (green filled circles), highlighted values as in “b”, (f) Period versus amplitude: P_1 (red filled circles), P_2 (blue filled circles), P_3 (green filled circles), highlighted values as in “b”.

other words, they represent the weakest periodic signals of all liberal models. These five low A_1 and low A_2 amplitude values are also highlighted in Figs. 10cef.

The amplitudes A_1 , A_2 and A_3 are shown again in Fig. 10c. There is no correlation between these amplitudes and the mean M in Fig. 10d. The compact $P_{w,6}$ -group and $P_{w,7}$ -group distributions are also shown again in Figs. 10ef. These periodicities do not correlate with the mean or the amplitude. The scatter of periods increases at the lower amplitudes (Fig. 10f). The lower signal to noise ratio may be the reason for this (as also in Fig. 9f).

We conclude that the periods of the liberal model clearly belong to two separate groups. The first group is $P_{w,2} \approx P_{w,4} \approx P_{w,6}$ (Eqs. 62, 64 and 66), and the second one is $P_{w,3} \approx P_{w,5} \approx P_{w,7}$ (Eqs. 63, 65 and 67). For $\Delta T = 5212.^d8$ and $P = 2.^d4000$, the ± 1 rotation difference is $\delta_P = (P\Delta T)/(\Delta T \pm P) = \pm 0.^d0011$. Except for $P_{w,2}$, the differences of the three values *within* both groups are

smaller than $\delta_P/2$. The differences $P_{w,3} - P_{w,2} = 8.5\delta_P$, $P_{w,5} - P_{w,4} = 14.3\delta_P$ and $P_{w,7} - P_{w,6} = 13.8\delta_P$ *between* these two groups confirm that they are separated.

The largest samples in the above two separate groups are the $P_{w,6}$ -group and the $P_{w,7}$ -group. If the above two groups represent the long-term P_1 and P_2 periods of the 2P-model, the distributions of the light curve minimum epochs in the $P_{w,6}$ -group and the $P_{w,7}$ -group should be regular with these two periodicities. The primary and the secondary minimum epochs $t_i \pm \sigma_{t_i}$ of the $P_{w,6}$ -group and the $P_{w,7}$ -group are given Table 11. These samples are small ($n = 24$ and 20), and the time points t_i are evenly distributed one year after each other. The seven pairs of $n = 14$ time points t_i during the years 1998-2004 are nearly simultaneous, because they are determined from overlapping segments. This type of a regular time distribution introduces numerous spurious periods into our period analysis. Due to these obstacles, the search for the best period must rely on

Table 9. Liberal model mean, period and amplitude, otherwise as in Table 7.

TEL	SEG	YEAR	M	P_1	P_2	P_3	A_1	A_2	A_3
		[y]	[mag]	[d]	[d]	[d]	[mag]	[mag]	[mag]
2	1	1996.25	8.2060±0.0055	—	—	2.4067±0.0006	—	—	0.149±0.005
2	2	1997.23	8.2337±0.0037	—	—	2.4064±0.0005	—	—	0.140±0.003
2	3	1998.21	8.2036±0.0018	—	—	2.3951±0.0010	—	—	0.052±0.004
1	1	1998.28	8.2032±0.0012	2.3490±0.0034	2.3987±0.0012	—	0.014±0.002	0.042±0.003	—
2	4	1999.19	8.1792±0.0019	2.3810±0.0010	2.4208±0.0017	—	0.041±0.003	0.032±0.003	—
1	2	1999.22	8.1747±0.0011	2.3803±0.0007	2.4217±0.0008	—	0.040±0.002	0.032±0.002	—
2	5	2000.19	8.2623±0.0038	2.3641±0.0023	2.3950±0.0005	—	0.030±0.003	0.124±0.004	—
1	3	2000.24	8.2576±0.0054	2.3992±0.0008	2.4307±0.0040	—	0.128±0.005	0.029±0.005	—
2	6	2001.19	8.3019±0.0050	2.3858±0.0008	2.4032±0.0004	—	0.038±0.005	0.190±0.004	—
1	4	2001.26	8.2983±0.0076	—	—	2.4020±0.0004	—	—	0.198±0.005
2	7	2002.20	8.2998±0.0033	2.3903±0.0010	2.4136±0.0012	—	0.071±0.006	0.069±0.005	—
1	5	2002.24	8.2903±0.0034	2.3894±0.0007	2.4097±0.0008	—	0.054±0.004	0.084±0.004	—
1	6	2003.17	8.2394±0.0030	2.3940±0.0007	2.4236±0.0038	—	0.102±0.003	0.020±0.003	—
2	8	2003.21	8.2428±0.0032	2.3969±0.0011	2.4245±0.0035	—	0.091±0.005	0.022±0.004	—
1	7	2004.13	8.1844±0.0042	2.3950±0.0019	2.4147±0.0029	—	0.093±0.011	0.062±0.011	—
2	9	2004.23	8.1928±0.0050	—	—	2.4063±0.0008	—	—	0.136±0.007
1	8	2005.23	8.2483±0.0034	2.3889±0.0009	2.4063±0.0012	—	0.090±0.006	0.072±0.005	—
1	9	2006.22	8.2432±0.0034	2.3896±0.0004	2.4093±0.0007	—	0.085±0.004	0.106±0.003	—
1	10	2007.26	8.2548±0.0053	2.3954±0.0006	2.4061±0.0014	—	0.248±0.024	0.118±0.023	—
1	11	2008.21	8.3074±0.0045	2.3808±0.0012	2.4062±0.0008	—	0.077±0.005	0.137±0.005	—
1	12	2009.23	8.2816±0.0032	—	—	2.4043±0.0006	—	—	—
1	13	2010.12	8.2916±0.0037	—	—	2.3895±0.0010	—	—	0.115±0.005

Table 10. Liberal model minimum epochs, otherwise as in Table 8

TEL	SEG	YEAR	$t_{g1,min,1}$	$t_{g1,min,2}$	$t_{g2,min,1}$	$t_{g2,min,2}$	$t_{S,min,1}$	$t_{S,min,2}$
		[y]	[HJD - 2400000]					
2	1	1996.25	—	—	—	—	50086.056±0.041	—
2	2	1997.23	—	—	—	—	50412.955±0.032	—
2	3	1998.21	—	—	—	—	50779.712±0.100	—
1	1	1998.28	50852.542±0.269	50851.986±0.112	50850.927±0.049	—	—	—
2	4	1999.19	51145.492±0.055	51144.537±0.071	51146.438±0.112	—	—	—
1	2	1999.22	51155.039±0.038	—	51153.468±0.071	—	—	—
2	5	2000.19	51510.289±0.143	—	51508.111±0.023	—	—	—
1	3	2000.24	51534.339±0.038	—	51534.710±0.202	51536.347±0.159	—	—
2	6	2001.19	51875.004±0.043	51873.812±0.039	51874.421±0.021	—	—	—
1	4	2001.26	—	—	—	—	51884.040±0.030	—
2	7	2002.20	52242.585±0.049	52243.378±0.079	52243.870±0.104	—	—	—
1	5	2002.24	52248.229±0.059	52249.835±0.050	52248.758±0.049	—	—	—
1	6	2003.17	52614.830±0.027	—	52616.346±0.141	—	—	—
2	8	2003.21	52614.710±0.051	—	52613.595±0.249	—	—	—
1	7	2004.13	52980.176±0.076	—	52978.965±0.122	—	—	—
2	9	2004.23	—	—	—	—	52972.470±0.071	—
1	8	2005.23	53344.831±0.054	—	53343.706±0.064	—	—	—
1	9	2006.22	53722.936±0.017	53721.819±0.023	53723.122±0.035	—	—	—
1	10	2007.26	54076.823±0.038	—	54077.168±0.082	—	—	—
1	11	2008.21	54440.885±0.058	—	54442.056±0.054	—	—	—
1	12	2009.23	—	—	—	—	—	—
1	13	2010.12	—	—	—	—	55174.413±0.034	55173.029±0.051

the most accurate $t_i \pm \sigma_{t_i}$ values. We utilize all available information i.e. the weights $\sigma_{t_i}^{-2}$ of the time points t_i . Hence, the non-parametric weighted Kuiper method is applied to the $P_{w,6}$ -group and the $P_{w,7}$ -group minima of Table 11 (see Jetsu & Pelt 1996, their Eq. 28, hereafter the WK-method). The WK-method test statistic V_n utilizes the weights

$$w_i = \frac{n \sigma_{t_i}^{-2}}{\sum_{i=1}^n \sigma_{t_i}^{-2}}, \quad (68)$$

where σ_{t_i} is the error of t_i . When Jetsu (1996) applied this method to search for active longitudes in CABSs, the samples were at least three times larger than those in our Table 11. He noted that no significance estimated could be obtained for the periods detected with the WK-method, if the scatter of the weights w_i is large. For example, the sum of the three largest w_i weights in the $P_{w,6}$ -group is $5.7+3.1+2.3 = 11.1$ (Table 11). This sample contains only $n = 24$ time points t_i . When the WK-method searches for the best periods, the contribution of these three most accurate time

Table 11. Minima epochs of the $P_{w,6}$ -group and the $P_{w,7}$ -group. YEAR, TEL and SEG are as in Table 10. Columns 4. and 10. give the period P_1, P_2 or P_3 , and the minimum epoch $t_{\min,1}$ or $t_{\min,2}$ connected to this period (Pair). Columns 5 and 11 give the respective numerical values $t_i \pm \sigma_{t_i}$ from Table 10. The K-method weights w_i of $t_i \pm \sigma_{t_i}$ are given on columns 6 and 12 (Eq. 68). All results given in this table are shown in Figs. 11ab.

$P_{w,6}$ -group minima epochs						$P_{w,7}$ -group minima epochs					
1.	2.	3.	4.	5.	6.	7.	8.	9.	10.	11.	12.
YEAR	TEL	SEG	Pair	$t_i \pm \sigma_{t_i}$	w_i	YEAR	TEL	SEG	Pair	$t_i \pm \sigma_{t_i}$	w_i
1998.28	1	1	$P_1 : t_{\min,1}$	50852.542 ± 0.269	0.0	1998.28	1	1	$P_2 : t_{\min,1}$	50850.927 ± 0.049	0.8
1999.19	2	4	$P_1 : t_{\min,1}$	51145.492 ± 0.055	0.5	1999.19	2	4	$P_2 : t_{\min,1}$	51146.438 ± 0.112	0.2
1999.22	1	2	$P_1 : t_{\min,1}$	51155.039 ± 0.038	1.1	1999.22	1	2	$P_2 : t_{\min,1}$	51153.468 ± 0.071	0.4
2000.19	2	5	$P_1 : t_{\min,1}$	51510.289 ± 0.143	0.1	2000.19	2	5	$P_2 : t_{\min,1}$	51508.111 ± 0.023	3.8
2000.24	1	3	$P_1 : t_{\min,1}$	51534.339 ± 0.038	1.1	2000.24	1	3	$P_2 : t_{\min,1}$	51534.710 ± 0.202	0.0
2001.19	2	6	$P_1 : t_{\min,1}$	51875.004 ± 0.043	0.9	2001.19	2	6	$P_2 : t_{\min,1}$	51874.421 ± 0.021	4.5
2002.20	2	7	$P_1 : t_{\min,1}$	52242.585 ± 0.049	0.7	2002.20	2	7	$P_2 : t_{\min,1}$	52243.870 ± 0.104	0.2
2002.24	1	5	$P_1 : t_{\min,1}$	52248.229 ± 0.059	0.5	2002.24	1	5	$P_2 : t_{\min,1}$	52248.758 ± 0.049	0.8
2003.17	1	6	$P_1 : t_{\min,1}$	52614.830 ± 0.027	2.3	2003.17	1	6	$P_2 : t_{\min,1}$	52616.346 ± 0.141	0.1
2003.21	2	8	$P_1 : t_{\min,1}$	52614.710 ± 0.051	0.6	2003.21	2	8	$P_2 : t_{\min,1}$	52613.595 ± 0.249	0.0
2004.13	1	7	$P_1 : t_{\min,1}$	52980.176 ± 0.076	0.3	2004.13	1	7	$P_2 : t_{\min,1}$	52978.965 ± 0.122	0.1
2005.23	1	8	$P_1 : t_{\min,1}$	53344.831 ± 0.054	0.6	2005.23	1	8	$P_2 : t_{\min,1}$	53343.706 ± 0.064	0.5
2006.22	1	9	$P_1 : t_{\min,1}$	53722.936 ± 0.017	5.7	2006.22	1	9	$P_2 : t_{\min,1}$	53723.122 ± 0.035	1.6
2007.26	1	10	$P_1 : t_{\min,1}$	54076.823 ± 0.038	1.1	2007.26	1	10	$P_2 : t_{\min,1}$	54077.168 ± 0.082	0.3
2008.21	1	11	$P_1 : t_{\min,1}$	54440.885 ± 0.058	0.5	2008.21	1	11	$P_2 : t_{\min,1}$	54442.056 ± 0.054	0.7
1998.28	1	1	$P_1 : t_{\min,2}$	50851.986 ± 0.112	0.1	2000.24	1	3	$P_2 : t_{\min,2}$	51536.347 ± 0.159	0.1
1999.19	2	4	$P_1 : t_{\min,2}$	51144.537 ± 0.071	0.3	1996.25	2	1	$P_3 : t_{\min,1}$	50086.056 ± 0.041	1.2
2001.19	2	6	$P_1 : t_{\min,2}$	51873.812 ± 0.039	1.1	1997.23	2	2	$P_3 : t_{\min,1}$	50412.955 ± 0.032	2.0
2002.20	2	7	$P_1 : t_{\min,2}$	52243.378 ± 0.079	0.3	2001.26	1	4	$P_3 : t_{\min,1}$	51884.040 ± 0.030	2.2
2002.24	1	5	$P_1 : t_{\min,2}$	52249.835 ± 0.050	0.7	2004.23	2	9	$P_3 : t_{\min,1}$	52972.470 ± 0.071	0.4
2006.22	1	9	$P_1 : t_{\min,2}$	53721.819 ± 0.023	3.1						
1998.21	2	3	$P_3 : t_{\min,1}$	50779.712 ± 0.100	0.2						
2010.12	1	13	$P_3 : t_{\min,1}$	55174.413 ± 0.034	1.4						
2010.12	1	13	$P_3 : t_{\min,2}$	55173.029 ± 0.051	0.6						

points is about the same as that of the remaining other 21 less accurate time points, i.e. 11.1 against 12.9 = $n - 11.1$.

Since the samples are small and sparsely distributed at regular time intervals of one year, we use the WK-method only to find the V_n periodogram peaks that are closest to the $P_{w,6}$ and $P_{w,7}$ periods. These best periods are

$$P_{\text{WK},6} = 2.^{\text{d}}39313 \pm 0.^{\text{d}}00028 \quad (69)$$

$$P_{\text{WK},7} = 2.^{\text{d}}40762 \pm 0.^{\text{d}}00038. \quad (70)$$

The next step is to determine the zero epochs for the ephemerides of these two periodicities. We fix the most accurate t_i value at phase 0.25. This particular t_i value has the highest weight, i.e. $w_i = 5.7$ in the $P_{w,6}$ -group and $w_i = 4.5$ in the $P_{w,7}$ -group (Table 11). These two values are highlighted with a large square in Figs. 11ab. They gave the largest amount of information that was already used in solving the periods of Eqs. 69 and 70. The eight most accurate t_i values of both samples are highlighted with smaller squares. Of these eight points, we select only those that are closer than ± 0.15 in phase to the most accurate t_i value. Those points are highlighted with diamonds in Figs. 11ab. There are four and six such values in the $P_{w,6}$ -group and the $P_{w,7}$ -group, respectively (Figs. 11ab). For these particular values, we compute the level of their weighted mean phase and the error of this mean phase (Figs. 11ab: continuous and dotted horizontal red lines). These levels give us the ephemerides

$$\text{HJD } 2453722.876 (\pm 0.092) + 2.39313\text{E} \quad (71)$$

$$\text{HJD } 2451874.272 (\pm 0.163) + 2.40762\text{E}. \quad (72)$$

We add a continuous blue horizontal line to Figs. 11ab. It is half a period, or equivalently 0.5 in phase, above the red line of the ephemeris zero epoch. The majority of the time points $t_i \pm \sigma_{t_i}$ are close to these red and blue continuous lines of Figs. 11ab, especially the more accurate ones. This is an extremely good result, considering that the remaining values, $n - 4 = 20$ in the $P_{w,6}$ -group and $n - 6 = 14$ in the $P_{w,7}$ -group, were not used in solving the levels of these red and blue horizontal lines in Figs. 11ab.

The $P_{\text{WK},6}$ and $P_{\text{WK},7}$ periods of Eqs. 66 and 67 give $|k| = 0.0060 \pm 0.0002$ and $|\Delta\Omega| = 0.0158 \pm 0.0005$ (Eqs. 17 and 18). This $|\Delta\Omega|$ value of FK Com is between the two highest values in Table 4 which are those of EI Eri and V711 Tau.

12. MLC of FK Com

The MLCs of fourteen CABSSs were published by Jetsu et al. (2017, their Figs. 1-14). They studied the original data as a function of orbital phase ϕ_{orb} , and also combined those data into twenty ϕ_{orb} phase bins. The MLC changes were searched for by comparing the MLC of all data, the 1st part of data and the 2nd part of data.

The two ephemerides of Eq. 71 and 72 give the two MLC for the original y_i data of FK Com (Figs. 12a-1).

The first MLC of the original y_i data of FK Com is computed with the ephemeris of Eq. 71 (Figs. 12a-f). The minimum of the binned magnitudes for all y_i data is at $\phi_1 \approx 0.8$ (Fig. 12a). This MLC changes, because its shape, amplitude and minimum are slightly different in the 1st and the 2nd part of data (Figs. 12c-f).

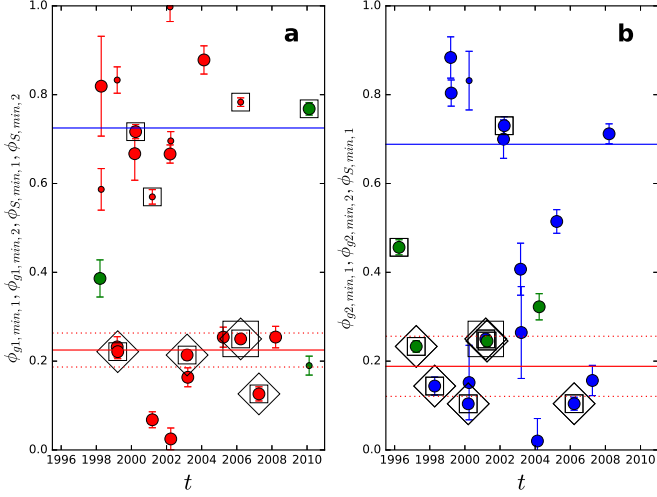


Fig. 11. Primary and secondary minima of $P_{w,6}$ -group and $P_{w,7}$ -group from Table 11. (a) $P_{w,6}$ -group symbols are large filled red circles (Pair= $P_1:t_{\min,1}$), small filled red circles (Pair= $P_1:t_{\min,2}$), large filled green circles (Pair= $P_3:t_{\min,1}$) and small filled green circle (Pair= $P_3:t_{\min,2}$). Continuous and dotted red lines denote the level and the accuracy of zero phase of the ephemeris of Eq. 71, while the continuous blue line denotes the 0.5 phase. The most accurate value is highlighted with a large square, and the eight most accurate values with smaller squares. The ephemeris zero epoch is determined from the four values highlighted with diamonds. (b) $P_{w,7}$ -group symbols are large filled blue circles (Pair= $P_2:t_{\min,1}$), small filled blue circles (Pair= $P_2:t_{\min,2}$), and large filled green circles (Pair= $P_3:t_{\min,1}$). Continuous and dotted red lines denote the zero phase of the ephemeris of Eq. 72, and the continuous blue line denotes the 0.5 phase. The highlighted values are selected as in “a”.

The ephemeris of Eq. 72 gives the second MLC for the original y_i data (Figs. 12g-l). This MLC for all original y_i data is regular and its minimum is close to $\phi_2 = 0.0$ (Fig. 12h). The shape, the amplitude and the minimum this MLC differ in the 1st and the 2nd part of data (Figs. 12j-l).

The MLC of the y_i data should be more regular, because the changes of the mean within the segments have been removed (Eq. 1). The error bars of the binned y_i magnitudes in Figs 13bdf are indeed smaller than those of the binned original y_i data in Figs.12bdf. All MLCs of the y_i data are also more regular than those of the original y_i data.

The first MLC for the y_i data of FK Com is shown in Figs. 13a-f, where the phases ϕ_1 are computed from the ephemeris of Eq. 71. The minimum of the binned magnitudes of all y_i data is at $\phi_1 \approx 0.7$ (Fig. 12b). For the 1st and the 2nd part of y_i data, these MLC changes in Figs. 13df resemble those of the MLC of y_i data in Figs. 12df.

With the ephemeris of Eq. 72, the results for the second MLC for the y_i data in Figs 13g-l resemble those obtained for the y_i data in Figs 12g-l. Note that the binned y_i data of the 2nd part show primary and secondary minima at $\phi_2 \approx 0.0$ and $\phi_2 \approx 0.5$ (Figs. 12l and 13l).

Although the amplitudes of all these MLC are low, between $0.^m02$ and $0.^m06$, their presence in the data indicates that the 2P-model is the correct model for the light curves of FK Com. These low MLC amplitudes are of the same order as those observed in some CABSs by Jetsu et al.

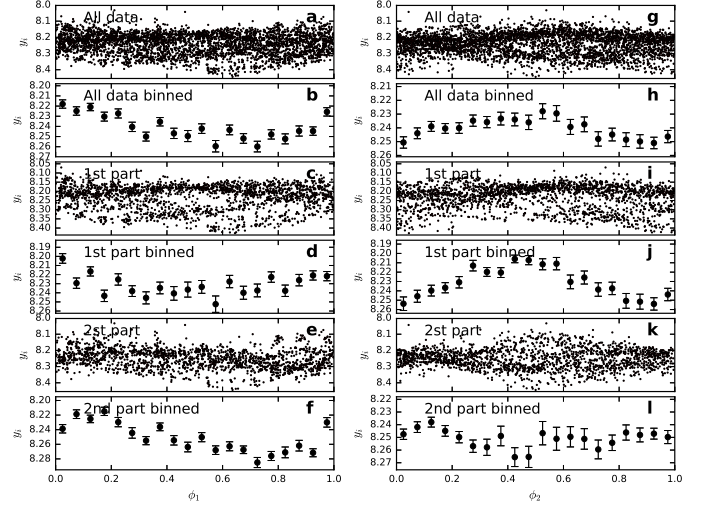


Fig. 12. MLC for original y_i data. (a) All data as function of phase ϕ_1 for computed from the ephemeris of Eq. 71. (b) All data, mean and error of mean in 20 bins. (cd) 1st part of data, otherwise as in “ab”, (ef) 2nd part of data, otherwise as in “ab” (g-l) Phases ϕ_2 computed from the ephemeris of Eq. 72, otherwise as in “a-f”.

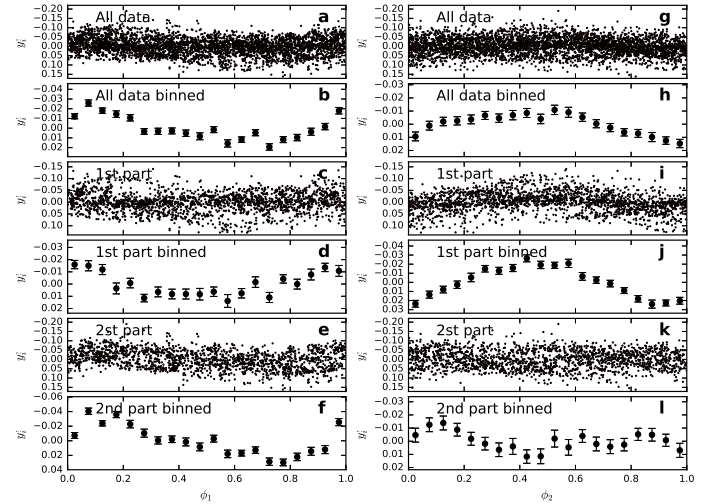


Fig. 13. MLC for y_i data. Otherwise as in Fig. 12

(2017, e.g. Fig. 3: EL Eri, Fig. 8: FG UMa). They noted that low amplitudes were *always* observed when the MLCs of these CABSs had two minima, but high amplitudes were observed *only* when their MLCs had one minimum. For FK Com, the bimodal phase distributions of the seasonal minima of the real $g_1(t)$ and $g_2(t)$ light curves also support this idea (Figs. 11ab). The changes of these MLCs between the 1st and 2nd part of data of FK Com are similar to those already observed in CABSs by Jetsu et al. (2017).

13. 2P-method analysis of all data

We also apply the 2P-method to all y_i data. The results are shown in Figs. 14-16. Before this analysis, a second order polynomial fit is first used to remove the changes of the mean of the original data within the segments (Eq. 1). Then the data of all segments are combined. This eliminates

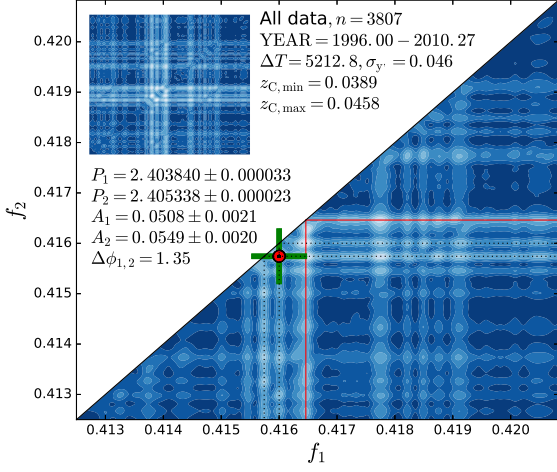


Fig. 14. All data, otherwise as in Fig. 6.

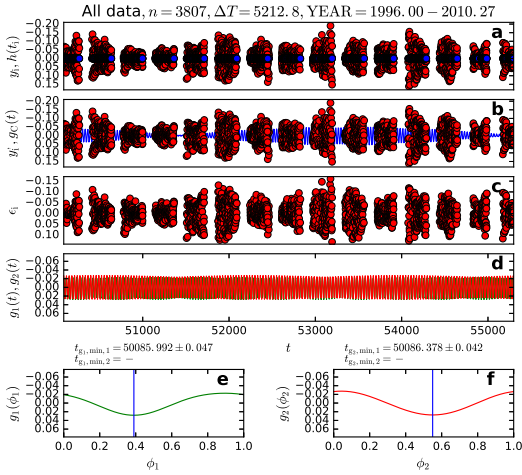


Fig. 15. All data, otherwise as in Fig. 7.

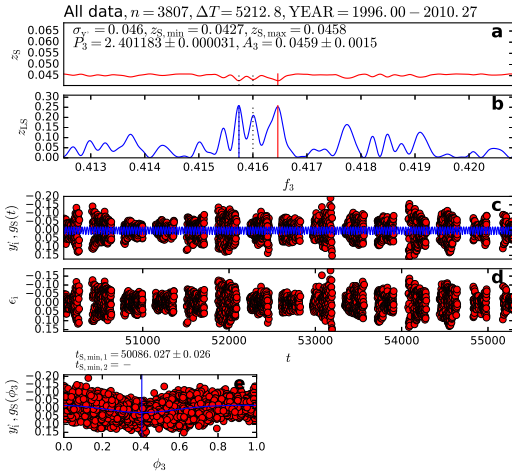


Fig. 16. All data, otherwise as in Fig. 8.

the mean level changes both within and between segments. Hence, our analysed “original” all y_i data is the y_i^g data within individual segments.

The computation of the 2P-method results requires a lot of computing time. Hence, our tested period interval is only $f_{\min} = (1-a)f_{\text{mid}}$ and $f_{\max} = (1+a)f_{\text{mid}}$, where $P_{\text{mid}} = 2.4$

and $a = 0.01$ (Eq. 34). The $z_C(f_1, f_2)$ periodogram of all y_i^g data resembles a patchwork quilt (Fig. 14). There are numerous horizontal and vertical white stripes, and even whiter patches in the crossings of these stripes. The minimum level $z_{C,\min} = 0.^m0389$ is about fifty times larger than the $0.^m008$ accuracy of the data. This level is comparable to the standard deviation $\sigma_{y_i} = 0.^m046$ of the data. The stronger $P_2 = 2.^d405338 \pm 0.^d000023$ periodicity is close, but not exactly equal, to $P_{\text{WK},7} = 2.^d40762 \pm 0.^d00038$ (Eq. 70). The weaker $P_1 = 2.^d403840 \pm 0.^d000033$ periodicity is certainly not equal to $P_{\text{WK},6} = 2.^d39313 \pm 0.^d00028$ (Eq. 69).

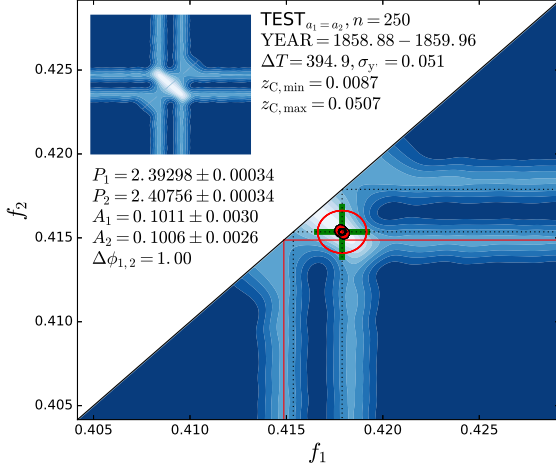
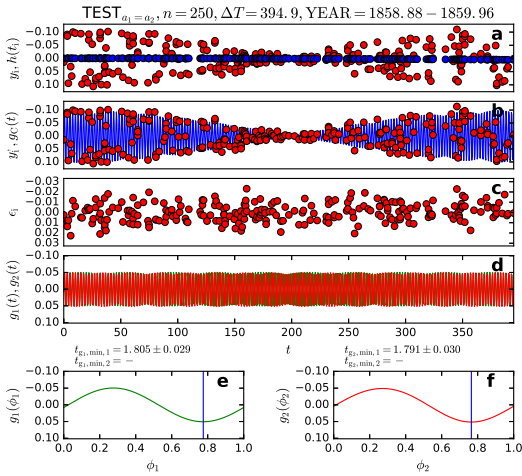
The second order polynomial fit to the original data in Fig. 15a is a horizontal line, because the changes of the mean within the segments were already removed before combining the y_i^g data of all segments. The $g_C(t)$ model can not follow the data (Fig. 15b), because the residuals ϵ_i are of the same order as the y_i^g data (Fig. 15c). The amplitudes of the $g_1(t)$ and g_2 light curves $A_1 = 0.^m051$ and $A_2 = 0.^m055$ are nearly the same (Figs. 15def). Both curves have only one minimum.

The results for the simple $g_S(t)$ model of the 1P-method are shown in Figs. 16a-e. The $z_{S,\min} = 0.^m0427$ value is even larger than the $z_{C,\min} = 0.^m0389$ value of the complex 2P-model. The 1P-method, the LS-method and the 2P-method detect different best periods (Fig. 16b: vertical continuous red, continuous blue and dotted black lines). The amplitude of the $g_S(t)$ curve is only $A_3 = 0.^m046$. This model fails to reproduce the data and the residuals are of the same order as the data itself (Figs. 16cd). The $g_S(t)$ curve has only one minimum (Fig. 16e).

The amplitudes of the $g_C(t)$ and $g_S(t)$ models are so low that the plots for the modelled y_i^g data (Figs. 15b and Figs. 16b) are nearly identical to the plots for the residuals ϵ_i (Figs. 15c and Figs. 16c). Does all this then mean that the 2P-method does not work, because the ephemerides of Eqs. 71 and 72 do not explain all data? The answer is “No”. The $z_C(f_1, f_2)$ periodogram of all data displays exactly the results that we should get. The impact of each individual segment is illustrated in this periodogram of all data. It is not these results for all data, but the results for the temporally overlapping data segments from two different telescopes, that can be used to check the performance of the 2P-method. The results for these seven pairs of temporally overlapping segments from two different telescopes agree well, and this confirms that the 2P-method works (Appendix: Sects. A.2-A.15). The results for *individual* segments show that the real light curves $g_1(t)$ and $g_2(t)$ are constantly changing. These $g_1(t)$ and $g_2(t)$ changes are the reason for the patchwork quilt $z_C(f_1, f_2)$ periodogram of Fig. 14. This figure illustrates how complex the combined long-term changes of the real light curves $g_1(t)$ and $g_2(t)$ of FK Com can be. Even the two-dimensional period finding 2P-method can not model to this complexity for all data.

14. 2P-method analysis of simulated TEST $_{a_1=a_2}$ and TEST $_{a_1 < a_2}$ data

The results for the temporally overlapping seven pairs of segments from two different telescopes already confirm that the 2P-method works (Sects. A.2-A.15). However, we want to apply this method also to the simulated data of Sects. 7.3.1 and 7.3.2. Our aim is to show that the 2P-method de-

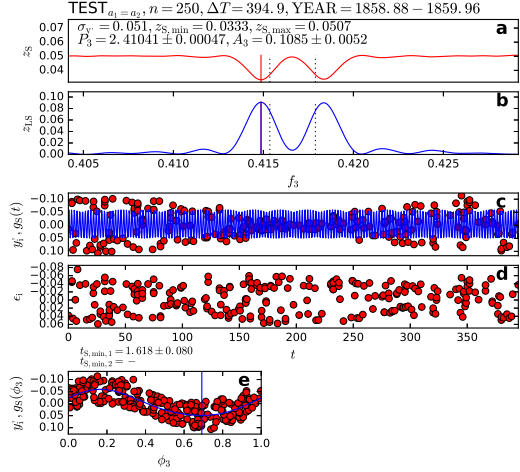

 Fig. 17. $\text{TEST}_{a_1=a_2}$, otherwise as in Fig. 6.

 Fig. 18. $\text{TEST}_{a_1=a_2}$, otherwise as in Fig. 7.

tects the simulated real light curves $g_1(t) = s_1(t)$ and $g_2(t) = s_2(t)$ of Eqs. 30 and 31, as well as correctly retrieves all other parameters of the $g_C(t) = s(t) = s_1(t) + s_2(t)$ model. Note that the years in our next six Figs. 17-22 are arbitrary, because the simulated $t = 0$ equals HJD 2 400 000.

14.1. Results for simulated $\text{TEST}_{a_1=a_2}$ data

The $z_C(f_1, f_2)$ periodogram of $\text{TEST}_{a_1=a_2}$ data displays two equally light blue crosses against a dark blue background: the signature of two equally strong signals (Fig. 17). The results agree for the detected periods $P_1 = 2.^{\text{d}}39298 \pm 0.^{\text{d}}00034 \approx 2.^{\text{d}}39313$ of Eq. 71 and $P_2 = 2.^{\text{d}}40756 \pm 0.^{\text{d}}00034 \approx 2.^{\text{d}}40762$ of Eq. 72, as well as those for the amplitudes $A_1 = 0.^{\text{m}}1011 \pm 0.^{\text{m}}0030 \approx 2a_1 = 0.^{\text{m}}10$ and $A_2 = 0.^{\text{m}}1006 \pm 0.^{\text{m}}0026 \approx 2a_2 = 0.^{\text{m}}10$. The residuals $z_{C,\min} = 0.^{\text{m}}0087$ are nearly equal to the standard deviation $0.^{\text{m}}008$ of the Gaussian residuals added to the simulated model $s(t)$ (Eq. 33). This is a perfect period analysis result.

The original data and the second order polynomial fit to these data are shown in Fig. 18a. The $g_C(t)$ model fits the y_i data, and the level and scatter of the residuals are stable (Fig. 18bc). The $g_1(t)$ and $g_2(t)$ curves in Figs. 18def are the


 Fig. 19. $\text{TEST}_{a_1=a_2}$, otherwise as in Fig. 8.

same as the $\text{TEST}_{a_1=a_2}$ input curves. We noted in the end of Sect. 7.3 that the simulated light curves had the zero point time shifts of $P_1/2$ and $P_2/2$ in Eqs. 30 and 31. This means that the $s_1(t)$ and $s_2(t)$ maxima, or equivalently the light curve minima, should be at $3P_1/4 = 1.^{\text{d}}795$ and $3P_2/4 = 1.^{\text{d}}806$, respectively. This agrees quite well with the results $t_{g1,\text{tmin},1} = 1.^{\text{d}}822 \pm 0.^{\text{d}}030$ and $t_{g2,\text{tmin},1} = 1.^{\text{d}}753 \pm 0.^{\text{d}}030$.

The 1P-method results are shown in Figs. 19a-e. The relation of Eq. 39 predicts that the one-dimensional period finding methods should detect the period $P_3 = (P_1 + P_2)/2 = 2.^{\text{d}}40037$. We have checked that the 1P-method and the LS-method detect this period in the first and second *part* of the data. However, these two methods detect a completely different period, $P_3 = 2.^{\text{d}}41041 \pm 0.^{\text{d}}00047$, from *all* data. The reason for this failure is the abrupt $\Delta\phi_b = 0.5$ phase shift (Eq. 48) that occurs in the middle of $\text{TEST}_{a_1=a_2}$ data. The two best periods detected with both of these one-dimensional period finding methods are quite close, but not exactly equal, to P_1 and P_2 (Figs. 19a-b: vertical continuous red, continuous blue and dotted black lines). These methods can detect signs of the P_1 and P_2 periods, because the difference between $1/P_1$ and $1/P_2$ is $f_0 = 1/\Delta T$ during $\Delta T = P_{1,\text{ap}}$. Hence, these two equally strong peaks in Fig. 19b can be separated in the Fourier transform domain (see Loumos & Deeming 1978, as well as the discussion in our Sect. 9.4). The 1P-model clearly fails to adapt to the amplitude changes and the abrupt $\Delta\phi_b = 0.5$ phase shift of these data (Figs. 19cde).

14.2. Results for simulated $\text{TEST}_{a_1 < a_2}$ data

The $\text{TEST}_{a_1 < a_2}$ periodogram $z_C(f_1, f_2)$ displays a nearly white cross and a light blue cross against a dark blue background (Fig. 20). These two crosses are signatures of the stronger and the weaker signal. The periods $P_1 = 2.^{\text{d}}39251 \pm 0.^{\text{d}}00063 \approx 2.^{\text{d}}39313$ of Eq. 71 and $P_2 = 2.^{\text{d}}40804 \pm 0.^{\text{d}}00034 \approx 2.^{\text{d}}40762$ of Eq. 72, as well as the amplitudes $A_1 = 0.^{\text{m}}0467 \pm 0.^{\text{m}}0032 \approx 2a_1 = 0.^{\text{m}}05$ and $A_2 = 0.^{\text{m}}0948 \pm 0.^{\text{m}}0028 \approx 2a_2 = 0.^{\text{m}}10$ are close to those of the simulated model. The standard deviation $0.^{\text{m}}008$ of the Gaussian residuals added to the simulated model $s(t)$ (Eq. 33) is close, but not exactly equal, to $z_{C,\min} = 0.^{\text{m}}0101$.

The next figure Fig. 21a shows the original data and the second order polynomial fit to these data. Due to the

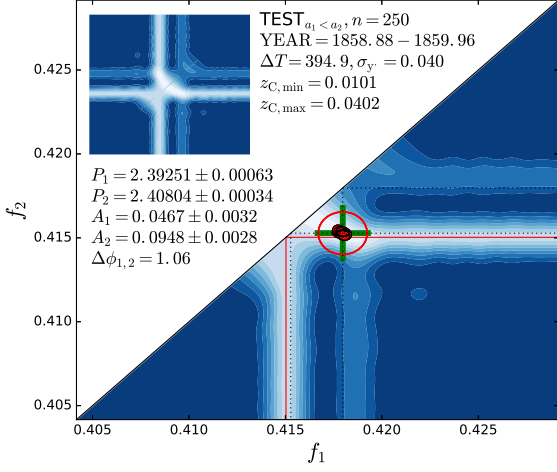


Fig. 20. $\text{TEST}_{a_1 < a_2}$, otherwise as in Fig. 6.

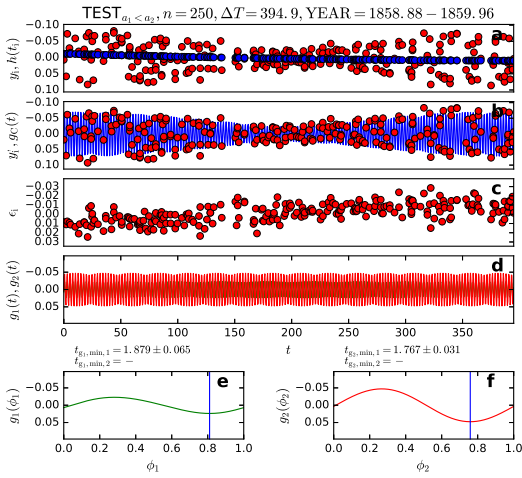


Fig. 21. $\text{TEST}_{a_1 < a_2}$, otherwise as in Fig. 7.

irregular time distribution of this particular simulated data sample, the polynomial fit deviates slightly from the expected zero level in the beginning of the segment. This deviation shows in the $g_C(t)$ model fit to the y_i data, and especially as a minor trend in the level of the residuals ϵ_i (Fig. 21bc). The $g_1(t)$ and $g_2(t)$ curves shown in Figs. 21def should have minima at $3P_1/4 = 1.^d795$ and $3P_2/4 = 1.^d806$. Our results, $t_{g1,tmin,1} = 1.^d879 \pm 0.^d065$ and $t_{g2,tmin,1} = 1.^d767 \pm 0.^d031$, are close to these input values. The above mentioned minor deviation of the second order polynomial fit does slightly mislead our 2P-model. Due to this deviation, the $z_{C,min} = 0.^m0101$ level does not reach the $0.^m008$ level of simulated residuals (Eq. 33). We have analysed numerous other $\text{TEST}_{a_1 < a_2}$ simulations, where the polynomial fit to the original data does not cause this type of deviation of the residuals from the zero level. In those cases, all 2P-model analysis results are even closer to the input values of the simulated model. However, we chose to show this particular simulation, because our aim was to verify that even a poor second order polynomial fit to the original data does not seriously mislead the 2P-model analysis. We encounter similar deviations also in the 2P-method analysis of real data (e.g. Figs. A.5c of A.14c).

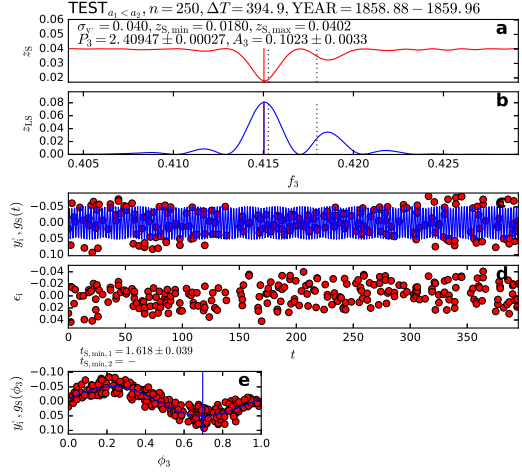


Fig. 22. $\text{TEST}_{a_1 < a_2}$, otherwise as in Fig. 8.

The 1P-method analysis results are shown in Figs. 22a-e. The relations of Eq. 45 and 46 predict that the one-dimensional period finding methods should detect the stronger period $P_2 = 2.^d40762$. The best period detected with both of the 1P-method and the LS-method is close, but not exactly equal, to P_2 (Figs. 22a-b: vertical continuous red, continuous blue and dotted black lines). Both of these two one-dimensional period finding methods can also detect some signs of the weaker P_1 periodicity. The 1P-model can not reproduce the amplitude changes of these data (Figs. 22cde).

In conclusion, we confirm that the 2P-method correctly detects the periodicities of simulated $\text{TEST}_{a_1 = a_2}$ and $\text{TEST}_{a_1 < a_2}$ data, as well as the amplitudes and the minimum epochs. Finally, we have also checked that the 2P-method detects numerous different kinds of simulated $g_1(t)$ and $g_2(t)$ combinations, and not only the combinations of $\text{TEST}_{a_1 = a_2}$ and $\text{TEST}_{a_1 < a_2}$ cases that were discussed above.

15. Connection between CPS-method results and 2P-method results

Here, we discuss how the 2P-model ephemerides of Eq. 71 and 72 are connected to the CPS-method analysis results reported earlier by Hackman et al. (2013). Their results for the periods, the amplitudes and the minimum epochs are shown in Figs. 23b-e.

The phase difference between the minima of the $g_1(t)$ and $g_2(t)$ curves is shown in Fig. 23a (continuous zig-zag line). It is computed from the t_1 zero epoch and the P_1 period of Eq. 71, and the t_2 zero epoch and the P_2 period of Eq. 72. This phase difference is

$$\Delta\phi_{P_1, P_2} = (2\pi)^{-1} \arccos [\cos \theta_1 \cos \theta_2 + \sin \theta_1 \sin \theta_2], \quad (73)$$

where the phase angles are $\theta_1 = 2\pi(t - t_1)/P_1$ and $\theta_2 = 2\pi(t - t_2)/P_2$. The $\Delta\phi_{P_1, P_2} = 0.5$ epochs are denoted with vertical dotted lines in all Figs. 23a-e. The ephemerides of Eqs. 71 and 72 predict that these are the most probable epochs for the lowest observed amplitudes $A_3 = 2a_{b,min}$ of the sum of curve $g(t) = g_1(t) + g_2(t)$ (Eq. 43), and the abrupt $\Delta\phi_b$ phase shifts (Eq. 48). The time interval between two consecutive vertical lines is one lap cycle period $P_{lap} = 398^d$. The data contain fourteen such cycles C1-C14. It is essential to understand that our three figures for

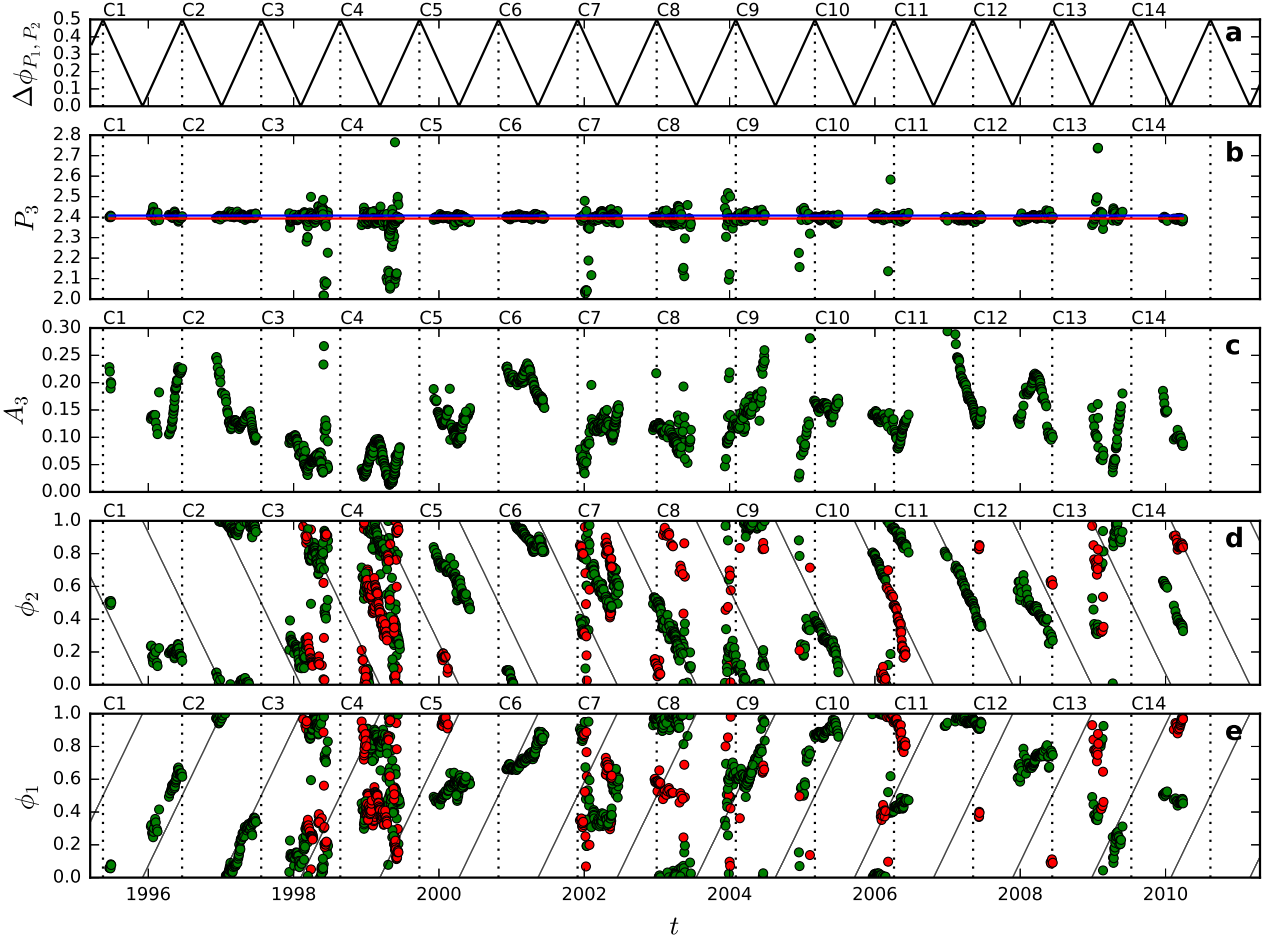


Fig. 23. CPS-model results of Table 3. (a) Phase difference $\Delta\phi_{P_1, P_2}$ of Eq. 73 (continuous zig-zag line) and epochs of $\Delta\phi_{P_1, P_2} = 0.5$ (vertical dotted lines). These vertical dotted lines are also shown in all panels below. The lap cycles P_{lap} from one vertical line to another are numbered from C1 to C14. (b) CPS-method periods (Table 3: P_3) of Table 3. Red and blue continuous lines denote the $P_{WK,6}$ and $P_{WK,7}$ levels (Eqs. 69 and 70). (c) CPS-method amplitudes (Table 3: A_3). (d) CPS-method primary and secondary minimum epochs (Table 3: $t_{\min,1}$ and $t_{\min,2}$). The phases ϕ_2 are computed from the ephemeris of Eq. 72. Tilted lines denote $\phi_1 = 0$ of Eq. 71. (e) Same as in “d”, except that the phases ϕ_1 are computed from the ephemeris of Eq. 71 and tilted lines denote $\phi_2 = 0$ of Eq. 72.

the periods (Figs. 2b, 3b, 23b), the amplitudes (Figs. 2c, 3c, 23c) and the minima (Figs. 2d, 3d, 23de) illustrate the same phenomena in the simulated and the real data. The main difference is that these figures show fourteen P_{lap} cycles C1-C14 of real data of FK Com, but only one P_{lap} cycle of simulated data. The changes of periods, amplitudes and minimum phases during each *individual* C1-C14 cycle are analogous to the simulated changes of these parameters in Figs. 2b-d and 3b-d.

First, we describe the general regularities in Fig. 23 for *all* cycles, and then those for the *individual* cycles. Finally, we describe something that will be referred to as the “corridor effect”.

15.1. General regularities

The results for the P_3 periods are shown in Fig. 23b, where the levels of the $P_1 = P_{WK,6}$ and $P_2 = P_{WK,7}$ periods (Eqs. 71 and 72) are denoted with horizontal continuous red and blue lines. Hackman et al. (2013) computed their weighted mean, $P_{w,CPS} \pm \Delta P_{w,CPS} = 2.^d398 \pm 0.^d012$ (Eqs.

26 and 27) from $n = 136$ independent P_3 estimates. Using all $n = 1450$ estimates from Table 3 gives the same result $P_{w,CPS} \pm \Delta P_{w,CPS} = 2.^d398 \pm 0.^d029$, except for a larger error $\Delta P_{w,CPS}$. Of the P_3 periods deviating more than $\pm 0.^d2$ from $2.^d4$, there are $n = 35$ values below $2.^d2$, but only $n = 3$ values above $2.^d6$. (Fig. 23b). There is a simple reason for this. When the analysed datasets cover about one month and a period close to two days is used in the least squares fit, all data concentrate on two narrow phase intervals, and the algorithm can utilize the remaining empty phase intervals for obtaining a model with smaller residuals. When we remove the above mentioned 38 deviating P_3 values, the remaining $n = 1412$ values give $P_{w,CPS} \pm \Delta P_{w,CPS} = 2.^d398 \pm 0.^d010$. This $P_{w,CPS}$ value differs $0.^d003 \pm 0.^d010$ from the mean $(P_1 + P_2)/2 = (P_{w,6} + P_{w,7})/2 = 2.^d40028 \pm 0.^d00025$ of our ephemeris periods in Eqs. 71 and 72. Our 2P-method analysis shows that either one of the $P_1 = P_{WK,6}$ and $P_2 = P_{WK,7}$ periodicities can dominate in different segments. Thus, our Eqs. 39, 45 and 46 predict that the relation $P_{WK,6} = P_1 < P_{w,CPS} < P_2 = P_{WK,7}$ should be fulfilled, and it is.

Except for a few outliers, the A_3 changes are continuous (Fig. 23c). The scatter of the P_3 periods is larger for smaller amplitudes, and close to the vertical dotted lines denoting the $\Delta\phi_{P_1, P_2} = 0.5$ epochs. The light curve primary and secondary minimum phases are computed from the ephemeris of Eq. 72 (Fig. 23d). The scatter of these phases is larger for smaller amplitudes. The amplitudes are high in cycles C1, C2, C5, C6, C11 and C2, as well as in the beginning of cycles C9 and C10. The migration of the minima is regular during these high amplitude time intervals. Low amplitudes are seen in cycles C3, C4, C7, C8, C9, C13 and C14, and in the end of cycle C10. The majority of secondary minima are observed during these low amplitude time intervals, as well as the abrupt $\Delta\phi_b$ shifts predicted by Eq. 48. Since we know that these shifts depend on the amplitude ratio $a_1/a_2 = A_1/A_2$, there is no need to unambiguously identify all “perfect” $\Delta\phi_b = 0.5$ flip-flop events, like the ones on the C6–C7 and C10–C11 cycle borders (Fig. 23d: dotted vertical lines). These shifts coincide with low observed A_3 amplitudes, but they *never* occur in high A_3 amplitude light curves, as predicted by Eq. 48.

The JHL-argument predicts many of the above general results in Figs. 23b–e. Similar general regularities were also discovered in the photometry of fourteen CABSs by Jetsu et al. (2017, Figs. 15–27). However, all details in Figs. 23b–e can not be explained with the ephemerides of Eqs. 71 and 72. This is no surprise, because the 2P-model residuals for all data are so large in Figs. 14–15. In other words, the real $g_1(t)$ and $g_2(t)$ light curves are not the same for all data. These real light curves change *between* and *within* segments. Several details in Figs. 23b–e can be connected to these real light curves of *individual* lap cycles. We will now discuss some of those details in the temporal order.

15.2. Individual lap period cycles

DATA_{2,1} and DATA_{2,2} overlap C1 and C2 cycles. The 1P-model is the liberal model, where only one high amplitude $P_3 = 2.^d4067$ signal dominates (Figs. 8 and A.3). There is no scatter in the P_3 periods and the A_3 amplitudes are high (Figs. 23bc). The primary minima stay close to $\phi_2 = 0.0$, and there are no secondary minima (Fig. 23d).

The 1P-model is also the liberal model for DATA_{2,3} and DATA_{1,3} during C3 cycle. The P_3 periods disperse in the end this cycle and the amplitudes A_3 decrease close to zero (Figs. 23bc). The primary minima are at both sides of $\phi_2 = 0.0$, but now there are also secondary minima (Fig. 23d). There is some switching between these primary and secondary minima in the end of these segments.

In C4 cycle, the 2P-model is the liberal model for DATA_{2,4} and DATA_{1,2}. The P_3 periods scatter in the end of these segments, but the variation of the A_3 amplitudes is regular (Figs. 23bc). The periods $P_1 \approx 2.^d3810$ and $P_2 \approx 2.^d4208$ give a lap cycle $P_{\text{lap}} = 145^d$. The amplitudes of these two signals are nearly equal, and this explains the messy $\Delta\phi_b$ shifts during cycle C4 (Fig. 23d). The two minima and the one maximum of the A_3 observed amplitude curve can also be used to estimate indirectly the length of the P_{lap} cycle (Fig. 23c). These two minima and the one maximum, $A_{3,\text{min}} \approx 0.^m01$ and $A_{3,\text{max}} \approx 0.^m09$, of this nearly regular amplitude curve can be used to estimate indirectly the A_1 and A_2 amplitudes. The relations of Eqs. 50 and 51 give $A_1 \approx 0.^m040$ and $A_2 \approx 0.^m050$. Note that these relations do not tell anything about P_1 and P_2 , and

about the order $A_1 < A_2$ or $A_1 > A_2$. The liberal models of these segments have approximately the above mentioned amplitudes in Table 9: $A_1 = 0.^m041$ and $A_2 = 0.^m032$ for DATA_{2,4}, and $A_1 = 0.^m040$ and $A_2 = 0.^m032$ for DATA_{1,2}.

In C5 cycle, the 2P-model is the liberal model of DATA_{2,5} and DATA_{1,3}. However, the strong high amplitude $P_2 = 2.^d3950 \approx P_1 = 2.^d3992$ periodicity dominates the observed light curve (Sects. A.6 and A.7). The P_3 periods are stable and the A_3 amplitude changes are regular (Figs. 23bc). Hence, the migration of the minima is regular, although there are a few secondary minima in the beginning of this C5 cycle (Fig. 23d).

The stronger P_2 periodicity of the 2P-model during C6 cycle is the same in DATA_{2,6} and DATA_{1,4} (Sects. A.8 and A.9: last paragraphs). Due to this, the P_3 periods show no scatter and the A_3 amplitude changes are regular (Figs. 23bc). The migration of the minima is regular, because the high amplitude $g_2(t)$ signal dominates the observed $g(t)$ light curve (Fig. 23d).

The P_3 periods scatter and the A_3 amplitudes approach zero in the beginning of C7 cycle (Figs. 23bc). A perfect flip-flop takes place at C6–C7 cycle border in DATA_{2,7} and DATA_{1,5} (Fig. 23d: vertical dotted line). The variation of the original data is small in the beginning of both segments, but then it begins to increase (Figs. A.29a and A.32a). The short 248^d lap cycle of the periods $P_1 = 2.^d3903$ and $P_2 = 2.^d4136$ (Fig. A.28: DATA_{2,7}) explains the regular migration of the minima during seven months (Fig. 23d).

There is some scatter in the P_3 periods and the A_3 amplitudes of C8 cycle (Figs. 23bc). However, the migration of the primary minima is regular, because the stronger period $P_1 = 2.^d3940$ (Fig. A.34) dominates the observed $g(t)$ light curves of DATA_{1,6} and DATA_{2,8}. There are a few secondary minima (Fig. 23d).

There are minor differences in the results for the temporally partly overlapping DATA_{1,7} and DATA_{2,9} during cycles C8–C9 (see Sect. A.15: last paragraph). In the beginning, there is some scatter in the P_3 and A_3 values (Figs. 23bc). The scatter of minima is large in the end of C8 cycle when the amplitudes A_3 are small. The results for DATA_{1,7} indicate the presence of two periodicities during the first months (Fig. A.40). The scatter of minima vanishes in the middle of C9 cycle, when the high amplitude $P_3 = 2.^d4063$ periodicity begins to dominate during the last months of DATA_{2,9} (Fig. A.45).

The DATA_{1,8} observations cover the end of C9 cycle and the beginning of C10 cycle. The A_3 amplitude of the observed light curve is first low, but then it increases (Fig. A.47a). The scatter in P_3 periods and A_3 amplitudes, as well as the irregularities in the minima migration, vanish when the amplitudes increase (Figs. 23b–d).

The border between C10 and C11 cycles shows another perfect flip-flop. This phenomenon is also seen in the DATA_{1,9} observations, as the amplitude first decreases close to zero and then increases again (Fig. A.50a). The “expected” scatter of some P_3 values is also observed during this event (Fig. 23b). This scatter of P_3 periods coincides with the A_3 amplitude minimum (Fig. 23bc), as expected in a flip-flop. The migration of the primary and the secondary minima, as well as the switch between these minima, are regular (Fig. 23d).

The $P_1 = 2.^d3954$ periodicity in DATA_{1,10} (Fig. A.52) enhances the largest A_3 amplitudes in Fig. 23c. Hence, there is no scatter in the P_3 periods and the A_3 amplitudes, and

the migration of minima is regular during the last half of C11 cycle (Figs. 23b-d).

The level of the P_3 periods is stable and the A_3 changes are regular during the last half of C12 cycle (Figs. 23bc). The lap cycle $P_{\text{lap}} = 226^{\text{d}}$ of the periods $P_1 = 2.^{\text{d}}3808$ and $P_2 = 2.^{\text{d}}4062$ is nearly as long as the time span $\Delta T = 204^{\text{d}}$ of DATA_{1,11} (Fig. A.55). The A_3 amplitude curve nearly completes this lap cycle, while the stronger P_2 periodicity dominates the migration of the minima (Figs. 23cd).

The enigmatic light curve changes during DATA_{1,12} are discussed in detail in Sect. A.20. There is scatter in the P_3 periods during C13 cycle (Fig. 23b). The A_3 amplitudes first decrease close to zero and then begin to increase again (Fig. 23c), as also seen in Fig. A.59a. The scatter of minima is large in the middle of cycle C13, but it decreases towards the end when the secondary minima vanish (Fig. 23d).

The P_3 periods are stable and the A_3 amplitude changes are regular during C14 cycle (Fig. 23bc). The minima migration is also regular (Fig. 23d), because the high amplitude $P_3 = 2.^{\text{d}}3895$ periodicity dominates during DATA_{1,13} (Fig. A.63).

15.3. Corridor effect

The CPS-method primary and secondary minimum phases ϕ_2 in Fig. 23d are computed from the ephemeris of Eq. 72. They show that the $P_2 = P_{\text{WK},7}$ periodicity dominates the minima migration in C1, C2 and C13 cycles, as well as in the beginning of C9 cycle. The other periodicity, $P_1 = P_{\text{WK},6}$, dominates in C5, C6, C7, C8, C10, C11, C12 and C14 cycles. The cases of C3 and C4 cycles, and the beginning of C7 cycle, are uncertain. This uncertainty occurs in the segments with low A_1 and A_2 amplitudes (Fig. 10c).

We reverse the above migration trends in Fig. 23e, where the primary and secondary minima phases ϕ_1 are computed from the ephemeris of Eq. 71. Comparison of Figs. 23de reveals that the migration connected to the continuous tilted lines is much more easier to “see” than the migration connected to the horizontal direction. The distance scale between 0.0 and 1.0 for the “horizontal” phases ϕ_2 in Fig. 23d and ϕ_1 in Fig. 23e is much larger than the same distance scale for the “tilted” phases. Thus, the tilted migration always seems more regular than the horizontal migration. For example, the same migration during C1 and C2 cycles seems more irregular in Fig. 23d than in Fig. 23e. The human eye, or the human brain, is easily fooled by this geometrical illusion that we will hereafter call the “corridor effect”.

For example, this corridor effect was utilized to its full potential by Berdyugina & Tuominen (1998, their Fig. 1) when they added an arbitrary number orbital rounds to the *tilted* pairs of migration lines of EI Eri, II Peg and HR 7275. They also plotted the *horizontal* flip-flop pair of migration lines of σ Gem. The corridor effect misguided the visual inspection leading to the discovery of “permanent” active longitudes of three CABSs (EI Eri, II Peg and HR 7275). Our results for the simple 2P-model, the sum of two sinusoids, show that no such permanent pairs of migration lines do exist, or they have to be substituted by at least three pairs of migration lines (see Sect. 7.7: MIGRATION₁, MIGRATION₂ and MIGRATION₃).

16. Discussion

16.1. 2P-method formulation

Jetsu et al. (2017) presented the general light curve model for CABSs and CASSs. This model was based on the JHL-argument. Our definitions for the complex 2P-model and the simple 1P-model are given in Sect. 3 (Eqs. 6 and 7).

The models of one-dimensional period finding methods have unique phases, like the sinusoidal LS-model. There are no such unique phases for presenting the *observed* $g_C(t)$ light curves of the 2P-model (Eq. 6). These $g_C(t)$ light curves are constantly changing, and they can be studied only as a function of time, not as a function of phase. The only unique phases are the ϕ_1 and ϕ_2 phases of the *real* $g_1(t)$ and $g_2(t)$ light curves (Eqs. 3 and 5).

The complex $g_C(t)$ model and the simple $g_S(t)$ model are nested (Sect. 3.3). They are the same model at the diagonal line $f_1 = f_2$ of the $z_C(f_1, f_2)$ periodograms (CASE₁), and when $g_1(t)$ has $A_1 = 0$ (CASE₂) or $g_2(t)$ has $A_2 = 0$ (CASE₃). If none of these three cases occurs, we can compare the complex $g_C(t)$ model and the simple $g_S(t)$ model with the statistical criterion of Eq. 16, and choose which one is the better model for the data.

The earlier 2P-model analysis of thirteen CABSs relied on the fixed P_{act} and $P_{\text{rot}} \approx P_{\text{orb}}$ values (Jetsu et al. 2017). One season of FK Com photometry was also studied with the 2P-model by first solving the fixed P_{act} value, and then solving the fixed P_{rot} value (Sect. 4).

We point out that all results obtained for the stellar SDR with the SI-method and the LC-method are not necessarily true especially if the solar-stellar connection holds (Sect. 5.1-5.2). Nevertheless, those earlier SDR results certainly contradict the JHL-argument (e.g. Strassmeier 2009, Sect. 7). For example, if this argument is true, the earlier SI-method studies should have detected the two constant periods P_{act} and $P_{\text{rot}} \approx P_{\text{orb}}$ of the JHL-argument (the *1st question*). We argue that the parameters $|k|$ (Eq. 18) and $|\Delta\Omega|$ (Eq. 19) of thirteen CABSs support the idea the earlier SI-method studies could have already detected these two periodicities (Table 4). We also present *general* and *particular* evidence for this (Sects. 6.2 and 6.3). These results provide our answer to the *1st question*.

The LC-method gives several estimates for stellar SDR, like the $|k|$ or Z parameters (Eqs. 24, 25 and 28). The values of these parameters are computed from the observed changes of the photometric rotation period under the assumption that $P_{\text{phot}} \approx P_{\text{rot}}$ (Sect. 7.1). Numerous LC-method studies have confirmed that the stellar SDR decreases when P_{phot} decreases (Sect. 7.2). These $P_{\text{phot}} \approx P_{\text{rot}}$ changes in the observed light curves of CABSs and CASSs contradict the JHL-argument (the *2nd question*).

The $P_{\text{phot}} \approx P_{\text{rot}}$ values have usually been determined with the one-dimensional period finding methods, like the LC-method. We simulate artificial data with a simple 2P-model: the sum of two sinusoids (Sect. 7.3). These simulated data are analysed with the LC-method (Sect. 7.3.1-7.3.2). The results for the light curve periods (P_3), amplitudes (A_3) and minimum epochs ($t_{1,\text{min}}$) reveal an effect that we refer to as “incompatibility” (Sect. 7.4). The observed values of all these three parameters change, although the underlying 2P-model does not change at all (Sects. 7.4.1-7.4.3). The incompatibility of the P_3 periods detected with the LC-method, or with any other one-dimensional period finding method, provides answers to the *2nd question* and the *3rd*

question. This incompatibility effect does not only contaminate the LC-method results, because it can also mislead the identification of starspots in the SI-method surface images (Sect. 7.4.4).

Due to the minima-incompatibility effect, our study arrives at a dead end in Sect. 7.5. The K-method analysis of the minimum epochs $t_{\min,1}$ determined with the one-dimensional CPS-method does not give us an unambiguous P_{act} value for FK Com. The relation $P_{\text{rot}} \approx P_{\text{orb}}$ can not be used, because FK Com is not a binary. In other words, we have no *qualitative* or *quantitative* answers for the *4th question* or the *5th question*.

The simple 2P-model, the sum of two sinusoids, is already studied in Sect. 7.3. We show how the periods, the amplitudes and the minimum phases of this particular 2P-model can be solved analytically (Sect. 7.6). These solutions allow us to obtain indirect information of the *real* light curves (the two sinusoids) that cause the *observed* light curve (the sum of two sinusoids). For example, this indirect approach reveals the three migration alternatives MIGRATION_1 , MIGRATION_2 and MIGRATION_3 . These migration alternatives provide *qualitative* answers to the *4th question*, the *5th question* and the *6th question*. For example, perfect flip-flop events $\Delta\phi_b = 0.5$ occur when the two real light curves are equal amplitude sinusoids (Eq. 48).

The above indirect solutions are valid *only*, if the correct complex $g_C(t)$ model is a sum of two sinusoids. In this case, the sum curve $g_C(t)$ is also a sinusoid (Eqs. 37 and 40). For example, if the *observed* $g_C(t)$ light curve has two minima, then at least one of the real $g_1(t)$ and $g_2(t)$ light curves can not be a sinusoid. In this case, the relations for a sum of sinusoids given in Sect. 7.6 are no longer valid. Therefore, the *quantitative* answers to the *4th question* and the *5th question* are still missing. The only way out of this dead end is to formulate of the 2P-method, which gives the unambiguous solutions for all parameters of the 2P-model.

For any pair of fixed tested frequencies f_1 and f_2 , the complex model $g_C(t)$ is linear (Sect. 8.1). The simple $g_S(t)$ model is also linear, if the tested f_3 frequency is fixed (Sect. 8.2). For both models, the least squares fit minimizes the $\chi^2 = \sum_{i=1}^n (\epsilon_i/\sigma_i)^2$ test statistic, as well as gives an unambiguous model solution. For unity weights $\sigma_i = 1$, the periodograms of Eqs. 53 and 55 fulfill $z_C(f_1, f_2) = (\chi^2/n)^{1/2}$ and $z_S(f_3) = (\chi^2/n)^{1/2}$. We do not have to make any additional assumptions, because our $z_C(f_1, f_2)$ and $z_S(f_3)$ periodograms give the same results as the minimization of χ^2 test statistic would give with unity errors $\sigma_i = 1$, or equivalently with equal weights $w_i = \sigma_i^{-2}$. The best frequencies are at the *global* minima of the $z_C(f_1, f_2)$ and $z_S(f_3)$ periodograms. The combination of these two periodograms works like a mirror. It shows the same $z_C(f_1, f_2)$ periodogram at both sides of the diagonal $f_1 = f_2$ line. When approaching the mirror surface, the picture becomes hazy and one has to figure out how to move on the mirror surface. The solution is to search for the best frequency f_3 from the diagonal line $f_1 = f_2$, i.e. to switch from the $z_C(f_1, f_2)$ periodogram to the $z_S(f_3)$ periodogram.

The interpretation of the $z_C(f_1, f_2)$ periodograms is far more complicated than that of the simple $z_S(f_3)$ periodograms (Sect. 9). This interpretation of $z_C(f_1, f_2)$ periodograms is an “art” which requires the creation of new objective characteristics. Those characteristics are defined in Sects. 9.1-9.3, where the results for $\text{DATA}_{2,1}$ are presented. The results for all other 21 segments are presented in the

Appendix. Our period analysis results for the seven pairs of temporally overlapping segments from two different telescopes are compared in great detail in fourteen Sects. A.2-A.15. These results agree well. We summarise the characteristics of individual $z_C(f_1, f_2)$ periodograms in Table 6.

We use preassigned criteria in the selection of the best model for each individual segment. Our criteria for choosing between the conservative and the liberal model are given in Sect. 9.4. The weaker periodic signals, or signals having periodicities too close to each other, are rejected in the conservative models. All periodic signals are accepted in the liberal models, unless the periods of the two signals are the same. In all cases, where the 2P-model and the 1P-model can be compared with the statistical criterion of Eq. 16, the former is statistically the better model for the light curves of FK Com.

16.2. 2P-method analysis

The conservative model results for the photometry of FK Com are summarized in Figs. 9a-f (Sect. 10). The quasi-periodic activity cycle of the mean M has a period between five and seven years (Fig. 9a). The seventeen P_3 period estimates give the weighted mean $P_{w,1} = 2.^d4009$ for the $P_{w,1}$ -group (Eq. 61, Fig. 9b: green continuous line). It seems as if these P_3 periodicities avoid this $P_{w,1}$ level, and are divided into two separate levels $P_{w,2} = 2.^d3954$ of the $P_{w,2}$ -group and $P_{w,3} = 2.^d4048$ of the $P_{w,3}$ -group (Eqs. 62 and 63). The A_3 amplitude changes of the conservative model are quite regular (Fig. 9c), and show some correlation with the level of the mean brightness M (Fig. 9d).

The liberal model results in Figs. 10-13 are more interesting, because the 2P-model is statistically a better model than the 1P-model for the light curves of FK Com (Sect. 11). The levels of the P_1 and P_2 periods of the 2P-model are $P_{w,4} = 2.^d3896$ ($P_{w,4}$ -group: Eq. 64) and $P_{w,5} = 2.^d4053$ ($P_{w,5}$ -group: Eq. 65). These levels are shown in Fig. 10b (red and blue continuous lines). The P_3 periods of the segments, where the 1P-model is the liberal model, coincide with these $P_{w,4}$ and $P_{w,5}$ levels, although these P_3 periods are not used in computing these two levels. Combining these P_3 periods to the above P_1 and P_2 periods gives $P_{w,6} = 2.^d3898$ ($P_{w,6}$ -group: Eq. 66) and $P_{w,7} = 2.^d4050$ ($P_{w,7}$ -group: Eq. 67). The amplitude changes are irregular, because there are some weak signals (Fig. 10c: highlighted symbols). If these weak signals are ignored, the $P_{w,6}$ -group and the $P_{w,7}$ -group stand out as two clearly separate period samples (Figs. 10e-f).

The primary and secondary minimum epochs of the $P_{w,6}$ -group and the $P_{w,7}$ -group are given in Table 11. If these two groups do represent two real separate physical structures, these minima should follow the $P_{w,6}$ and $P_{w,7}$ periodicities. The WK-method analysis of these epochs gives us the ephemerides of Eqs. 71 and 72. The minima distributions of both groups are bimodal (Figs. 11ab). These results indicate that the periods and the minima of the $P_{w,6}$ -group and the $P_{w,7}$ -group are connected. FK Com seems to have two persistent long-lived structures rotating with constant periods $P_{\text{WK},6} = 2.^d39313$ and $P_{\text{WK},7} = 2.^d40762$ (Eqs. 69 and 70). There are some minor deviations, like the weak signals in the years 1998, 2000 and 2003 (Fig. 10b: highlighted symbols). However, this structure is very stable between the years 2004 and 2010,

as illustrated in Fig. 10b, where the red, the blue and the green filled symbols nicely coincide with the red and blue continuous horizontal lines. This kind of starspot distribution stability explains why the SI-method gives extremely low $|\Delta\Omega|$ estimates for some stars. If these two long-lived structures of FK Com are real, they should also show in the two MLCs computed from Eqs. 71 and 72. This is confirmed in Figs. 12 and 13.

The 2P-method analysis results for all y_i data are shown in Figs. 14-16 (Sect. 13). The $z_C(f_1, f_2)$ periodogram resembles a patchwork quilt, because the real $g_1(t)$ and $g_2(t)$ light curves evolve *between* and *within* the segments (Fig. 14). For this reason, it is impossible to model all data with a single 2P-model or 1P-model (Figs. 15-16).

Our results for the seven pairs of temporally overlapping segments from two different telescopes already confirm the performance of the 2P-method (Appendix: Sects. A.2-A.15). As an additional test for this method, we also check that our new method gives the correct results for the simulated data of $\text{TEST}_{a_1=a_2}$ and $\text{TEST}_{a_1 < a_2}$, and it does (Sects. 14.1-14.2: Figs. 17-22).

The connection between the CPS-method analysis results of Table 3 and the ephemerides of Eqs. 71 and 72 is illustrated in Figs. 23a-e (Sects. 15.1-15.2). The two long-lived structures rotating with constant periods can explain many general CPS-method analysis results for all data, as well as for individual segments. We also discuss the corridor effect (Sect. 15.3). Due to this effect, the tilted migration lines appear more reliable than the horizontal migration lines in Figs. 23d-e. This effect can be enhanced by adding an arbitrary integer number of rotations to the phases of these tilted migration lines, like in Berdyugina & Tuominen (1998, their Fig. 1) or in our Fig. 1a.

16.3. 2P-method physical indications

The JHL-argument does not rule out the formation and decay starspots in late-type stars. For example, such starspot distribution evolution has been undeniably confirmed by direct interferometric observations of ζ And (Roettenbacher et al. 2016). However, the results presented in the previous Sect. 16.2 confirm that the time scale of starspot formation and decay in FK Com is much longer than the earlier one month estimates (e.g. Jetsu et al. 1993; Hackman et al. 2013). In absence of the erratic short-lived starspots and the abrupt flip-flop events, it is much easier to find a physical model explaining the slower less irregular starspot distribution changes of FK Com. This model can be geometrically simple and temporally nearly stable. For example, a large long-lived magnetic loop would suffice, if the starspots at the feet of this loop rotate with different angular velocities. Such a large loop has been observed directly in the radio images of the active K0 IV component of Algol, where this structure was oriented towards the inactive B8 V component (Peterson et al. 2010). This result may indicate that the stationary $P_{\text{orb}} \approx P_{\text{rot}}$ part dominated in those radio images of Algol, because this loop was parallel to the line connecting the centres of the two members of this binary.

Most of the seasonal real $g_1(t)$ and $g_2(t)$ light curves of FK Com have only one minimum, although their shape is not always strictly sinusoidal. In the liberal models, two real $g_1(t)$ light curve minima are present in *six* segments out of a total of 22 segments (Figs. A.8e, A.11e, A.23e, A.29e, A.8e and A.50e). Two minima are present *only in one* low

$A_2 = 0.^m029$ amplitude real $g_2(t)$ light curve (Fig. A.20f). Hence, a second large magnetic loop might be needed to explain the light curves of some segments. No such a second loop would be needed to explain the majority of real light curves of the remaining segments, $15/22 \equiv 68\%$, which have only one $g_1(t)$ or $g_2(t)$ minimum.

The long-lived starspots of FK Com could even be vortices resembling the Great red spot of Jupiter (e.g. Mantere et al. 2011; Käpylä et al. 2011), except that the extreme chromospheric and the coronal activity of FK Com, “the king of spin”, can not be explained without the presence of strong magnetic fields (Ayres et al. 2016). The light curves of this star have been monitored only for about half a century. If essentially the same starspot pattern is observed indefinitely, we will get very accurate P_1 and P_2 estimates, if “nothing happens”. However, if we keep on finding this “boring” combination of long-lived starspots in CABSSs and CASSs for the next millions of years, there are striking similarities in the geometries of magnetic fields in early-type and late-type stars, as already pointed out by Jetsu et al. (2017, Sect. 7). The similarity between the oblique rotator of early-type stars and the large magnetic loop of late-type stars would be the stationary starspot. The difference would be the non-stationary starspot at the other end of the large magnetic loop of late-type stars. The reason for this difference may be the interaction between convection and magnetic fields which complicates things in the late-type stars, while the magnetic fields in the fully radiative early-type Ap and Bp stars are stable (e.g. Jetsu et al. 1992; Shultz et al. 2018).

In the synchronously rotating CABSSs, the relation $P_{\text{rot}} \approx P_{\text{orb}}$ can be used to check whether the P_1 or P_2 period represents the stationary period P_{rot} . Although this is not possible for FK Com, this single star seems to “act” like a binary star. Both of the two P_1 or P_2 periods are still observed, although both members of this hypothetical coalesced W UMa binary are no longer present. This is not unusual for single stars. For example, Lehtinen et al. (2012, their Fig. 4) showed that one period clearly dominated the regular *horizontal* migration of the primary and secondary minima of the *single* main sequence star LQ Hya in many segments. However, a second different period certainly dominated the *tilted* migration during their segment “SEG 14”.

In the next Sects. 16.4–16.5.8, we discuss what are the other consequences, *if* the JHL-argument is true.

16.4. Consequences for SI-method

We have already noted that the SI-method can, and most probably does, detect the non-stationary and stationary starspots of the 2P-model (Sect. 6.3: cases of II Peg and FK Com in Berdyugina et al. 1998; Korhonen et al. 2000). The main weakness of this method is the map-incompatibility (Sect. 7.4.4): comparison of surface images over time intervals longer than $P_{\text{lap}}/2$ is ambiguous. After this time interval, it becomes next to impossible to determine, if any starspot A has moved backwards with respect to any other starspot B, or vice versa.

16.5. Consequences for LC-method

We discuss the consequences of the JHL-argument for the LC-method analyses in a broader context, because these consequences are not limited only to the stellar SDR estimates.

16.5.1. Cycles of the mean M

It is usually assumed that the mean brightness M measures the projected area covered by the starspots (e.g. Jetsu et al. 1993). The value of M does not depend on the applied period finding method, because an estimate can be obtained directly from the mean of the data. Hence, there is no incompatibility in the activity cycles detected from the M changes.

16.5.2. Cycles of the period P_3

The photometric rotation period P_3 estimates obtained with any one-dimensional period finding method suffer from the period-incompatibility (Sect. 7.4.1). Any cycles detected in these P_3 periods are not real activity cycles (e.g. Distefano et al. 2017). For example, the apparently quasi-periodic P_3 changes of our simulated data in Fig. 3b represent random fluctuations, as well as the P_3 changes of the real FK Com data in Fig. 23b.

16.5.3. Cycles of the amplitude A_3

If the JHL-argument is true, the A_3 amplitude estimates determined with any one-dimensional period finding method are also incompatible (Sect. 7.4.2). If the real light curves $g_1(t)$ and $g_2(t)$ follow the periods P_1 and P_2 , then the A_3 amplitude changes follow the P_{lap} lap cycle (Eq. 32). This cycle is not an activity cycle, because it is not connected to the number, the area or the temperature of starspots.

For example, Ferreira Lopes et al. (2015) used the observed amplitude A_3 as a proxy for stellar activity. Some studies use the activity index which is also proportional to this A_3 amplitude (e.g. Arkhypov et al. 2015, their A_1 parameter). Unfortunately, a time interval of constant brightness light curve does not mean that the starspots are absent, nor that the stellar surface is fully covered with starspots. Therefore, the studies of the *observed shape* of the light curve (e.g. Reinhold & Arlt 2015) do not either tell anything about the distribution or the latitudes of starspots.

16.5.4. Cycles of the minima $t_{\text{min},1}$ and $t_{\text{min},2}$

The light curve minima $t_{\text{min},1}$ and $t_{\text{min},2}$ determined with any one-dimensional period finding method suffer from minima-incompatibility (Sect. 7.4.3), and may display flip-flop cycles (e.g. Berdyugina & Tuominen 1998). These cycles are not activity cycles, because they follow the P_{lap} lap period cycle. The magnitude of the $\Delta\phi_b$ phase shifts depends on the amplitudes A_1 and A_2 (Eq. 48). The P_{lap} cycles of flip-flop events are not so easy to detect as the P_{lap} cycles of A_3 , because a “perfect” $\Delta\phi_b = 0.5$ flip-flop requires $A_1 \approx A_2$. These cycles can also be shorter than P_{lap} . For example, if the $g_1(t)$ and $g_2(t)$ curves are double waves, the resulting flip-flop cycle is $P_{\text{lap}}/2$. The periods $P_1 = 2.^{\text{d}}39313 \pm 0.^{\text{d}}00028$ and $P_2 = 2.^{\text{d}}40762 \pm 0.^{\text{d}}00028$

(Eqs. 69 and 70) give $P_{\text{lap}} = 398^{\text{d}} \pm 13^{\text{d}}$. This means that a perfect flip-flop event of FK Com is ($A_1 \approx A_2$), or is not ($A_1 \neq A_2$), observed after every thirteenth month. The “phase jumps” and the flip-flop events of FK Com identified by Oláh et al. (2006) are simply manifestations of different $\Delta\phi_b$ values.

The first flip-flop cycles were detected in four CABSs (Berdyugina & Tuominen 1998), and quite soon also in FK Com (Korhonen et al. 1999). Elaborate dynamo models have been developed to explain these spurious cycles (e.g. Pipin & Kosovichev 2015; Viviani et al. 2017). The flip-flop of FK Com is discussed in detail in the Sect. 16.5.6, where we present the short history of this phenomenon.

16.5.5. Photometric activity cycles in general

An innumerable number of activity cycles of CABSs and CASSs have been detected in all the above five light curve parameters M , P_3 , A_3 , $t_{\text{min},1}$ and $t_{\text{min},2}$ when the estimates for these parameters have been determined with the one-dimensional period finding methods. Many sophisticated physical models and theories of stellar magnetic fields are based on these cycle detections. If the JHL-argument is true, the only real activity cycles may have been detected from the changes of the mean M . Some additional examples of the consequences are given below.

Rieger et al. (1984) detected a 154^d cycle in the solar high energy γ -ray flares. Since then, this Rieger cycle has also been detected in numerous other solar activity indicators, e.g. the sunspot area (Lean 1990; Oliver et al. 1998), the solar flares (Bai & Sturrock 1993; Bai 2003) or the Mt Wilson Sunspot Index (Ballester et al. 2002, MWSI). Stellar Rieger cycle analogues have also been detected (e.g. Massi 2007; Lanza et al. 2009; Bonomo & Lanza 2012; Distefano et al. 2017). The *observed* light curves have usually been first analysed with the most widely used one-dimensional period finding method, the LS-method. Then the quasi-periodic amplitude A_3 and period P_3 changes have been analysed with the same method (e.g. Distefano et al. 2017). This has revealed short-term quasi-periodic A_3 and P_3 changes which have been interpreted as stellar Rieger cycle detections. Unfortunately, the *observed* A_3 and P_3 values analysed in the above studies have nothing to do with the real amplitudes (A_1, A_2) and the real periods (P_1, P_2) of the 2P-model. As for longer A_3 and P_3 cycles, Reinhold et al. (2017) analysed a large sample of 23601 stars with the LS-method. They detected long-term activity cycles in the A_3 amplitudes, but not in the P_3 periods. Their results support the JHL-argument, because the long-term P_{lap} cycles can be detected in A_3 , but not in the long-term random P_3 changes. Only short-term quasi-periodic random fluctuations can be detected in the P_3 periods.

Lehtinen et al. (2016) studied the activity trends in 21 young solar-type stars. The mean M , the period P_3 and the amplitude A_3 estimates were determined with a one-dimensional period finding method, the CPS-method. Activity cycles were detected from the M , A_3 , $M - A_3/2$ and $M + A_3/2$ long-term changes. If the JHL-argument is true, then only the M cycle detections may have been real activity cycle detections, but the P_3 and A_3 estimates were unreliable due to the period- and the amplitude-incompatibility. Hence, the A_3 , $M - A_3/2$ and $M + A_3/2$ cycles were not real activity cycles. Lehtinen et al. (2016, Fig. 14) studied the connection between the cycle periods

P_{cyc} and several other physical parameters. For example, the P_3/P_{cyc} ratios were compared to those obtained by Brandenburg et al. (1998) and Saar & Brandenburg (1999). Since then, the results of the analysis based on the above M , A_3 , P_3 and P_{cyc} estimates in Lehtinen et al. (2016) have already been found to support the results presented in numerous observational and theoretical studies (e.g. See et al. 2016; Viviani et al. 2017; Olsper et al. 2017; Warnecke 2017; Özavcı et al. 2018; Distefano et al. 2017; Fabbian et al. 2017; Brandenburg et al. 2017; Reinhold et al. 2017; Nielsen et al. 2017; Wargelin et al. 2017; Siltala et al. 2017; Flores Soriano & Strassmeier 2017; Lanzafame et al. 2018; Kóspál et al. 2018; Alekseev & Kozhevnikova 2018; Brandenburg 2018). One of the main results reported in Lehtinen et al. (2016, their Fig. 14) was that the active longitudes are detected only in the solar-type stars where strong chromospheric Ca II H&K emission is observed. If there are no active longitudes, this result indicates that the stationary and non-stationary starspots are stronger and more stable in these stars.

16.5.6. Short history of flip-flop

Here, we tell the short history of the flip-flop phenomenon. Jetsu et al. (1991, 1993) discovered these events in the light curves of FK Com. For a quarter of a century, the starspots had concentrated on two active longitudes separated by 180 degrees. An abrupt shift from one active longitude to another had happened only three times. This result also indicated weak SDR in FK Com.

The next flip-flop was soon discovered (Jetsu et al. 1994). The models of non-axisymmetric stellar magnetic fields failed to explain this phenomenon (e.g. Moss et al. 1995). Similar active longitudes were discovered in CABSs (e.g. Jetsu 1996; Berdyugina & Tuominen 1998), as well as in the Sun (e.g. Jetsu et al. 1997). Moss & Tuominen (1997) modelled the non-axisymmetric magnetic fields of CABSs. Moss (1999) demonstrated that the non-linear solar dynamo models could produce weak large-scale non-axisymmetric magnetic field structures. Tuominen et al. (2002) predicted that the flip-flop phenomenon is the stellar counterpart of Hale’s polarity law in the bipolar sunspots, and that the future observations may confirm this “active star Hale polarity rule”. Berdyugina & Usoskin (2003) analysed 120 years sunspot observations and discovered two persistent active longitudes separated by 180 degrees. Pelt et al. (2005) argued that this result was biased, and this debate continues (Berdyugina 2007; Balthasar 2007; Vernova et al. 2007; Tuominen et al. 2007; Gyenge et al. 2014). There are numerous dynamo models that can explain the flip-flop phenomenon and the active longitudes (e.g. Elstner & Korhonen 2005; Korhonen & Elstner 2005; Berdyugina et al. 2006; Korhonen & Elstner 2011; Mantere et al. 2013; Cole et al. 2014; Pipin & Kosovichev 2015; Viviani et al. 2017). These models have also been used to infer the coronal structure of FK Com (Drake et al. 2008; Cohen et al. 2010).

The first SI-method study of FK Com indicated that the flip-flop events between the two active longitudes may follow a mean cycle of 6.5 years (Korhonen et al. 1999). A long-lived starspot rotating with a constant period of 2.^d4037 was discovered in the next SI-method study, as already mentioned earlier in our Sect. 6.3. Korhonen et al.

(2001b) reported indications of three and six year flip-flop cycles. The first surface images that confirmed the flip-flop phenomenon of FK Com were published by Korhonen et al. (2001a). The next two SI-method studies indicated flip-flop cycles of 6.4 years (Korhonen et al. 2002) and 2.6 years (Korhonen et al. 2004). No such cycles were detected in the 25 surface imaging maps studied by Korhonen et al. (2007). The reason for this result can now be understood. FK Com is an “ideal” star for fooling its observers, because the $P_{\text{lap}} = 398^{\text{d}}$ lap cycle period causes extremely misleading map-incompatibility effects, especially if the surface images are obtained during the same season of each year.

The JHL-argument neatly explains the flip-flop phenomenon (Eq. 48). Considering that the past quarter of a century has been wasted in trying to find a physical cause for this phenomenon, it was absurd to question the person *who* actually first detected this phenomenon and gave it its name (Tuominen et al. 2002, Sect. 2.1). We guess that no-one wants to take that credit now. Nevertheless, we quote the following sentence from Moss & Tuominen (1997): “*The visible fields then have maxima at the longitudes corresponding to the intersection of the line of centres with the stellar surfaces.*” Although the cause of the flip-flop phenomenon was misunderstood at that time, this particular dynamo model result agrees perfectly with the 2P-model, because the MLC minima of stationary starspots in fourteen CABSs concentrated on this intersection line (Jetsu et al. 2017, Figs. 1-14, “b-g” panels).

16.5.7. Active longitudes, starspot life-times and starspot migration

The active longitudes appeared to be long-term stable structures rotating with a constant period (e.g. Jetsu et al. 1993). This concept was introduced, because the starspot life-times seemed to be about one month and the observed photometric rotation periods of these starspots were changing. It was suggested that the starspots first formed on these longitudes, then detached from these structures, and finally migrated with their own particular angular velocity before decaying. If the JHL-argument is correct, there are no active longitudes where the starspots form, migrate and decay. There are only two long-lived starspots that rotate with their own constant angular velocities. Their longitudes are stationary and non-stationary in the rotating reference frame.

If the JHL-argument is true, the analysis of short photometric samples with any one-dimensional period finding method gives the impression that a lot happens, although practically nothing happens. The CABSs and CASSs appear very lively when in fact they are not. For example, Giles et al. (2017) analysed the *Kepler* satellite light curves with the LS-method, and noted that the amplitudes and phases of these light curves gradually vary due to rapid starspot formation and decay. This LS-method failure in modelling time intervals longer than about one month has nothing to do with the starspot life-times. The 2P-method can sometimes model over seven months of data with no starspot decay at all (e.g. Figs. A.46 and A.47).

Table 12. Performance of the 1P-method. The first column gives the segments, where the 2P-model is the liberal model (Segment). The second column gives the section, where the period analysis is described (Section). The parameters $\Delta P_{1,3}$ and $\Delta P_{2,3}$ of Eqs. 74 and 75 are given on the next columns. The units of both parameters are $[\sigma_{P_3}]$. The last column gives our qualitative estimate for the number of correct P_1 or P_2 period detections with the 1P-method (n_{det}).

Segment	Section	$\Delta P_{1,3}$	$\Delta P_{2,3}$	n_{det}
DATA _{1,1}	A.3	33.6	1.9	1
DATA _{2,4}	A.4	1.2	35.0	2
DATA _{1,2}	A.5	0.6	58.6	2
DATA _{2,5}	A.6	79.5	2.3	1
DATA _{1,3}	A.7	1.3	36.3	1
DATA _{2,6}	A.8	41.2	2.3	1
DATA _{2,7}	A.10	8.0	9.9	0
DATA _{1,5}	A.11	24.0	5.0	0
DATA _{1,6}	A.12	3.0	39.3	1
DATA _{2,8}	A.13	1.0	29.7	1
DATA _{1,7}	A.14	9.8	18.3	0
DATA _{1,8}	A.16	12.0	17.0	0
DATA _{1,9}	A.17	40.5	7.7	0
DATA _{1,10}	A.18	3.6	25.0	0
DATA _{1,11}	A.19	27.6	8.7	0

16.5.8. Multiple period detections

Our results for the real data of FK Com allow us to estimate the performance of one-dimensional period finding methods in detecting multiple periodicities. We estimate this performance when the 2P-model is the liberal model. In these cases, the criterion of Eq. 16 has already confirmed the 2P-model is certainly a better model than the 1P-model. Therefore, P_1 and P_2 periods detected with the 2P-method can be compared to the P_3 period detected with the 1P-method. We compute the dimensionless parameters

$$\Delta P_{1,3} = |P_1 - P_3|/\sigma_{P_3} \quad (74)$$

$$\Delta P_{2,3} = |P_2 - P_3|/\sigma_{P_3}. \quad (75)$$

They measure the distance of the P_3 value from the P_1 and P_2 values in units of σ_{P_3} . We can also make a qualitative estimate of how many correct periods the 1P-method does detect (n_{det}). Our results are summarized in Table 12.

There are eight cases where $\Delta P_{1,3} \leq 3$ or $\Delta P_{2,3} \leq 3$, and 22 cases where $\Delta P_{1,3} > 3$ or $\Delta P_{2,3} > 3$. In the former eight cases, our estimate is $n_{\text{det}} \geq 1$. There are two segments where our qualitative estimate is $n_{\text{det}} = 2$, because Figs. A.12ab and A.15ab show that the 1P-method can detect nearly the correct values of both P_1 and P_2 periods. This raises the total number of correct detections to ten. There are fifteen segments in Table 12. Hence, the total number of real P_1 or P_2 periods not detected with the 1P-method is $2 \times 15 - 10 = 20 \equiv 66.7\%$.

We write in several cases that the 1P-method detects “signs” of the real P_1 or P_2 periods. Although in many of these cases the $\Delta P_{1,3}$ or $\Delta P_{2,3}$ distance is shorter than $\pm 3\sigma_{P_3}$, this does not mean that the 1P-method detects the correct numerical P_1 or P_2 period value. The $z_S(f_3)$ and $z_{\text{LS}}(f_3)$ periodograms of TEST _{$a_1=a_2$} and TEST _{$a_1<a_2$} simulated data are typical examples of this discrepancy (Figs. 18ab and 21ab).

Our analysis of all segments confirms that the periods detected with the 1P-method and the LS-method are practically the same. Hence, the conclusions drawn here about the performance of the 1P-method apply also to the LS-method. Since the period-incompatibility causes this result, the performance of any other one-dimensional period finding method, like the CPS-method, can not be any better.

Reinhold & Reiners (2013) applied the LS-method to detect multiple periodicities from the *Kepler* space telescope light curves of thousands of stars. They applied the LS-method to determine the first best P_3 value for the original data, and then they removed this periodic sinusoid from the data. The residuals were analysed again with the LS-method to search for the second best period. This gave the next residuals, and the pre-whitening continued. Our TEST _{$a_1=a_2$} and TEST _{$a_1<a_2$} simulations are exactly the cases that Reinhold & Reiners (2013) were trying to find from the real data: the sum of at least two sinusoids. Our Table 12 shows how frequently the real periods are missed in their pre-whitening approach, if the data contains *only two* sinusoids. We have already confirmed that the 2P-method certainly detects any such two sinusoids (Sects. 14.1 and 14.2). If the JHL-argument is true, there are numerous uncertainties in the above pre-whitening approach that has been used to estimate stellar SDR. We mention some of those uncertainties below.

- 1st uncertainty: The results in our Table 12 indicate that the probability for simultaneous correct detection of both periods with the 1P-method is only $2/15 \equiv 13\%$. The probability for detecting the correct P_1 or P_2 value is about 33%. Both of the above probabilities are actually smaller, because our $\pm 3\sigma_{P_3}$ criterion for the $\Delta P_{1,3}$ and $\Delta P_{2,3}$ differences is conservative. With the $\pm 1\sigma_{P_3}$ criterion, this detection probability would drop from 33% to $2/30 \equiv 6.7\%$.
- 2nd uncertainty: The best P_3 period for the original data is not exactly the real period P_1 and/or P_2 , unless $A_1 = 0$ or $A_2 = 0$. This contaminates all next steps of the pre-whitening process.
- 3rd uncertainty: If the difference between the frequencies of the two real P_1 and P_2 periods is comparable to $f_0 = 1/\Delta T$, the LS-method can not separate the P_1 and P_2 periodogram peaks, and the first stage of pre-whitening eliminates both of the P_1 and P_2 signals (e.g. Figs. A.27 or A.30). The probability for obtaining the correct value for the best P_3 period of the original data depends on this $|P_1 - P_2|$ difference, as well as on the amplitudes A_1 and A_2 (Eqs. 39, 45 and 46).
- 4th uncertainty: Our residuals in many 2P-models are comparable to the accuracy of the data. Hence, the first two periodic sinusoids of the pre-whitening process should suffice. No third periodic sinusoid is required, let alone a combination of ten harmonics (Reinhold & Art 2015).
- 5th uncertainty: The phase shifts $\Delta\phi_b$ (Eq. 48) can totally mislead the LS-method analysis, especially the flip-flop events (e.g. Sect. 14.1: Fig. 19).
- 6th uncertainty: The *observed* $g(t)$ light curves, or the *real* $g_1(t)$ and $g_2(t)$ light curves, are not always sinusoids. Thus, the sinusoidal LS-model is not always the correct model.
- 7th uncertainty: If the tested period interval of any one-dimensional period finding method increases, then the

ranges of P_3 , Z and k increase (e.g. Fig. 4). We encounter no such problems with our two-dimensional period finding method. We have tested the $\pm 10\%$ period range for all 22 segments. Except for all solutions already obtained for the $\pm 3\%$ range, these $z_C(f_1, f_2)$ periodograms for the $\pm 10\%$ range show vast dark blue areas (i.e. noise at the continuum level $z_{C,\max} \approx \sigma_y$) and no white patches (i.e. additional alternative model solutions close to the $z_{C,\min}$ level).

The above mentioned uncertainties have numerous consequences for the currently accepted stellar SDR measurements (e.g. Reinhold et al. 2013; Reinhold & Reiners 2013; Reinhold & Gizon 2015; Lehtinen et al. 2016). For example, the SDR estimates have been too large due to the 3rd uncertainty which prevented the detection of the two real periods when the $|P_1 - P_2|$ difference was small.

If the same phenomenon is measured at the same time in the same star, the result should be the same. But this is not the case when the LS-method is used to measure P_3 , $|k|$ or Z from two simultaneous samples of photometry (Sect. 7.4.1). The LS-method gives *different* P_3 , $|k|$ and Z estimates for the *same* star when this star is observed with two different telescopes at the *same* time. These P_3 , $|k|$ and Z estimates do not measure SDR, they measure the random failures of the LS-method when the analysed data contain two signals having a constant period and a constant amplitude. In short, the first stage of pre-whitening usually fails. Since Kron (1947) discovered the starspots, we have forced the CABSs and CASSs to play only one tune, instead of two (Sect. 6: All equations). When searching for multiple periodicities, the pre-whitening with the simple sinusoidal LS-model can also mislead studies in asteroseismology (e.g. Kraus et al. 2015; Saio et al. 2018), exoplanet detection (e.g. Queloz et al. 2009; Hatzes 2013) and many other fields (e.g. Reyniers et al. 2009), especially if the real periods are too close to each other.

Our two-dimensional period finding method, the 2P-method, uses a linear model based on the χ^2 minimization, and it gives unambiguous solutions for all model parameters. The number of other suitable $g_1(t)$ and $g_2(t)$ functions, like higher harmonics, is unlimited. The application of our 2P-method has also its limitations.

Firstly, the interpretation of two-dimensional $z_C(f_1, f_2)$ periodograms is not easy, because it requires the study of the numerous characteristics defined in Sects. 9.1-9.3.

Secondly, a fast computation of these periodograms and the combined bootstrap approach require an efficient computer. Due to these first two limitations, the sliding window approach, similar that used in the CPS-method by Lehtinen et al. (2012), is difficult with the 2P-method. The easiest solution for an automated analysis would be to choose the liberal models. This would require only the testing of the “ $\pm 3\sigma_{f_1, f_2}$ hits $f_1 = f_2$ ” cases (Sect. 9.1.4). If the answer is “Yes”, the correct model is the 1P-model, otherwise the criterion of Eq. 16 can be used to decide between the 1P-model and the 2P-model.

Thirdly, we removed the changes of the mean with a second order polynomial (Eq. 1), while Jetsu et al. (2017) removed only a linear trend before applying the 2P-model. This procedure does sometimes mislead the analysis, which shows as regular trends in the residuals (e.g. Fig. 21c). One solution would be to modify the $g_C(t)$ model by adding and m :th order polynomial to it. Then again, this $\sum_{i=0}^m M_i t^i +$

$g_C(t)$ model would have even more free parameters. This alternative might be tested in the future.

Fourthly, the detection of the correct P_1 and P_2 period values requires very long segments, especially for small $|P_1 - P_2|$ differences. If the P_1 and P_2 period values are known, the 2P-model can be applied to short segments.

16.6. Generalized multiperiodicity search and other nonlinear inverse problems

In our 2P-method, we utilize the symmetry $z_C(f_1, f_2) = z_C(f_2, f_1)$, and test only the $f_1 > f_2$ frequency pairs. It is easy to generalize this method to higher dimensions. For example, a three-dimensional version could test frequency triples $f_1 > f_2 > f_3$ within an arbitrary frequency interval. If the approximately known real correct frequencies in the data are not close to each other (e.g. Mennickent 2017; Saio et al. 2018), the tested frequencies could be $l_1 < f_1 < l_2$, $l_3 < f_2 < l_4$ and $l_5 < f_3 < l_6$, where the numerical l_1, \dots, l_6 values for the tested frequency ranges can be adjusted, as long as the tested values fulfill $f_1 \neq f_2$, $f_1 \neq f_3$ and $f_2 \neq f_3$. The number of suitable $g_1(t)$, $g_2(t)$ and $g_3(t)$ functions for this three-dimensional period finding method, like higher harmonics, is unlimited.

The nonlinear $g(\bar{\beta})$ models represent an ill-posed inverse problem, because finding an unambiguous solution for the free parameters $\bar{\beta}$ is difficult or impossible. There are sophisticated analytical solutions for this problem (e.g. Tarantola & Valette 1982; Snieder 1998; Kaltenbacher et al. 2008). In our numerical solution for a nonlinear model, the free parameters $\bar{\beta}$ are divided into two groups.

- $\bar{\beta}_I$ group: The partial derivatives $\partial g / \partial \beta_i$ of these free parameters *do not contain any* free parameters, *if* the $\bar{\beta}_{II}$ group free parameters are fixed to constant numerical values.
- $\bar{\beta}_{II}$ group: The partial derivatives $\partial g / \partial \beta_i$ of these free parameters *contain at least one* free parameter, *even if* the $\bar{\beta}_I$ group free parameters are fixed to constant numerical values.

In the 2P-model, the amplitudes $B_1, B_2, C_1, C_2, D_1, D_2, E_1$ and E_2 belong to the $\bar{\beta}_I$ group, and the frequencies f_1 and f_2 belong to the $\bar{\beta}_{II}$ group. When the $\bar{\beta}_{II}$ group numerical values are fixed, the solutions for the second $\bar{\beta}_I$ group are unambiguous. This kind of a linearization can be applied to any arbitrary nonlinear model. The test statistic $z(\bar{\beta}_{II})$ of the nonlinear model can be, for example $(\chi^2/n)^{1/2}$, χ^2 or the sum of squared residuals used in Eq. 15. The correlation of $z(\bar{\beta}_{II})$ values that are close to each other in the $\bar{\beta}_{II}$ space can be used to find the suitable density for the grid of the tested $\bar{\beta}_{II}$ values (e.g. Jetsu & Pelt 1996, their Fig. 2). The tested $\bar{\beta}_{II}$ range of can be fixed, e.g. with physical or any other reasonable criteria. Our simple recipe for solving the free parameters of any nonlinear model is

- Identify the $\bar{\beta}_I$ and $\bar{\beta}_{II}$ groups
- Fix the tested $\bar{\beta}_{II}$ grid
- Compute $z(\bar{\beta}_{II})$ with a linear least squares fit
- Global $z(\bar{\beta}_{II})$ minimum gives the best $\bar{\beta}_I$ and $\bar{\beta}_{II}$ values

This approach gives only a *numerical* solution for the free parameters. The bootstrap approach can be used to solve the errors of these free parameters (e.g. Eq. 54). In conclusion, this type of numerical approach requires a lot of

computation time, but it gives an unambiguous solution for the free parameters β of any nonlinear model $g(\beta)$. In case of the nested models, the criterion of Eq. 16 can be used to decide what is the best model among the different model alternatives.

16.7. Consequences for stellar SDR

If the JHL-argument is true, the earlier SI-method estimates for the rotation periods of starspots can be reliable, except for the map-incompatibility effect (Sect. 7.4.4). All earlier LC-method estimates of SDR which have been obtained with the one-dimensional period finding methods are useless, because they failed to model the real light curves of two starspots rotating with different periods. The irony in all this is that these methods could not have measured stellar SDR even if it were present, except perhaps for the large $|P_1 - P_2|$ period differences. If the CABSs and CASSs have two long-lived starspots rotating with constant periods, the current ideas of stellar SDR need to be revised, because the erratic short-lived starspots are history.

One could argue that the 2P-model is only a mathematical model, but that it is not a suitable physical model for the stellar SDR. Most of the models in modern natural sciences are mathematical. We have shown that the simple mathematical sinusoidal LS-model is not the correct model for the light curves of CABSs and CASSs. The LS-method is easy to apply and it therefore tempting to end the period analysis at that. The spurious SDR estimates obtained with this simple mathematical sinusoidal model have been widely and uncritically accepted for decades, except for a few studies (e.g. Loumos & Deeming 1978; Aigrain et al. 2015). Our general solution for the free parameters of nonlinear models gives unambiguous results for *any data* (Sect. 16.6). It is not connected only to the *photometric data* of CABSs and CASSs. We argue, on the contrary, that the 2P-model is a good mathematical and physical model, because it can explain so many observed phenomena in the light curves of CABSs and CASSs. What is a better mathematical model from the physical point of view? Is it the LS-model that requires dramatic short-term changes in the starspot distribution of the object? Or, is it the 2P-model that requires no such dramatic short-term changes in the object? This would make sense, because the magnetic fields in CABSs and CASSs are much stronger than those in the Sun. Hence, it would be logical that the starspot life-times exceed the sunspot life-times. We do not claim that the 2P-model is perfect, but it certainly does reveal that the chromospherically active stars are not so “lively” objects as suggested by the earlier LS-method analyses. It is high time to stop looking for something that is not there.

17. Conclusions

We prove that the following argument is true:

- JHL-argument: “The *observed* light curves of chromospherically active binary and single stars are interference of two *real* constant period light curves of long-lived starspots. These constant periods are the non-stationary active longitude period P_{act} and the stationary rotation period $P_{\text{rot}} \approx P_{\text{orb}}$.”

Our argument contradicts the current widely held views about stellar surface differential rotation and starspots in

general. For this reason, we make six specific questions which undermine the validity of our argument (Sect. 1).

Those six questions are repeated below, where we answer them. The two periods of the 2P-model fulfill $P_1 < P_2$. In our answers below, these P_1 and P_2 periods can refer to P_{act} , P_{rot} or P_{orb} , depending on the object. The synchronously rotating chromospherically active *binary* stars may have $P_1 = P_{\text{act}}$ and $P_2 = P_{\text{rot}} \approx P_{\text{orb}}$, or $P_1 = P_{\text{rot}} \approx P_{\text{orb}}$ and $P_2 = P_{\text{act}}$, while the chromospherically active *single* stars, like FK Com, may have $P_1 = P_{\text{act}}$ and $P_2 = P_{\text{rot}}$, or $P_1 = P_{\text{rot}}$ and $P_2 = P_{\text{act}}$. For the synchronously rotating *binary* stars, the relation $P_{\text{rot}} \approx P_{\text{orb}}$ can be used to check, if the P_1 or P_2 period represents the stationary P_{rot} period in the rotating reference frame. This is not possible for the *single* stars, like FK Com.

Here are the six specific questions mentioned in our Abstract, and our answers to those questions:

- *1st question:* Why have these two constant periods, the non-stationary active longitude period P_{act} and the stationary rotation period $P_{\text{rot}} \approx P_{\text{orb}}$ of the JHL-argument, *not* been detected in the surface images?
Answer: The *general* and the *particular* evidence strongly indicate that these two constant periods have already been detected in the surface images (Sects. 6.1-6.3). The identification of the *same* starspot in many *different* surface images is ambiguous over longer periods of time (Sect. 7.4.4: map-incompatibility after $P_{\text{lap}}/2$).
- *2nd question:* Why have these two constant periods, the non-stationary active longitude period P_{act} and the stationary rotation period $P_{\text{rot}} \approx P_{\text{orb}}$ of the JHL-argument, *not* been detected in the light curves? Why are so *many different* $P_{\text{rot}} \approx P_{\text{phot}}$ periods *observed* in the light curves of the *same* star, if the photometric data contains only these two constant periods?
Answer: If the JHL-argument is true, the *observed* light curve is constantly changing. The one-dimensional period finding methods “detect” *many different spurious* P_3 periods for the *same* star, although the underlying two *real* light curves remain the *same*, and the two *real* P_1 and P_2 periods remain the *same* (Sects. 7.1-7.7, 15).
- *3rd question:* Why do the surface images and the light curves give *different* surface differential rotation estimates even for the *same* individual star?
Answer: The surface imaging methods can detect the *real* P_1 and/or P_2 periods, but the one-dimensional period finding methods “detect” many *spurious* P_3 periods from the observed light curve.
- *4th question:* Hackman et al. (2013) applied the Kuiper method to the $t_{\text{min},1}$ light curve minima of FK Com. Does this kind of an analysis give an *unambiguous* estimate for the non-stationary active longitude period P_{act} of the JHL-argument?
Answer: Due to the minima-incompatibility, the Kuiper method can not detect an unambiguous non-stationary active longitude period P_{act} value for FK Com. The 2P-method detects the unambiguous P_1 and P_2 values for FK Com during *individual* segments. The subsequent analysis gives the *long-term* P_1 and P_2 values for the two long-lived structures on the surface of FK Com (Eqs. 71 and 72).
- *5th question:* The Kuiper method detects the non-stationary active longitude period P_{act} of the JHL-argument from the seasonal $t_{\text{min},1}$ light curve minima

of chromospherically active binary stars (Jetsu et al. 2017) and single stars (Hackman et al. 2013). Why does this method *not* detect the stationary rotation period $P_{\text{rot}} \approx P_{\text{orb}}$ of the JHL-argument? The long-term mean light curves of chromospherically active binary stars in Jetsu et al. (2017) follow the stationary rotation period $P_{\text{rot}} \approx P_{\text{orb}}$ of the JHL-argument. Why do these long-term mean light curves *not* follow the non-stationary active longitude period P_{act} of the JHL-argument?

Answer: If the $t_{\text{min},1}$ light curve minimum epochs are determined with any one-dimensional period finding method, the Kuiper method analysis of these epochs does not detect only the non-stationary active longitude period P_{act} . The detected periodicity can be $[(f_1 + f_2)/2]^{-1}$, f_2^{-1} or f_1^{-1} of the 2P-model. These periods induce the three migration alternatives, the MIGRATION₁ ($A_1 \approx A_2$), the MIGRATION₂ ($A_1 < A_2$) or the MIGRATION₃ ($A_1 > A_2$), which are defined in Sect. 7.7. The period detected with the Kuiper method may not even be connected to any of the above three alternatives, because the A_1 and A_2 amplitudes of the two real light curves change during the long-term photometry of chromospherically active stars. FK Com has two long-term mean light curves. One follows P_1 and one follows P_2 (Figs. 12 and 13). As for the long-term mean light curves of chromospherically active binaries, the presence of stationary rotation period $P_{\text{rot}} \approx P_{\text{orb}}$ was confirmed in Jetsu et al. (2017), but the non-stationary active longitude period P_{act} needs to be measured more accurately in the future.

- *6th question:* What explains the observed *abrupt* flip-flop events in the chromospherically active stars, if the long-lived starspots rotate with the two *regular constant* periods, the non-stationary active longitude period P_{act} and the stationary rotation period $P_{\text{rot}} \approx P_{\text{orb}}$?
- *Answer:* The 2P-model explains the flip-flop. The *interference* of the two *real* light curves causes these events, e.g. the abrupt phase shift is $\Delta\phi_b = 0.5$, if these two real light curves are equal amplitude $A_1 = A_2$ sinusoids having constant periods P_1 and P_2 (Eq. 48).

These results have numerous consequences.

As predicted by the JHL-argument, the comparison between the 1P-model and the 2P-model with the statistical criterion of Eq. 16 confirms that the latter is certainly a better model for the light curves of FK Com (Sects. 11 and 16.1).

The two long-lived structures predicted by the JHL-argument, which rotate with the constant periods of Eqs. 71 and 72, are present on the surface of FK Com (Sect. 16.2). These structures cause the two observed long-term MLC (Figs. 12 and 13). Since the starspots on the surface of FK Com are not so ephemeral as was previously believed, no sophisticated physical models are needed. For example, the real light curves of FK Com could now be explained with one large long-lived magnetic loop, if the starspots at the feet of this loop rotate with different angular velocities (Sect. 16.3).

The JHL-argument predicts the SI-method detections of long-lived starspots rotating with the constant P_{act} or $P_{\text{rot}} \approx P_{\text{orb}}$ periods (e.g. Berdyugina et al. 1998; Korhonen et al. 2000). It also reveals the map-incompatibility effect that misleads the comparison of two surface images after time intervals longer than $P_{\text{lap}}/2$ (Sect. 16.4).

All earlier activity cycle detections in the periods, the amplitudes and the minima determined with the one-dimensional period finding techniques are spurious (Sect. 16.5.5). Many ideas based on these spurious activity cycle detections need to be revised, like the stellar Rieger cycles (Massi 2007; Distefano et al. 2017), or the connections between these spurious cycle periods and the starspots in general (Jetsu et al. 1990; Berdyugina et al. 2002; Ferreira Lopes et al. 2015; Karmakar et al. 2016; Lehtinen et al. 2016; Reinhold et al. 2017). For example, the rejection of these spurious P_{cyc} cycles may, or may not, help to confirm the existence of separate $P_{\text{rot}}/P_{\text{cyc}}$ branches (e.g. Brandenburg et al. 1998; Saar & Brandenburg 1999; Lorente & Montesinos 2005; Böhm-Vitense 2007; Oláh et al. 2009; Lehtinen et al. 2016).

All earlier physical and geometrical interpretations of the abrupt flip-flop events or the flip-flop cycles are no longer valid (e.g. Jetsu et al. 1991, 1993; Berdyugina & Tuominen 1998; Moss 2004; Fluri & Berdyugina 2004; Elstner & Korhonen 2005; Korhonen & Elstner 2005; Savanov & Strassmeier 2008; Pipin & Kosovichev 2015; Wang et al. 2015; Viviani et al. 2017; Luo et al. 2017). Something that does not happen has been successfully explained, but unfortunately this apparently dramatic phenomenon is merely interference of the two real light curves of CABSSs and CASSs (Sect. 16.5.6).

The formation, the migration and the decay of short-lived starspots, as well as the active longitudes, are spurious phenomena (Sect. 16.5.7). This explains the earlier contradicting starspot life-time estimates (e.g. Hall & Busby 1990; Hall & Henry 1994; Strassmeier et al. 1994; Hussain 2002; Strassmeier 2009; Bertello et al. 2012; Bradshaw & Hartigan 2014; Basri & Nguyen 2018).

The one-dimensional period finding methods, like the LS-method, fail to detect the two real P_1 and P_2 periods in the light curves of CABSSs and CASSs. The pre-whitening approach may sometimes recover these two periods, but only if the $|P_1 - P_2|$ difference is large (Sect. 16.5.8). When the one-dimensional period finding methods are used to study the light curves of CABSSs and CASSs, the results tell nothing about the real physical phenomena. Due to incompatibility, this approach resembles the forcing a square through a circle. The only reliable estimate is that obtained for the mean brightness, just like the centres of a square and a circle do coincide, but the rest makes no sense.

Our hammering of the earlier overwhelming observational evidence for stellar SDR culminates in Sect. 16.7, where we explain why our 2P-model is a better mathematical and physical model than the simple sinusoidal LS-model. Our model requires no short-term changes in the starspots. The slow changes in their relative positions suffice. This result needs to be incorporated into the theories of stellar SDR (e.g. Karak et al. 2015; Brun & Browning 2017; Viviani et al. 2017; Strugarek et al. 2018). For example, it may be that *if, and only if*, the long-lived starspots rotate at *different* latitudes and *stay* at these latitudes, *then* their constant $|P_1 - P_2|$ period difference could still measure stellar SDR.

We present an analogy of incompatibility, because for seven decades these “creatures” have managed to evade detection behind the “veil” of interference. Imagine a face with a left and a right eye. Both eyes can disappear and reappear. At any given moment, the number of eyes may be zero, one or two. The original stationary right eye can

disappear and reappear only at fixed locations. The original non-stationary left eye rotates slowly around the head. We see this head spinning. Soon it is impossible to tell which eye is the original left or right eye (Sect. 7.4.4: map-incompatibility after $P_{\text{lap}}/2$). The only compatible pictures of this face are snapshots, but none of these snapshots can be used to recognize this constantly changing face. These snapshots can capture only one side of the head, or equivalently only half of the full visible surface of FK Com.

The JHL-argument neatly explains many phenomena:

- Spurious *observed* rapid light curve changes
- Spurious short starspot life-times
- Spurious rapid photometric rotation period changes
- Spurious active longitudes
- Spurious starspot migration
- Spurious cycles in periods, amplitudes and minima
- SI-method and LC-method discrepancies for SDR
- Spurious flip-flop events
- Long-term MLC

From our answers to the *1st question*, the *2nd question* and the *3rd question*, we can draw the conclusion that the past overwhelming observational evidence for stellar SDR (e.g. Strassmeier 2009, Sect. 7) has vanished into thin air, or at least all evidence obtained with the one-dimensional period finding methods is inadmissible. Our new period finding method enables us to give *qualitative* and *quantitative* answers to the *4th question* and the *5th question*. It took a quarter of a century to find this short and correct answer to the *6th question*: “Farewell flip-flop.”

Acknowledgements. We thank Thomas Hackman and Ilana Hilesmaa for their comments of this manuscript. This work has made use of NASA’s Astrophysics Data System (ADS) services.

References

- Aigrain, S., Llama, J., Ceillier, T., et al. 2015, MNRAS, 450, 3211
- Alekseev, I. Y. & Kozhevnikova, A. V. 2018, Astronomy Reports, 62, 396
- Arkhipov, O. V., Khodachenko, M. L., Lammer, H., et al. 2015, ApJ, 807, 109
- Ayres, T. R., Kashyap, V., Saar, S., et al. 2016, ApJS, 223, 5
- Bai, T. 2003, ApJ, 591, 406
- Bai, T. & Sturrock, P. A. 1993, ApJ, 409, 476
- Ballester, J. L., Oliver, R., & Carbonell, M. 2002, ApJ, 566, 505
- Balona, L. A. & Abedigamba, O. P. 2016, MNRAS, 461, 497
- Balthasar, H. 2007, A&A, 471, 281
- Barnes, J. R., Collier Cameron, A., Donati, J.-F., et al. 2005, MNRAS, 357, L1
- Basri, G. & Nguyen, H. T. 2018, ArXiv e-prints
- Berdugina, S. V. 2007, Mem. Soc. Astron. Italiana, 78, 242
- Berdugina, S. V., Berdugin, A. V., Ilyin, I., & Tuominen, I. 1998, A&A, 340, 437
- Berdugina, S. V., Moss, D., Sokoloff, D., & Usoskin, I. G. 2006, A&A, 445, 703
- Berdugina, S. V., Pelt, J., & Tuominen, I. 2002, A&A, 394, 505
- Berdugina, S. V. & Tuominen, I. 1998, A&A, 336, L25
- Berdugina, S. V. & Usoskin, I. G. 2003, A&A, 405, 1121
- Bertello, L., Pevtsov, A. A., & Pietarila, A. 2012, ApJ, 761, 11
- Böhm-Vitense, E. 2007, ApJ, 657, 486
- Bonomo, A. S. & Lanza, A. F. 2012, A&A, 547, A37
- Bopp, B. W. & Stencel, R. E. 1981, ApJ, 247, L131
- Bradshaw, S. J. & Hartigan, P. 2014, ApJ, 795, 79
- Brandenburg, A. 2018, ArXiv e-prints
- Brandenburg, A., Mathur, S., & Metcalfe, T. S. 2017, ApJ, 845, 79
- Brandenburg, A., Saar, S. H., & Turpin, C. R. 1998, ApJ, 498, L51
- Brun, A. S. & Browning, M. K. 2017, Living Reviews in Solar Physics, 14, 4
- Chugainov, P. F. 1966, Information Bulletin on Variable Stars, 172
- Cohen, O., Drake, J. J., Kashyap, V. L., et al. 2010, ApJ, 719, 299
- Cole, E., Käpylä, P. J., Mantere, M. J., & Brandenburg, A. 2014, ApJ, 780, L22
- Cole, E. M., Hackman, T., Käpylä, M. J., et al. 2015, A&A, 581, A69
- Collier Cameron, A. 2007, Astronomische Nachrichten, 328, 1030
- Distefano, E., Lanzafame, A. C., Lanza, A. F., Messina, S., & Spada, F. 2016, A&A, 591, A43
- Distefano, E., Lanzafame, A. C., Lanza, A. F., Messina, S., & Spada, F. 2017, A&A, 606, A58
- Drake, J. J., Chung, S. M., Kashyap, V., et al. 2008, ApJ, 679, 1522
- Draper, N. R. & Smith, H. 1998, Applied Regression Analysis (John Wiley & Sons, Inc.)
- Efron, B. & Tibshirani, R. 1986, Stati. Sci., 1, 54
- EGgen, O. J. & Iben, Jr., I. 1989, AJ, 97, 431
- Elstner, D. & Korhonen, H. 2005, Astronomische Nachrichten, 326, 278
- Fabbian, D., Simoniello, R., Collet, R., et al. 2017, Astronomische Nachrichten, 338, 753
- Ferreira Lopes, C. E., Leão, I. C., de Freitas, D. B., et al. 2015, A&A, 583, A134
- Flores Soriano, M. & Strassmeier, K. G. 2017, A&A, 597, A101
- Fluri, D. M. & Berdyugina, S. V. 2004, Sol. Phys., 224, 153
- Giles, H. A. C., Collier Cameron, A., & Haywood, R. D. 2017, MNRAS, 472, 1618
- Gyenge, N., Baranyi, T., & Ludmány, A. 2014, Sol. Phys., 289, 579
- Hackman, T. 2004, PhD thesis, University of Helsinki, Finland
- Hackman, T., Pelt, J., Mantere, M. J., et al. 2013, A&A, 553, A40
- Hale, G. E. 1908, ApJ, 28, 315
- Hall, D. S. 1991, in Lecture Notes in Physics, Berlin Springer Verlag, Vol. 380, IAU Colloq. 130: The Sun and Cool Stars. Activity, Magnetism, Dynamos, ed. I. Tuominen, D. Moss, & G. Rüdiger, 353
- Hall, D. S. & Busby, M. R. 1990, in NATO Advanced Science Institutes (ASI) Series C, Vol. 319, 377
- Hall, D. S. & Henry, G. W. 1994, International Amateur-Professional Photoelectric Photometry Communications, 55, 51
- Hatzes, A. P. 2013, ApJ, 770, 133
- Henry, G. W. 1995, in Astronomical Society of the Pacific Conference Series, Vol. 79, Robotic Telescopes. Current Capabilities, Present Developments, and Future Prospects for Automated Astronomy, ed. G. W. Henry & J. A. Eaton, 44
- Howard, R. F. 1994, in Astronomical Society of the Pacific Conference Series, Vol. 68, Solar Active Region Evolution: Comparing Models with Observations, ed. K. S. Balasubramaniam & G. W. Simon, 1
- Howell, S. B., Mason, E., Boyd, P., Smith, K. L., & Gelino, D. M. 2016, ApJ, 831, 27
- Hussain, G. A. J. 2002, Astronomische Nachrichten, 323, 349
- Jetsu, L. 1996, A&A, 314, 153
- Jetsu, L., Hackman, T., Hall, D. S., et al. 2000, A&A, 362, 223
- Jetsu, L., Henry, G. W., & Lehtinen, J. 2017, ApJ, 838, 122
- Jetsu, L., Huovelin, J., Tuominen, I., et al. 1990, A&A, 236, 423
- Jetsu, L., Kokko, M., & Tuominen, I. 1992, A&A, 265, 547
- Jetsu, L. & Pelt, J. 1996, A&AS, 118, 587
- Jetsu, L. & Pelt, J. 1999, A&AS, 139, 629
- Jetsu, L., Pelt, J., & Tuominen, I. 1993, A&A, 278, 449
- Jetsu, L., Pelt, J., & Tuominen, I. 1999, A&A, 351, 212
- Jetsu, L., Pelt, J., Tuominen, I., & Nations, H. 1991, in Lecture Notes in Physics, Berlin Springer Verlag, Vol. 380, IAU Colloq. 130: The Sun and Cool Stars. Activity, Magnetism, Dynamos, ed. I. Tuominen, D. Moss, & G. Rüdiger, 381
- Jetsu, L., Pohjolainen, S., Pelt, J., & Tuominen, I. 1997, A&A, 318, 293
- Jetsu, L. & Porceddu, S. 2015, PLoS ONE, 10(12), e0144140
- Jetsu, L., Porceddu, S., Lyytinen, J., et al. 2013, ApJ, 773, 1
- Jetsu, L., Tuominen, I., Grankin, K. N., Mel’Nikov, S. Y., & Schevchenko, V. S. 1994, A&A, 282, L9
- Kaltenbacher, B., Neubauer, A., & Scherzer, O. 2008, Iterative Regularization Methods for Nonlinear Ill-Posed Problems, Radon Series on Computational and Applied Mathematics (De Gruyter)
- Käpylä, P. J., Mantere, M. J., & Hackman, T. 2011, ApJ, 742, 34
- Karak, B. B., Käpylä, P. J., Käpylä, M. J., et al. 2015, A&A, 576, A26
- Karmakar, S., Pandey, J. C., Savanov, I. S., et al. 2016, MNRAS, 459, 3112
- Kövári, Z., Oláh, K., Kriskovics, L., et al. 2017, Astronomische Nachrichten, 338, 903
- Kochukhov, O. 2016, in Lecture Notes in Physics, Berlin Springer Verlag, Vol. 914, Lecture Notes in Physics, Berlin Springer Verlag,

- ed. J.-P. Rozelot & C. Neiner, 177
- Korhonen, H., Berdyugina, S. V., Hackman, T., et al. 1999, *A&A*, 346, 101
- Korhonen, H., Berdyugina, S. V., Hackman, T., et al. 2007, *A&A*, 476, 881
- Korhonen, H., Berdyugina, S. V., Hackman, T., Strassmeier, K. G., & Tuominen, I. 2000, *A&A*, 360, 1067
- Korhonen, H., Berdyugina, S. V., Ilyin, I. V., Strassmeier, K. G., & Hackman, T. 2009, in *Revista Mexicana de Astronomia y Astrofisica*, vol. 27, Vol. 36, *Revista Mexicana de Astronomia y Astrofisica Conference Series*, CD323–CD327
- Korhonen, H., Berdyugina, S. V., Strassmeier, K. G., & Tuominen, I. 2001a, *A&A*, 379, L30
- Korhonen, H., Berdyugina, S. V., & Tuominen, I. 2002, *A&A*, 390, 179
- Korhonen, H., Berdyugina, S. V., & Tuominen, I. 2004, *Astronomische Nachrichten*, 325, 402
- Korhonen, H., Berdyugina, S. V., Tuominen, I., et al. 2001b, *A&A*, 374, 1049
- Korhonen, H. & Elstner, D. 2005, *A&A*, 440, 1161
- Korhonen, H. & Elstner, D. 2011, *A&A*, 532, A106
- Kóspál, Á., Ábrahám, P., Zsidi, G., et al. 2018, *ArXiv e-prints*
- Kraus, M., Haucke, M., Cidale, L. S., et al. 2015, *A&A*, 581, A75
- Kron, G. E. 1947, *PASP*, 59, 261
- Lanza, A. F., Pagano, I., Leto, G., et al. 2009, *A&A*, 493, 193
- Lanzafame, A. C., Distefano, E., Messina, S., et al. 2018, *ArXiv e-prints*
- Lean, J. 1990, *ApJ*, 363, 718
- Lehtinen, J., Jetsu, L., Hackman, T., Kajatkari, P., & Henry, G. W. 2011, *A&A*, 527, A136
- Lehtinen, J., Jetsu, L., Hackman, T., Kajatkari, P., & Henry, G. W. 2012, *A&A*, 542, A38
- Lehtinen, J., Jetsu, L., Hackman, T., Kajatkari, P., & Henry, G. W. 2016, *A&A*, 588, A38
- Lindborg, M., Korpi, M. J., Hackman, T., et al. 2011, *A&A*, 526, A44
- Lomb, N. R. 1976, *Ap&SS*, 39, 447
- Lorente, R. & Montesinos, B. 2005, *ApJ*, 632, 1104
- Loumos, G. L. & Deeming, T. J. 1978, *Ap&SS*, 56, 285
- Luo, X., Wang, K., Zhang, X., et al. 2017, *AJ*, 154, 99
- Mantere, M. J., Käpylä, P. J., & Hackman, T. 2011, *Astronomische Nachrichten*, 332, 876
- Mantere, M. J., Käpylä, P. J., & Pelt, J. 2013, in *IAU Symposium*, Vol. 294, *Solar and Astrophysical Dynamos and Magnetic Activity*, ed. A. G. Kosovichev, E. de Gouveia Dal Pino, & Y. Yan, 175–186
- Massi, M. 2007, *Mem. Soc. Astron. Italiana*, 78, 247
- Mennickent, R. E. 2017, *Serbian Astronomical Journal*, 194, 1
- Moss, D. 1999, *MNRAS*, 306, 300
- Moss, D. 2004, *MNRAS*, 352, L17
- Moss, D., Barker, D. M., Brandenburg, A., & Tuominen, I. 1995, *A&A*, 294, 155
- Moss, D. & Tuominen, I. 1997, *A&A*, 321, 151
- Nielsen, M. B., Schunker, H., Gizon, L., Schou, J., & Ball, W. H. 2017, *A&A*, 603, A6
- Oláh, K., Kolláth, Z., Granzer, T., et al. 2009, *A&A*, 501, 703
- Oláh, K., Korhonen, H., Kóvári, Z., Forgács-Dajka, E., & Strassmeier, K. G. 2006, *A&A*, 452, 303
- Oliver, R., Ballester, J. L., & Baudin, F. 1998, *Nature*, 394, 552
- Olsper, N., Lehtinen, J. J., Käpylä, M. J., Pelt, J., & Grigorievskiy, A. 2017, *ArXiv e-prints*
- Özavcı, I., Şenavcı, H. V., Işık, E., et al. 2018, *MNRAS*, 474, 5534
- Panov, K. & Dimitrov, D. 2007, *A&A*, 467, 229
- Pelt, J., Tuominen, I., & Brooke, J. 2005, *A&A*, 429, 1093
- Peterson, W. M., Mutel, R. L., Güdel, M., & Goss, W. M. 2010, *Nature*, 463, 207
- Petit, P., Donati, J.-F., Oliveira, J. M., et al. 2004, *MNRAS*, 351, 826
- Pipin, V. V. & Kosovichev, A. G. 2015, *ApJ*, 813, 134
- Porceddu, S., Jetsu, L., Markkanen, T., et al. 2018, *Open Astronomy*, in press
- Porceddu, S., Jetsu, L., Markkanen, T., & Toivari-Viitala, J. 2008, *Cambridge Archaeological Journal*, 18, 327
- Puzin, V. B., Savanov, I. S., & Dmitrienko, E. S. 2014, *Astronomy Reports*, 58, 471
- Puzin, V. B., Savanov, I. S., & Dmitrienko, E. S. 2017, *Astronomy Reports*, 61, 693
- Queloz, D., Bouchy, F., Moutou, C., et al. 2009, *A&A*, 506, 303
- Radick, R. R., Lockwood, G. W., Henry, G. W., Hall, J. C., & Pevtsov, A. A. 2018, *ApJ*, 855, 75
- Reinhold, T. & Arlt, R. 2015, *A&A*, 576, A15
- Reinhold, T., Cameron, R. H., & Gizon, L. 2017, *A&A*, 603, A52
- Reinhold, T. & Gizon, L. 2015, *A&A*, 583, A65
- Reinhold, T. & Reiners, A. 2013, *A&A*, 557, A11
- Reinhold, T., Reiners, A., & Basri, G. 2013, *A&A*, 560, A4
- Reyniers, M., Degroote, P., Bodewits, D., Cuypers, J., & Waelkens, C. 2009, *A&A*, 494, 379
- Rieger, E., Kanbach, G., Reppin, C., et al. 1984, *Nature*, 312, 623
- Roettenbacher, R. M., Monnier, J. D., Korhonen, H., et al. 2016, *Nature*, 533, 217
- Saar, S. H. & Brandenburg, A. 1999, *ApJ*, 524, 295
- Saio, H., Bedding, T. R., Kurtz, D. W., et al. 2018, *MNRAS*, 477, 2183
- Savanov, I. S. & Strassmeier, K. G. 2008, *Astronomische Nachrichten*, 329, 364
- Scargle, J. D. 1982, *ApJ*, 263, 835
- Schwabe, M. 1844, *Astronomische Nachrichten*, 21, 233
- See, V., Jardine, M., Vidotto, A. A., et al. 2016, *MNRAS*, 462, 4442
- Shultz, M. E., Wade, G. A., Rivinius, T., et al. 2018, *MNRAS*, 475, 5144
- Siltala, L., Jetsu, L., Hackman, T., et al. 2017, *Astronomische Nachrichten*, 338, 453
- Snieder, R. 1998, *Inverse Problems*, 14, 387
- Strassmeier, K. G. 2009, *A&A Rev.*, 17, 251
- Strassmeier, K. G. 2011, in *IAU Symposium*, Vol. 273, *Physics of Sun and Star Spots*, ed. D. Prasad Choudhary & K. G. Strassmeier, 174–180
- Strassmeier, K. G. & Bartus, J. 2000, *A&A*, 354, 537
- Strassmeier, K. G., Boyd, L. J., Epan, D. H., & Granzer, T. 1997, *PASP*, 109, 697
- Strassmeier, K. G., Hall, D. S., & Henry, G. W. 1994, *A&A*, 282, 535
- Strugarek, A., Beaudoin, P., Charbonneau, P., & Brun, A. S. 2018, *ArXiv e-prints*
- Tarantola, A. & Valette, B. 1982, *Reviews of Geophysics and Space Physics*, 20, 219
- Tuominen, I., Berdyugina, S. V., & Korpi, M. J. 2002, *Astronomische Nachrichten*, 323, 367
- Tuominen, I., Pelt, J., Brooke, J., Korpi, M., & Ostwriter, G. H. 2007, *Astronomische Nachrichten*, 328, 1020
- Van Helden, A. 1996, *Proc. Am. Phil. Soc.*, 140, 358
- Vernova, E. S., Tyasto, M. I., & Baranov, D. G. 2007, *Sol. Phys.*, 245, 177
- Vida, K., Korhonen, H., Ilyin, I. V., et al. 2015, *A&A*, 580, A64
- Viviani, M., Warnecke, J., Käpylä, M. J., et al. 2017, *ArXiv e-prints*
- Wang, K., Zhang, X., Deng, L., et al. 2015, *ApJ*, 805, 22
- Wargelin, B. J., Saar, S. H., Pojmański, G., Drake, J. J., & Kashyap, V. L. 2017, *MNRAS*, 464, 3281
- Warnecke, J. 2017, *ArXiv e-prints*
- Washuettl, A., Strassmeier, K. G., & Weber, M. 2009, *Astronomische Nachrichten*, 330, 366
- Webbink, R. F. 1976, *ApJ*, 209, 829
- Welty, A. D. & Ramsey, L. W. 1994, *ApJ*, 435, 848
- Willson, R. C. & Hudson, H. S. 1991, *Nature*, 351, 42

Appendix A: Notes of individual segments

In this Appendix, we discuss the period analysis results of each individual segment, except for those of DATA_{2,1} which were already discussed in Sect. 9. For each segment, the information given in Tables 6-11 requires one page in this Appendix, which contains the descriptive text and the three different figures. This tedious detailed discussion can not be avoided, because the interpretation of our two-dimensional period analysis results is far from trivial. Note that we change the page when all results for any particular segment have been described. In this way, our appendix is easier to read, because all figures connected to any particular segment are on the same page as the descriptive text.

A.1. DATA_{2,2}

The $z_C(f_1, f_2)$ periodogram shows a cross shape and white arms (Fig. A.1). The $\pm f_0/2$ and $\pm 3\sigma_{f_1, f_2}$ limits hit $f_1 = f_2$. The frequency level of the best period P_3 of the 1P-model fits perfectly to the positions of the white arms. Note that there are two cases where the best model for a bootstrap is outside the red circle of Eq. 57 (Fig. A.1: two red “x” symbols, Table 6: bootstrap outside $\pm f_0/2$ = “Yes”). The best solution for the $g_C(t)$ model is so close to the $f_1 = f_2$ diagonal line that amplitude dispersion takes place. This 2P-model clearly breaks down (Table 6: 2P-model breaks down = “CASE₁”). We conclude that the 1P-model is both the conservative and the liberal model for DATA_{2,2}.

The original data y_i show that the amplitude of the light curve of FK Com decreases, but its mean remains about the same during $\Delta T = 224.^d6$ (Fig. A.2a). The second order polynomial h_i of Eq. 1 can reproduce these minor changes of the mean. The $z_C(t)$ model can follow the amplitude changes of y_i^i (Fig. A.2b). The residuals of this model reach $z_{C, \min} = 0.^m016$, and display no regular variation (Fig. A.2c). However, the $g_1(t)$ and $g_2(t)$ light curves suffer from amplitude dispersion, and make no sense (Figs. A.2edf).

The 1P-model gives the best period $P_3 = 2.^d4064 \pm 0.^d0005$ for these data (Fig. A.3a). The amplitude of the light curve is high, $A_3 = 0.^m140 \pm 0.^m003$. Note that these numerical P_3 and A_3 values are practically the same as for DATA_{2,1} of the previous year (Tables 7 and 9). The best period determined with the LS-method is nearly equal to P_3 (Fig. A.3b: red and blue vertical lines). The 1P-model can not follow the changing amplitude of the light curve of FK Com during about seven months (Fig. A.3c). This effect is also seen in the model residuals, especially in the beginning of the data (Fig. A.3d). Nevertheless, the mean residuals $z_{S, \min}$ of the 1P-model are only $0.^m0026$ larger than in the 2P-model (Fig. A.1). The $g_S(\phi_3)$ phase plot shows only one minimum (Fig. A.3e).

Since the conservative and the liberal model are the same, the results given in Tables 7-8 and 9-10 are also the same. No simultaneous TEL=1 observations are available to check these results for DATA_{2,2}.

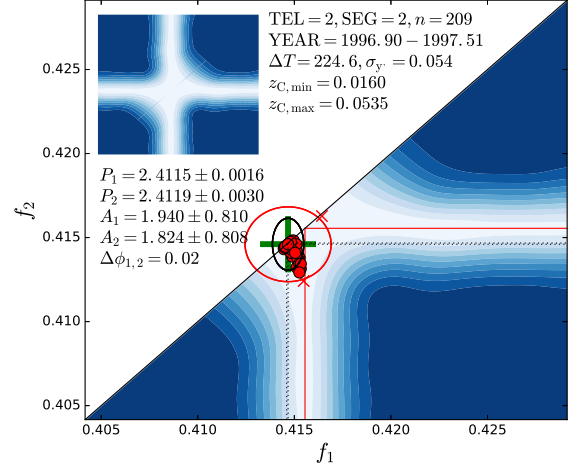


Fig. A.1. DATA_{2,2}. Otherwise as in Fig. 6

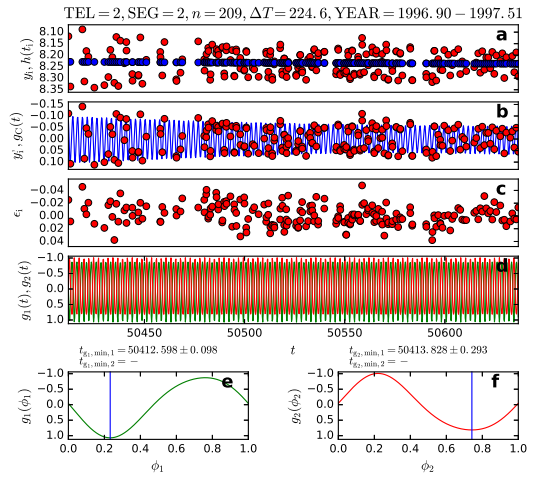


Fig. A.2. DATA_{2,2}. Otherwise as in Fig. 7

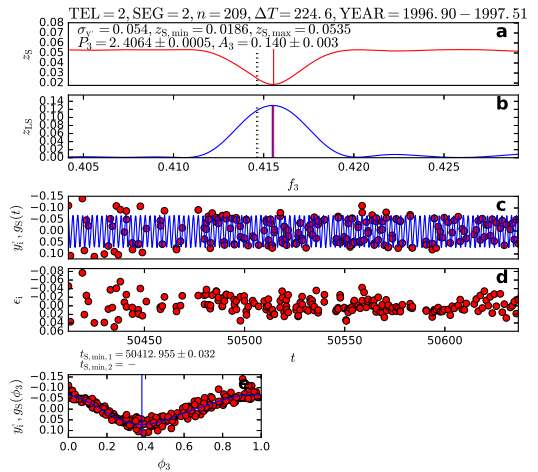


Fig. A.3. DATA_{2,2}. Otherwise as in Fig. 8

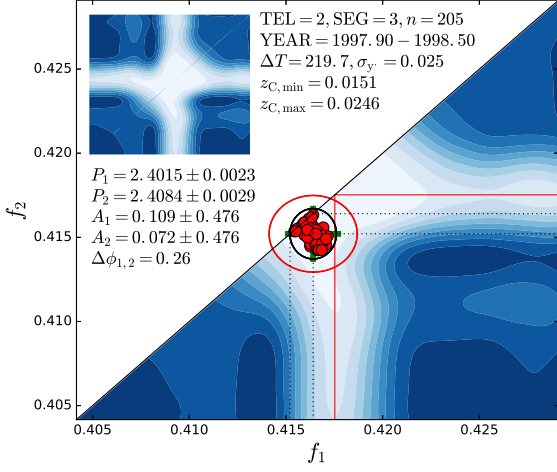


Fig. A.4. DATA_{2,3}. Otherwise as in Fig. 6

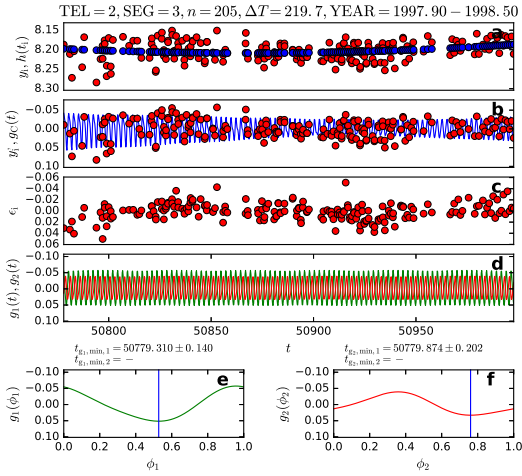


Fig. A.5. DATA_{2,3}. Otherwise as in Fig. 7

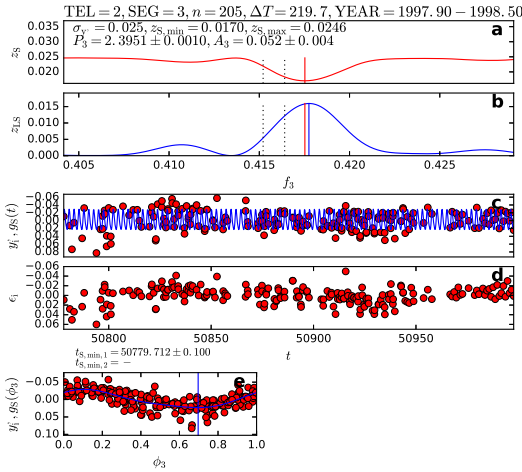


Fig. A.6. DATA_{2,3}. Otherwise as in Fig. 8

A.2. DATA_{2,3}

A cross shape is present in the $z_C(f_1, f_2)$ periodogram of Fig. A.4. However, the arms of this cross become a bit blue closer to the right and the lower edge of the large blue-white triangle. The continuous vertical and horizontal red lines denoting the frequency level $1/P_3$ of the 1P-model best period coincide with the locations of these arms. The $\pm f_0/2$ and the $\pm 3\sigma_{f_1, f_2}$ limits hit the diagonal line $f_1 = f_2$. Amplitude dispersion takes place because the best $g_C(t)$ model is too close to this diagonal, i.e. the 2P-model breaks down (“CASE₁”). Note that the amplitude dispersion is present only in the σ_{A_1} and σ_{A_2} estimates, but not in the A_1 and A_2 estimates. We conclude that the 1P-model is the conservative and the liberal model.

The amplitude of the light curve of FK Com first decreases, then increases, and again decreases during seven months (Fig. A.5a). The small changes of the mean can be modelled with the second order polynomial h_i (Eq. 1). The best $z_C(t)$ model can more or less reproduce these changes (Fig. A.5b). The residuals of this model have $z_{C,\min} = 0.^m0151$. These residuals do not show large temporal variation (Fig. A.5c), except for the beginning of the data where the polynomial fit h_i may not follow the real mean of the original data (Fig. A.5a).

The 1P-model gives the best period $P_3 = 2.^d3951 \pm 0.^d0010$ (Fig. A.6a: red vertical line). The LS-method result for the best period is nearly the same (Fig. A.6b: blue vertical line). The light curve amplitude is low, $A_3 = 0.^m052 \pm 0.^m004$. This amplitude value is not a very good estimate for these data, because the $g_S(t)$ model can not follow the amplitude changes of y_i during about seven months (Fig. A.6b). The model residuals also display this inconsistency effect (Fig. A.6d). Regardless of all these effects, the $z_{S,\min} - z_{C,\min}$ difference is only $0.^m0019$. Only one minimum is present in the $g_S(\phi_3)$ phase plot (Fig. A.6e).

The same results are given in Tables 7-8 and 9-10, because the conservative and the liberal model for the data of this segment are the same, i.e. the 1P-model. Simultaneous TEL=1 observations are available. This DATA_{1,1} confirms the above P_3 and A_3 estimates, although these TEL=1 observations begin over two months later than DATA_{2,3}.

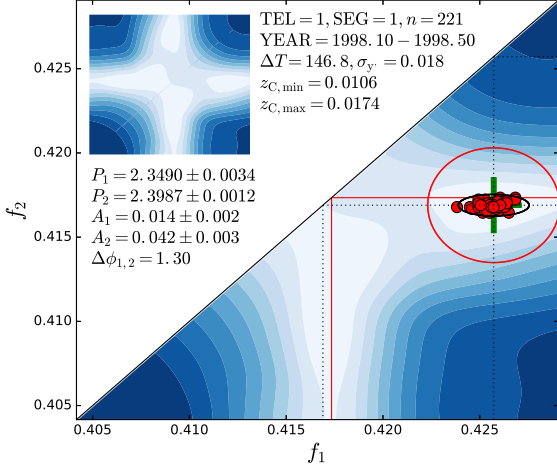


Fig. A.7. DATA_{1,1}. Otherwise as in Fig. 6

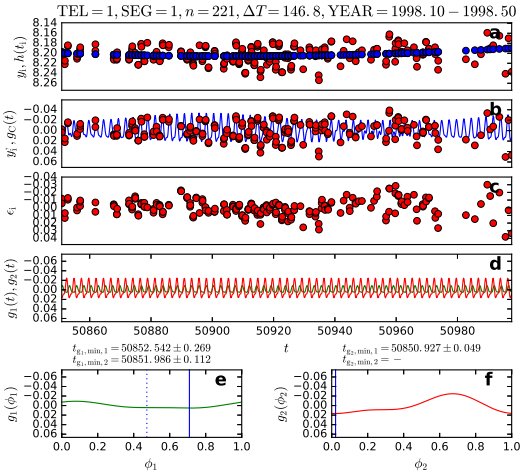


Fig. A.8. DATA_{1,1}. Otherwise as in Fig. 7

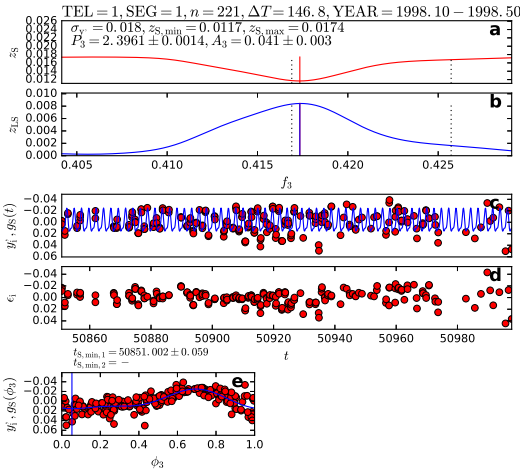


Fig. A.9. DATA_{1,1}. Otherwise as in Fig. 8

A.3. DATA_{1,1}

The $z_C(f_1, f_2)$ periodogram shows a cross shape, not completely white arms and the best model at end of a horizontal arm (Fig. A.7). The amplitude $A_1 = 0.^m014 \pm 0.^m002$ of the weaker periodicity $P_1 = 2.^d3490 \pm 0.^d0034$ is only $0.^m0034$ larger than the $z_{C,\min} = 0.^m0106$ value. This is the weakest signal in Tables 7 and 9. Its signal to noise ratio is close to one ($A_1/z_{C,\min} = 1.3$). The weakness of this signal, together with the high amplitude ratio $R_A = A_2/A_1 = 3$ (Eq. 59), indicates that here we encounter our first CASE₂ (Eq. 11). In other words, the stronger periodicity $P_2 = 2.^d3987 \pm 0.^d0012$ dominates the $g_C(t)$ solution, although the amplitude of this other signal is also very low $A_2 = 0.^m042 \pm 0.^m003$. Hence, the 2P-model breaks down (Table 6: 2P-model breaks down="CASE₂"). The locations of the cross shape and the red lines denoting the frequency level $1/P_3$ of the 1P-model best period are nearly identical. In fact, the $P_2 - P_3 = 0.^d0026 \pm 0.^d0018$ and $A_2 - A_3 = 0.^m001 \pm 0.^m004$ differences are so small that our final results given in Tables 7 and 9 would be nearly the same for the 2P-model or the 1P-model. The $\pm f_0/2$ and $\pm 3\sigma_{f_1, f_2}$ limits do not hit $f_1 = f_2$. In this segment, the 1P-model is the conservative model and the 2P-model is the liberal model.

Except for the first two missing months, the earlier light curve of FK Com from Fig. A.5a is seen again in Fig. A.8a. All changes of the mean can not be reproduced by the second order polynomial h_i of Eq. 1. The $z_C(t)$ model can more or less follow the y_i amplitude changes (Fig. A.8b). The residuals are small, $z_{C,\min} = 0.^m0106$, but they increase towards the end of the data (Fig. A.8c). The $g_1(t)$ and $g_2(t)$ light curves are shown in Figs. A.8edf. Note that the green low amplitude $g_1(t)$ curve in Fig. A.8e has two minima.

The 1P-method and the LS-method give exactly the same best periods (Fig. A.9ab: red and blue vertical lines). These periods are close to the stronger P_2 periodicity, and it is no surprise these two methods detect no signs of the weaker P_1 periodicity. The $g_S(t)$ light curve has a low amplitude of $0.^m041 \pm 0.^m003$ (Fig. A.9c). It can approximately reproduce the y_i changes, except for the end of these data where the residuals increase (Fig. A.9d). The 1P-model and the 2P-model have nearly the same level of residuals because the difference $z_{S,\min} - z_{C,\min} = 0.^m0011$ is negligible. The $g_S(\phi_3)$ phase plot shows only one minimum (Fig. A.9e).

The results in Tables 7-8 and 9-10 are different, because the conservative and the liberal models are different. As already noted, the temporally overlapping DATA_{2,3} confirms the above P_3 and A_3 estimates.

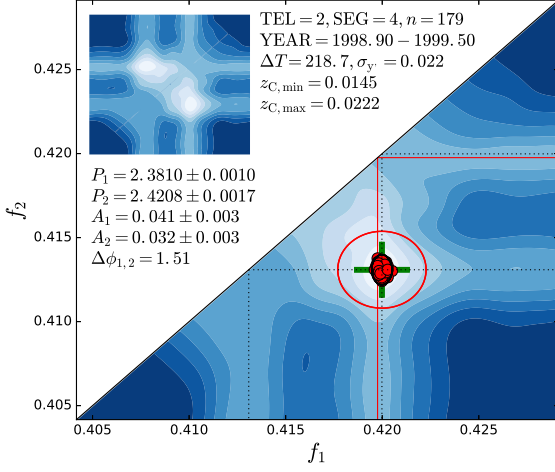


Fig. A.10. DATA_{2,4}. Otherwise as in Fig. 6

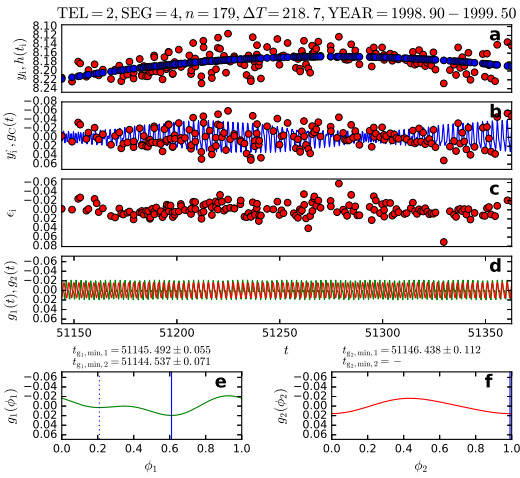


Fig. A.11. DATA_{2,4}. Otherwise as in Fig. 7

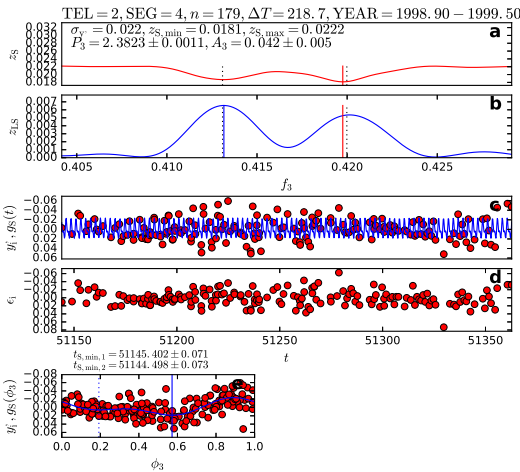


Fig. A.12. DATA_{2,4}. Otherwise as in Fig. 8

A.4. DATA_{2,4}

No cross shape and no white arms are seen in the $z_C(f_1, f_2)$ periodogram of Fig. A.10. The best $g_C(t)$ solution is so far from the $f_1 = f_2$ diagonal line that the CASE₁ break down of the 2P-model does not occur. The amplitude ratio $R_A = 1.3$ rules out the CASE₂ and CASE₃ alternatives. These seven months of data represent by far the first clear case where two simultaneous real periods are unambiguously detected with the 2P-method. Since the 2P-model does not break down, this is the first time that we discuss the application of the criterion of Eq. 16. This criterion is fulfilled, because the ratio $R_S/R_C = z_{S,min}^2/z_{C,min}^2$ in Eq. 15 gives $F = 18.8$ reaching an extreme critical level $Q_F = 9 \times 10^{-15}$, i.e. we reject the H_0 hypothesis of Sect. 3.3. The 2P-model is certainly the best model for these data. The residuals reach $z_{C,min} = 0.^m0145$. This is an excellent result considering that we can model about seven months of the constantly changing light curve of FK Com. After all, the accuracy of the data is between $0.^m004$ and $0.^m008$ only during the best photometric nights. The red lines denoting the frequency level $1/P_3$ of the best period of the 1P-model nearly coincide with the dotted lines of $1/P_1$. In this segment, the 2P-model is the conservative and the liberal model.

The original data show that the amplitude and the mean of light curve of FK Com underwent significant changes during $\Delta T = 218.^d7$ (Fig. A.11a). The second order polynomial (Eq. 1: h_i) can more or less follow the changes of the mean brightness. The 2P-model model fits to the y_i data (Fig. A.11b). The residuals are largest in the middle of the observing season and they contain a few large outliers (Fig. A.11c). The red and green continuous lines in Figs. A.11d-f show the low amplitude $g_1(t)$ and $g_2(t)$ light curves. The green $g_1(\phi_1)$ curve has two minima (Fig. A.11e).

The 1P-method and the LS-method periodograms give different best periods (Fig. A.12ab: red and blue vertical lines). However, both of these methods detect the same two best periods. The dotted lines denoting the best periods P_1 and P_2 detected with the 2P-method are very close to the two minima of the 1P-method periodogram and the two maxima of the LS-method periodogram. The difference between P_1 and P_2 is so large that the 1P-method and the LS-method can also detect both of these periods, as already predicted by Loumos & Deeming (1978). The $g_S(t)$ light curve fails to reproduce the y_i changes (Fig. A.12c). The residuals in Fig. A.12d are quite large, because $z_{S,min} = 0.^m018$ is close to $\sigma_y = 0.^m022$. There are two minima in the $g_S(\phi_3)$ curve (Fig. A.12e).

The results for this segment are the same in Tables 7-8 and 9-10, because the conservative and the liberal models are the same. All the above main results for DATA_{2,4} are confirmed by the analysis of the simultaneous DATA_{1,2}, which is presented in the next Sect. A.5.

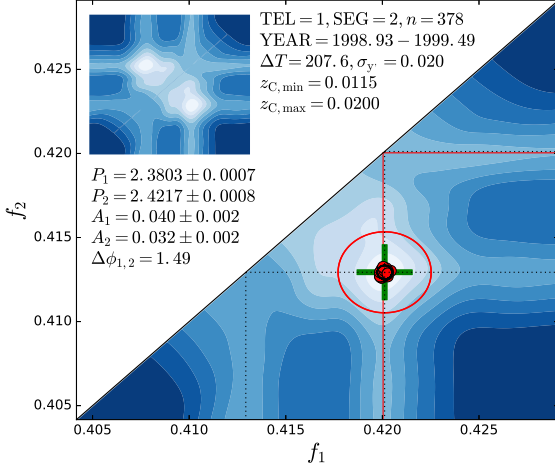


Fig. A.13. DATA_{1,2}. Otherwise as in Fig. 6

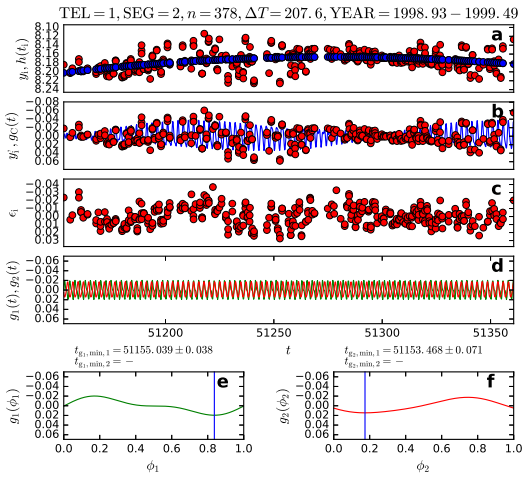


Fig. A.14. DATA_{1,2}. Otherwise as in Fig. 7

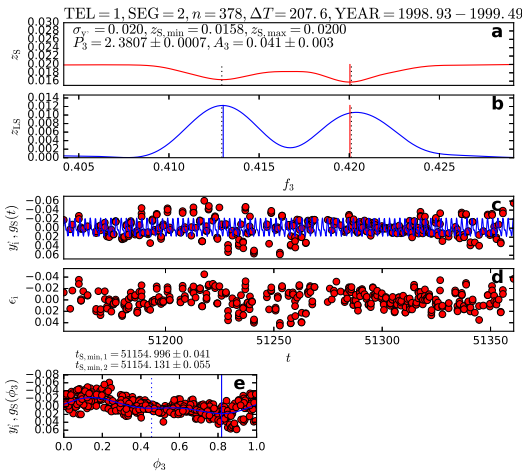


Fig. A.15. DATA_{1,2}. Otherwise as in Fig. 8

A.5. DATA_{1,2}

The cross shape and the white arms are also absent from the $z_C(f_1, f_2)$ periodogram of Fig. A.13. The best $g_C(t)$ solution is so far from the $f_1 = f_2$ diagonal that the CASE₁ alternative break down can be excluded. The amplitude ratio $R_A = 1.3$ excludes also the CASE₂ and CASE₃ alternatives for the 2P-model break down. This is the second time when the 2P-method detects two simultaneous real periods. We can again unambiguously compare the 2P-model to the 1P-model by testing the criterion of Eq. 16. Using $R_S/R_C = z_{S,min}^2/z_{C,min}^2$ in Eq. 15 gives $F = 65.2$. This F value is so improbable that the critical level Q_F goes below our 10^{-16} computational accuracy. This confirms that the 2P-model is the best model for these data. The $z_{C,min} = 0.^m0115$ parameter measuring the residuals is smaller than in the simultaneous DATA_{4,2} in Fig. A.10. As in DATA_{2,4}, the $1/P_3$ red lines coincide with the $1/P_1$ dotted lines. The 2P-model is both the conservative and the liberal model.

The same significant changes of light curve of FK Com that were already seen in Fig. A.11a are displayed again in Fig. A.14a. These changes can be reproduced with the 2P-model (Fig. A.14b). The second order polynomial fit h_i in Fig. A.14a can not follow all changes of the mean in the original data during $\Delta T = 207.^d6$. This causes the regular small amplitude fluctuation of residuals in Fig. A.14c. The low amplitude $g_1(t)$ and $g_2(t)$ light curves are denoted with red and green continuous lines in Figs. A.14def. Both curves have only one minimum.

The 1P-method and the LS-method detect the same two best periods, but the order of significance for these two periods is again different (Fig. A.15ab: red and blue vertical lines). These two best periods are nearly the same as P_1 and P_2 detected with the 2P-method (Fig. A.15ab: dotted lines). In these data, the P_1 and P_2 difference is also so large that the 1P-method and the LS-method can detect both periodicities. This result confirms the $1.5f_0$ detectability limit argument made by Loumos & Deeming (1978). The $g_S(t)$ model does not fit to the y_i data (Fig. A.15c). The residuals in Fig. A.15d reach only $z_{C,min} = 0.^m0158$ which is not much smaller than the standard deviation $\sigma_{y_i} = 0.^m020$ of these data. The $g_S(\phi_3)$ curve in Fig. A.15e shows two minima.

The results for the conservative and the liberal model are the same in Tables 7-8 and 9-10. The temporal overlap of DATA_{2,4} and DATA_{1,2} is perfect, and the 2P-method analysis results are identical (Table 7).

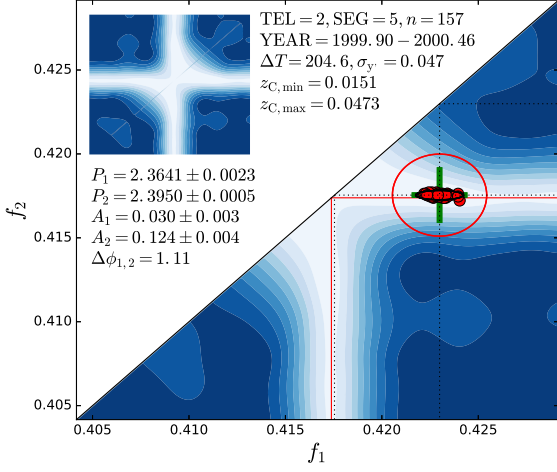


Fig. A.16. DATA_{2,5}. Otherwise as in Fig. 6

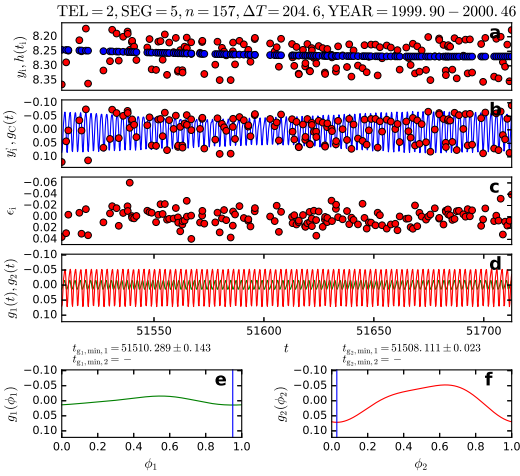


Fig. A.17. DATA_{2,5}. Otherwise as in Fig. 7

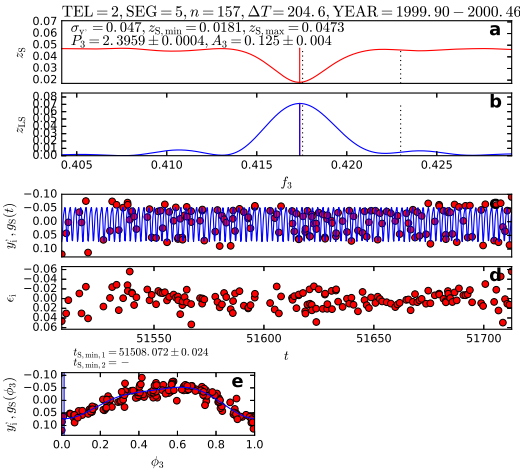


Fig. A.18. DATA_{2,5}. Otherwise as in Fig. 8

A.6. DATA_{2,5}

A cross shape and white arms are present in the $z_C(f_1, f_2)$ periodogram of Fig. A.16. The best $g_C(t)$ model is in the middle of the horizontal white arm. The $z_{C,\min} = 0.^m0151$ level is only two times lower than the amplitude $A_1 = 0.^m030 \pm 0.^m003$ of the weaker periodicity $P_1 = 2.^d3641 \pm 0.^d0023$. The high amplitude ratio $R_A = A_2/A_1 = 4.1$ means that the signal of the stronger periodicity $P_2 = 2.^d3950 \pm 0.^d0005$ dominates. The error ratio, $\sigma_{P_1}/\sigma_{P_2} = 5.4$, indicates that the location of $1/P_1$ on the horizontal $1/P_2$ arm is uncertain (Fig. A.16: black ellipse). The white arms coincide exactly with the red lines denoting the frequency level $1/P_3$ of the 1P-model best period. The small $P_3 - P_2 = 0.^d0009 \pm 0.^d0006$ and $A_3 - A_2 = 0.^m001 \pm 0.^m006$ differences show that our final results given in Tables 7 and 9 would be nearly the same with the 2P-model or the 1P-model. All these details indicate that the 2P-model breaks down takes place (Table 6: 2P-model breaks down="CASE2"). We conclude that the 1P-model is the conservative model and the 2P-model is the liberal model.

The amplitude of the light curve of FK Com first decreases and then increases during $\Delta T = 204.^d6$, and the second order polynomial h_i can easily follow the minor changes of the mean brightness (Fig. A.17a). The $z_C(t)$ model can reproduce these changes (Fig. A.17b). The level and the scatter of the residuals remain are stable (Fig. A.17c). There are few outliers that may be flares. The red $g_2(t)$ light curve clearly dominates over the green $g_1(t)$ light curve (Figs. A.17def).

The best periods detected with the 1P-method and the LS-method are exactly the same, while the stronger period P_2 detected with the 2P-method is nearly the same (Fig. A.18ab: red and blue vertical lines, black dotted vertical lines). The 1P-method and the LS-method detect no signs of the weaker P_1 periodicity. The amplitude of the $g_S(t)$ light curve is high, $0.^m125$ (Fig. A.18c). This model can approximately reproduce the y_i changes, although the residuals increase in the end and the beginning of data (Fig. A.18d). The $g_S(\phi_3)$ curve has only one minimum (Fig. A.18e).

The conservative and the liberal models are different, and therefore the results in Tables 7-8 and 9-10 are different. There are temporally overlapping TEL=1 observations (DATA_{1,3}) and they are discussed in the next Sect. A.3. That analysis confirms all main results presented above.

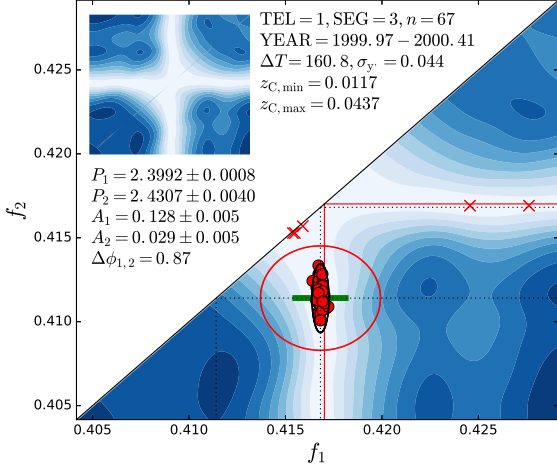


Fig. A.19. DATA_{1,3}. Otherwise as in Fig. 6

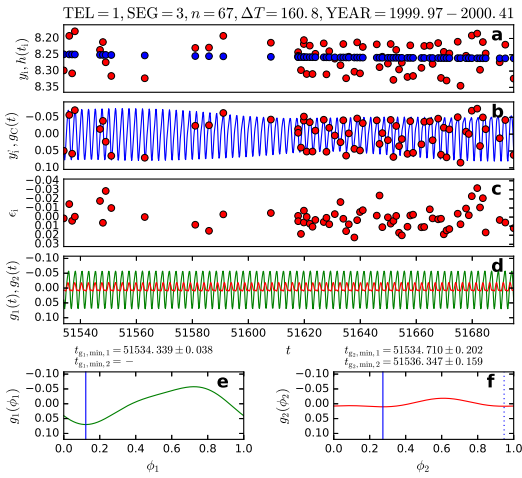


Fig. A.20. DATA_{1,3}. Otherwise as in Fig. 7

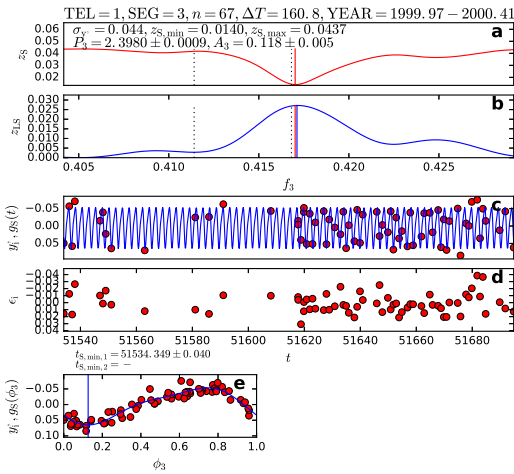


Fig. A.21. DATA_{1,3}. Otherwise as in Fig. 8

A.7. DATA_{1,3}

The $z_C(f_1, f_2)$ periodogram shows a cross shape, white arms and the best $g_C(t)$ model in the middle of the vertical white arm (Fig. A.19). The signal of the weaker periodicity $P_2 = 2.^d4307 \pm 0.^d0040$ has an amplitude $A_2 = 0.^m029 \pm 0.^m005$. The signal of the stronger periodicity $P_1 = 2.^d3992 \pm 0.^d0008$ dominates because the amplitude ratio $R_A = A_1/A_2 = 4.4$ is high. The location of $1/P_2$ on the vertical $1/P_1$ arm is uncertain due to the error ratio $\sigma_{P_2}/\sigma_{P_1} = 5.0$ (Fig. A.19: black ellipse). In this segment, five of the 50 first bootstrap samples yields a solution which is outside the $\pm f_0/2$ circle of Eq. 57 (Fig. A.19: red “x” symbol, Table 6: bootstrap outside $\pm f_0/2$ =”Yes”). It is probably neither a coincidence that the location of two red “x” symbols on the horizontal arm is close to the location of the best model for the partly simultaneous DATA_{2,5} (Fig. A.16: large green cross). The overlap between the white arms and the red lines denoting the frequency level $1/P_3$ of the 1P-model best period is perfect. The differences $P_1 - P_3 = 0.^d0012 \pm 0.^d0012$ and $A_1 - A_3 = 0.^m010 \pm 0.^m007$ are so small that the results in Tables 7 and 9 would be nearly the same with the 2P-model or the 1P-model. We have clearly encountered our first CASE₃ break down of the 2P-model (Table 6: 2P-model breaks down =”CASE₃”). Hence, the 1P-model is the conservative model, while the 2P-model is the liberal model.

This is our smallest analysed sample of data ($n = 68$). The first half of the $\Delta T = 160.^d8$ time span contains only a few observations. The minor changes of the mean brightness can be easily modelled with the second order polynomial h_i (Fig. A.20a). The 2P-model reproduces the small amplitude changes of the y_i data (Fig. A.20b). The level of the residuals is stable, but the scatter increases in the end of the data (Fig. A.20c). Due to CASE₃, the green $g_1(t)$ light curve dominates over the red $g_2(t)$ light curve (Figs. A.20def). The $g_2(\phi_2)$ curve has two minima.

The 1P-method and the LS-method detect nearly the same period. These two periods are close to the stronger P_1 periodicity detected with the 2P-method. (Fig. A.21ab: red and blue vertical lines, black dotted vertical lines). This result is predicted by Eqs. 45 and 46. No signs of the weaker P_2 periodicity are seen in periodograms of the 1P-method or the LS-method. The high $A_3 = 0.^m118$ amplitude of the $g_S(t)$ light curve in Fig. A.21c is nearly the same as in the simultaneous DATA_{2,5} (Fig. A.18c). The 1P-model reproduces the y_i changes. The residuals increase slightly in the end and the beginning of data (Fig. A.3d). There is only one minimum in the $g_S(\phi_3)$ curve (Fig. A.3e).

The conservative and the liberal model are not the same. Therefore, the results are different in Tables 7-8 and 9-10. Although the first part of DATA_{1,3} contains very few observations (Figs. A.20ac and A.21cd), all main results presented above agree with those obtained for the partly simultaneous DATA_{2,5}.

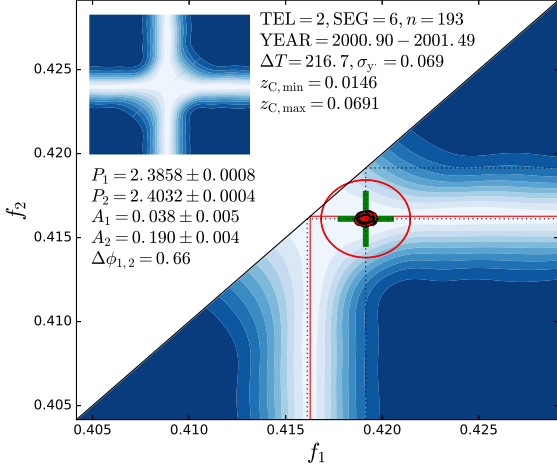


Fig. A.22. DATA_{2,6}. Otherwise as in Fig. 6

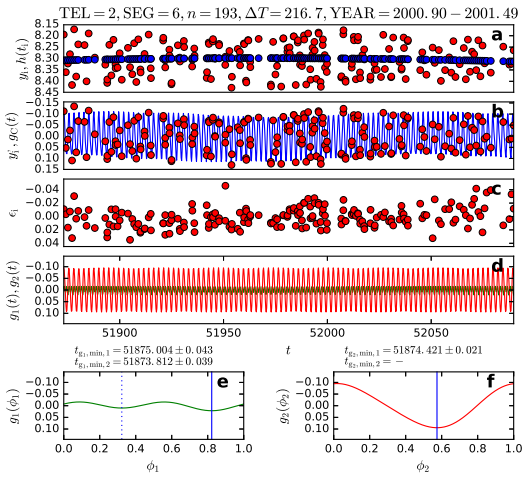


Fig. A.23. DATA_{2,6}. Otherwise as in Fig. 7

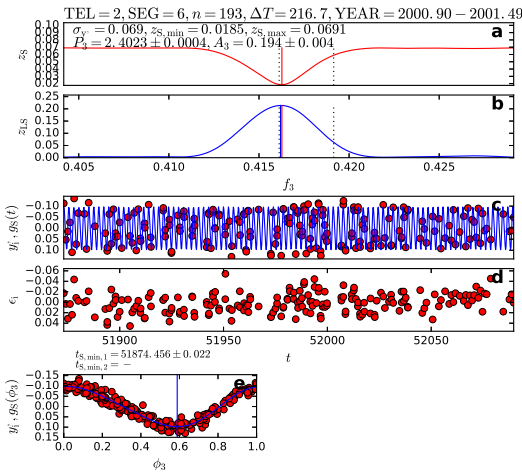


Fig. A.24. DATA_{2,6}. Otherwise as in Fig. 8

A.8. DATA_{2,6}

A cross shape and white arms are present in the $z_C(f_1, f_2)$ periodogram (Fig. A.22). The best model is close to the diagonal line. The red $\pm f_0/2$ circle of Eq. 57 hits the $f_1 = f_2$ diagonal which means that CASE₁ break down of the 2P-model takes place. The black $\pm 3\sigma_{f_1, f_2}$ ellipse of Eq. 58 certainly does not hit this diagonal. No amplitude dispersion takes place. However, the weaker periodicity $P_1 = 2.^d3858 \pm 0.^d0008$ has a low amplitude $A_2 = 0.^m038 \pm 0.^m005$. The high amplitude ratio $R_A = A_2/A_1 = 5.0$ indicates that the stronger periodicity $P_2 = 2.^d4032 \pm 0.^d0004$ dominates. The white arms overlap the red lines denoting the frequency level $1/P_3$ of the 1P-model best period. The results for the 2P-model or the 1P-model would be the same, because the differences $P_2 - P_3 = 0.^d0009 \pm 0.^d0006$ and $A_3 - A_2 = 0.^m006 \pm 0.^m006$ are small. Here we encounter our second CASE₂ break down of the 2P-model (Table 6: 2P-model breaks="CASE₁, CASE₂"). Due to CASE₁ and CASE₂ break down, the 1P-model is the conservative model and the 2P-model is the liberal model.

The second order polynomial h_i can follow the small changes of the mean brightness during $\Delta T = 216.^d7$ (Fig. A.23a). The 2P-model fits nicely to the amplitude changes of y_i (Fig. A.23b). The level and the scatter of the residuals remain stable (Fig. A.23c). The data probably contain a few flares. As expected in CASE₂, the red $g_2(t)$ curve dominates over the green $g_1(t)$ curve (Figs. A.23def). Two minima are seen in the $g_1(\phi_1)$ curve.

Exactly the same period is detected with 1P-method and the LS-method. As predicted by Eqs. 45 and 46, these two periods are nearly equal to the stronger P_2 period detected with the 2P-method (Fig. A.24ab: red and blue vertical lines, black dotted vertical lines). The 1P-method and the LS-method detect no signs of the weaker P_1 signal. The $g_S(t)$ light curve is a good model for the y_i data (Fig. A.24c). No large changes are seen in the level and the scatter of ϵ_i of Eq. 14 (Fig. A.24d). The $g_S(\phi_3)$ curve displays only one minimum (Fig. A.9d).

Since the conservative and liberal model are different, the results are different in Tables 7-8 and 9-10. In the next Sect. A.9, the above results for DATA_{2,6} are confirmed by the analysis of the simultaneous DATA_{1,4}.

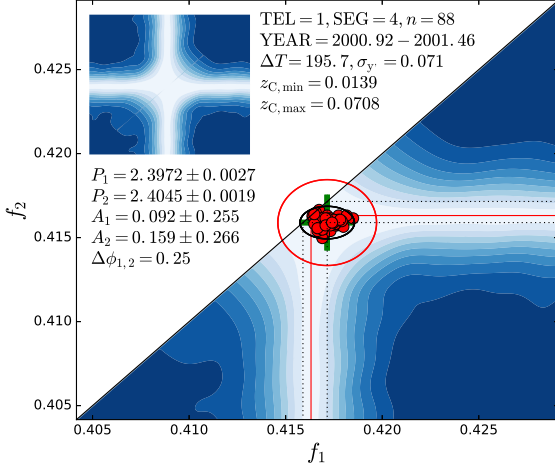


Fig. A.25. DATA_{1,4}. Otherwise as in Fig. 6

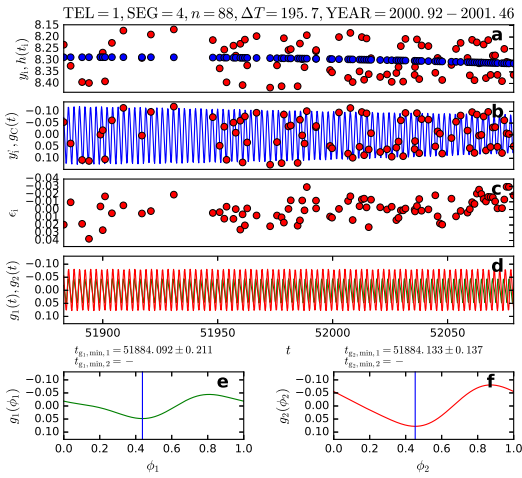


Fig. A.26. DATA_{1,4}. Otherwise as in Fig. 7

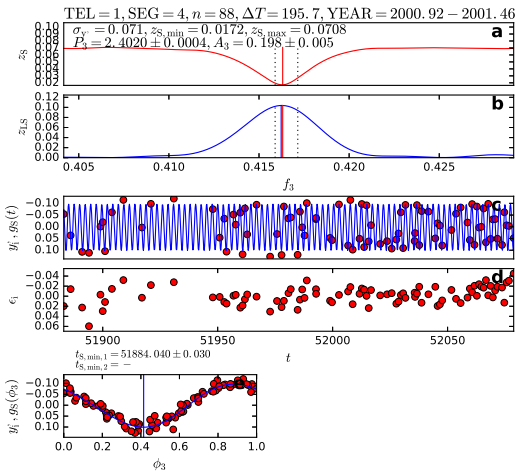


Fig. A.27. DATA_{1,4}. Otherwise as in Fig. 8

A.9. DATA_{1,4}

This is the second smallest data segment analysed with the 2P-method ($n = 88$). The smallest is DATA_{1,3} ($n = 67$). The $z_C(f_1, f_2)$ periodogram displays a cross shape and white arms (Fig. A.25). The best model is so close to the diagonal line that the $\pm f_0/2$ and $\pm 3\sigma_{f_1, f_2}$ limits hit $f_1 = f_2$. The A_1 and A_2 estimates show amplitude dispersion. However, this dispersion is present only in the σ_{A_1} and σ_{A_2} estimates because they are about hundred times larger than the typical values in Tables 7 and 9. The horizontal and vertical red lines denoting the frequency level $1/P_3$ of the 1P-model best period run through the white arms. The 2P-model or the 1P-model would give nearly the same best periods because the difference is only $P_2 - P_3 = 0.^d0025 \pm 0.^d0019$. We conclude that this is a CASE₁ break down of the 2P-model (Table 6: 2P-model breaks down="CASE₁"). This means that the 1P-model is the conservative model and the 2P-model is the liberal model.

The minor changes of the mean brightness of FK com during $\Delta T = 195.7^d7$ can be modelled with the second order polynomial h_i (Fig. A.26a). The $z_{C,\min} = 0.^m0139$ value indicates that the small y_i^j amplitude changes can be reproduced with the 2P-model (Fig. A.26b). The residuals are quite stable (Fig. A.26c). The red $g_2(t)$ curve has a higher amplitude than the green $g_1(t)$ curve (Figs. A.26def). Both curves have only one minimum.

The 1P-method and the LS-method detect the same best period. As predicted by Eqs. 45 and 46, the P_2 value detected with the 2P-method is quite close to these two periods in Fig. A.27ab (red and blue vertical lines, black dotted vertical lines). The $g_S(t)$ light curve follows the y_i^j data (Fig. A.27c), except in the beginning of the segment when the scatter of the residuals increases (Fig. A.27d). There is no secondary minimum in the $g_S(\phi_3)$ curve (Fig. A.27d).

Because the conservative and the liberal models are the same, the results in Tables 7-8 and 9-10 are the same. The above results for the stronger periodicity of DATA_{1,4} agree with those presented for the overlapping DATA_{2,6} in the previous Sect. A.8.

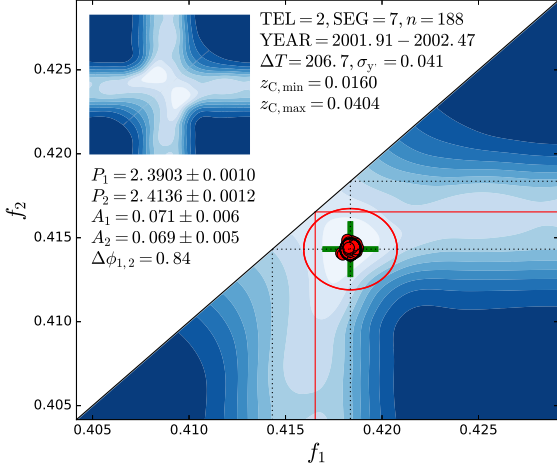


Fig. A.28. DATA_{2,7}. Otherwise as in Fig. 6

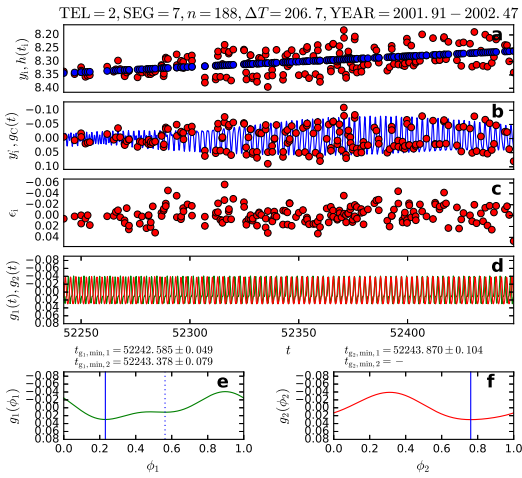


Fig. A.29. DATA_{2,7}. Otherwise as in Fig. 7

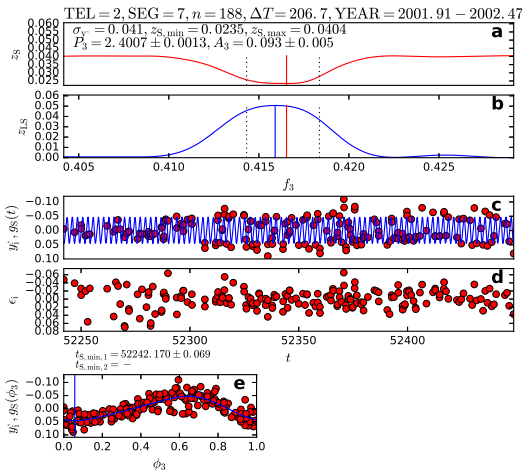


Fig. A.30. DATA_{2,7}. Otherwise as in Fig. 8

A.10. DATA_{2,7}

A hazy cross shape is present and the white arms are absent in the $z_C(f_1, f_2)$ periodogram of Fig. A.28. The distance of the best $g_C(t)$ solution from the $f_1 = f_2$ diagonal excludes the CASE₁ break down. The amplitude ratio $R_A = A_1/A_2 = 1.0$ rules out the CASE₂ and the CASE₃ break down alternatives. For the third time, the 2P-method unambiguously detects two simultaneous real periods. The criterion of Eq. 16 can be used to compare the 2P-model to the 1P-model. The ratio $R_S/R_C = z_{S,\min}^2/z_{C,\min}^2$ in Eq. 15 gives $F = 41.0$. The critical level Q_F of this F value is below our 10^{-16} computational accuracy. Hence, the 2P-model is certainly the best model for these data. Note that the $1/P_3$ red lines of the best period of the 1P-model do not coincide with the $1/P_1$ or the $1/P_2$ dotted lines of the best periods of the 2P-model. We conclude that the 2P-model is both the conservative and the liberal model.

The light curve of FK Com undergoes significant changes during $\Delta T = 206.^d7$. The mean brightness increases about $0.^m05$, while the amplitude first increases and then decreases (Fig. A.29a). Although the second order polynomial h_i can not follow the changes of the mean in the end of the segment, the 2P-model fits the y_i data quite nicely (Fig. A.29b). The level of residual stays close to zero, but their scatter increases in the end of the segment (Fig. A.29c). The $g_1(t)$ and $g_2(t)$ light curve amplitudes are comparable, and the former curve has two minima (Figs. A.29edf). The mean of the residuals, $z_{C,\min} = 0.^m016$, demonstrates that the 2P-model can successfully model about seven months of the constantly changing light curve of FK Com

The 1P-method and the LS-method detect slightly different periods (Fig. A.30ab: red and blue vertical lines). Both of these periods deviate considerably from the best P_1 and P_2 detected with the 2P-method (Fig. A.30ab: dotted lines). There is a simple explanation for this result. The amplitudes A_1 and A_2 are nearly equal which means that the alternative of Eq. 35 is true. Thus, the frequency of the observed interference light curve $g_1(t) + g_2(t)$ is about $(P_1^{-1} + P_2^{-1})/2$ (Eq. 39). The 1P-method and the LS-method detect this spurious periodicity. The $g_S(t)$ model can not follow the y_i data (Fig. A.30c), and the residuals are large (Fig. A.30d). The $g_S(\phi_3)$ curve has only one minimum (Fig. A.30e).

The results in Tables 7-8 and 9-10 are the same, because the conservative and the liberal models are the same. In the next Sect. A.11, we show that the simultaneous observations of DATA_{1,5} confirm the presence of the above P_1 and P_2 periodicities.

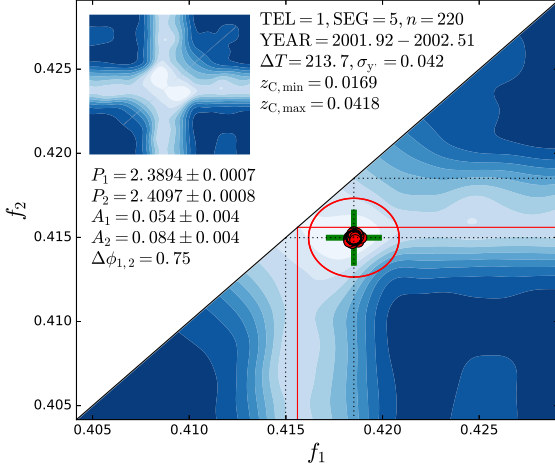


Fig. A.31. DATA_{1,5}. Otherwise as in Fig. 6

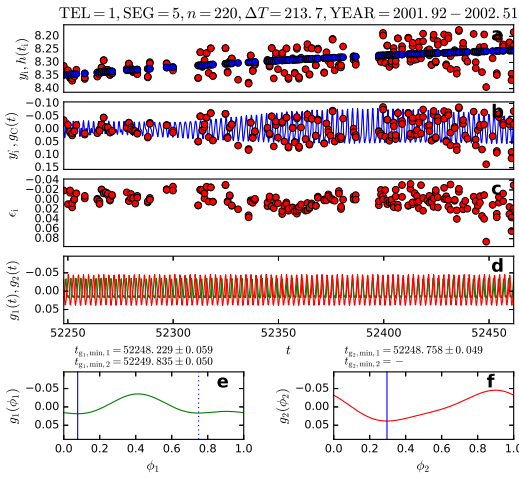


Fig. A.32. DATA_{1,5}. Otherwise as in Fig. 7

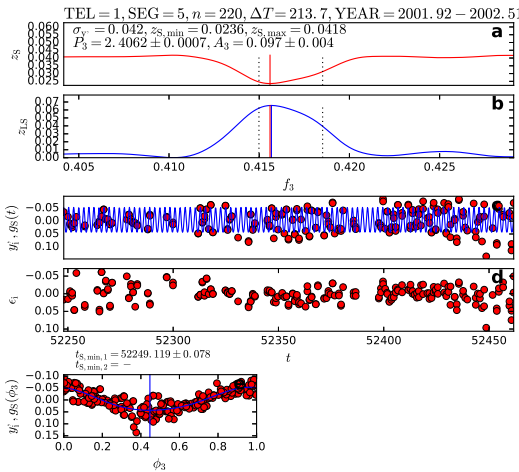


Fig. A.33. DATA_{1,5}. Otherwise as in Fig. 8

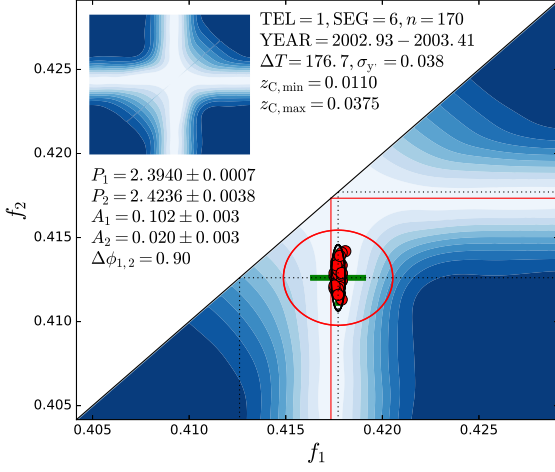
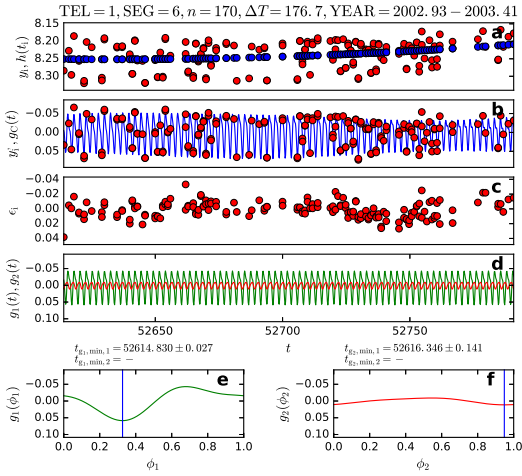
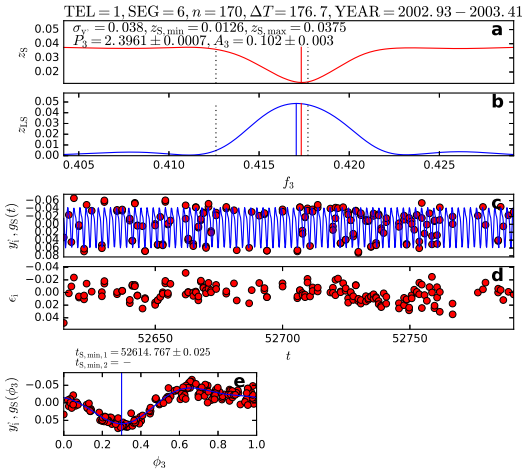
A.11. DATA_{1,5}

The $z_C(f_1, f_2)$ periodogram shows a hazy cross shape, but no white arms (Fig. A.31). We can rule out the CASE₁ break down alternative, because the best $g_C(t)$ solution is far from the $f_1 = f_2$ diagonal. The CASE₂ and CASE₃ break down alternatives can also be ruled out, because the amplitude ratio is $R_A = A_2/A_1 = 1.6$. This is our fourth unambiguous detection of two simultaneous real periods of FK Com. The $R_S/R_C = z_{S,\min}^2/z_{C,\min}^2$ ratio yields $F = 39.7$ (Eq. 15). The critical level Q_F of this F value is far below our 10^{-16} computational accuracy, and the criterion of Eq. 16 confirms that the 2P-model is the best model for these data. Neither one of the dotted lines denoting the $1/P_1$ or the $1/P_2$ frequencies coincides with the continuous red lines denoting the $1/P_3$ frequency. The differences from the simultaneous DATA_{2,7} are only $0.^d0009 \pm 0.^d0012$ in P_1 , $0.^d0039 \pm 0.^d0014$ in P_2 , $0.^m017 \pm 0.^m007$ in A_1 and $0.^m015 \pm 0.^m006$ in A_2 . In this segment, the 2P-model is both the conservative and the liberal model.

Our Fig. A.32a shows the same changes of light curve of FK Com that were already seen in Fig. A.29a. The changes of the mean brightness can not be entirely modelled with a second order polynomial. The 2P-model reproduces the y_i data (Fig. A.32b), but the scatter of the residuals increases towards the end of the data (Fig. A.32c). These residuals show some regular fluctuation, because the polynomial h_i can not follow all changes of the mean brightness of FK Com. There are some obvious outliers. The $g_1(t)$ and $g_2(t)$ light curve amplitudes are of the same order (Figs. A.32d). As in the simultaneous DATA_{2,7}, the green $g_1(\phi_3)$ curve has two minima, while the red $g_2(\phi_3)$ curve has only one minimum (Figs. A.32ef).

The periods detected with the 1P-method and the LS-method are not exactly the same (Fig. A.33ab: red and blue vertical lines). As in the simultaneous DATA_{2,7}, these two unreal periods are far from the best P_1 and P_2 periods detected with the 2P-method (Fig. A.33ab: dotted lines). These unreal periods are closer to the stronger P_2 periodicity, as predicted by Eqs. 45 and 46. The condition of equal amplitudes A_1 and A_2 (Eq. 35) is not fulfilled. For this reason, the frequency of the observed light curve $g_1(t) + g_2(t)$ also differs more from $(P_1^{-1} + P_2^{-1})/2$ (Eq. 39). Nevertheless, the unreal periods detected with the 1P-method and the LS-method are between the periods P_1 and P_2 detected with the 2P-method. The $g_S(t)$ model does not fit to the y_i data (Fig. A.33c). The residuals are large. Their scatter increases in the end and in the beginning of the segment (Fig. A.33d). Only one minimum is seen the $g_S(\phi_3)$ curve (Fig. A.33e).

The results given in Tables 7-8 and 9-10 are the same, because the conservative and the liberal models are the same. All results presented above confirm those already presented in Sect. A.10 for the simultaneous DATA_{2,7}.


Fig. A.34. DATA_{1,6}. Otherwise as in Fig. 6

Fig. A.35. DATA_{1,6}. Otherwise as in Fig. 7

Fig. A.36. DATA_{1,6}. Otherwise as in Fig. 8

A.12. DATA_{1,6}

A cross shape and white arms are present in the $z_C(f_1, f_2)$ periodogram of Fig. A.34. The best $g_C(t)$ model is in the middle of the vertical white arm. The CASE₁ break down of the 2P-model does not take place, because the $\pm f_0/2$ and $\pm 3\sigma_{f_1, f_2}$ limits do not hit the diagonal line $f_1 = f_2$. The high amplitude ratio $R_A = A_1/A_2 = 5.1$ means that the signal of the stronger $P_1 = 2.^d3940 \pm 0.^d0007$ periodicity dominates. The location of the best $1/P_2$ frequency on the vertical white arm is uncertain, because the error ratio is $\sigma_{P_2}/\sigma_{P_1} = 5.4$ (Eq. 58: Black ellipse). The vertical and horizontal red lines denoting the frequency level $1/P_3$ of the 1P-model best period coincide with the white arms. The differences $P_3 - P_1 = 0.^d0021 \pm 0.^d010$ and $A_3 - A_1 = 0.^m000 \pm 0.^m004$ are small. All the above details support our conclusion that a CASE₃ break down of the 2P-model occurs. Therefore, the 1P-model is the conservative model, while 2P-model is the liberal model.

The light curve mean brightness increases and the amplitude decreases during six months (Fig. A.35a). Except for the end of the segment, the minor changes of the mean can be modelled with the second order polynomial of Eq. 1. The $z_C(t)$ model can reproduce the light curve changes (Fig. A.35b). The residuals show some regular temporal variation (Fig. A.35c), because the polynomial fit h_i does not entirely follow the real mean of the original data. Due to CASE₃, the green $g_1(t)$ light curve dominates over the red $g_2(t)$ light curve (Figs. A.35edf). Both curves have only one minimum.

The 1P-model best period is $P_3 = 2.^d3961 \pm 0.^d0007$ (Fig. A.36a). The LS-method result for the best period is approximately the same (Fig. A.36b). The periods are close to the stronger P_1 signal. No signs of the weaker P_2 signal are detected with the 1P-method or the LS-method. The light curve amplitude $A_3 = 0.^m102 \pm 0.^m003$ is high. The level of the model residuals shows some regular fluctuation (Fig. A.36d). However, the mean residual value $z_{S,\min} = 0.^m0126$ is excellent considering that we model about six months of data. Only one minimum is seen in the $g_S(\phi_3)$ phase plot (Fig. A.36e).

The results given in Tables 7-8 and 9-10 are different, because the conservative and the liberal models are different. Simultaneous TEL=2 observations are available. The analysis DATA_{2,8} presented in the next Sect. A.13 confirms the results presented above.

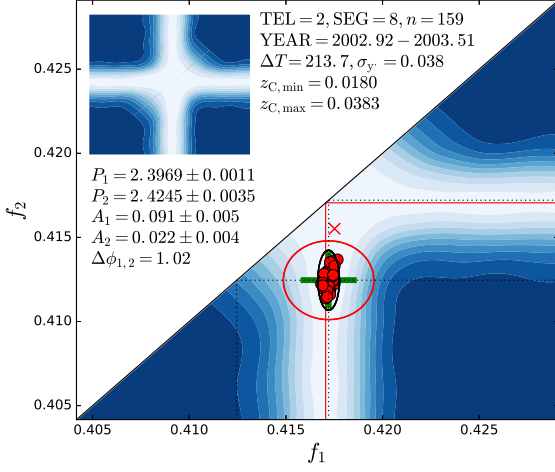


Fig. A.37. DATA_{2,8}. Otherwise as in Fig. 6

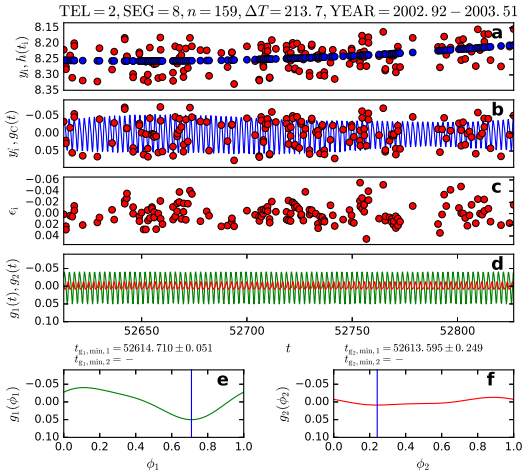


Fig. A.38. DATA_{2,8}. Otherwise as in Fig. 7

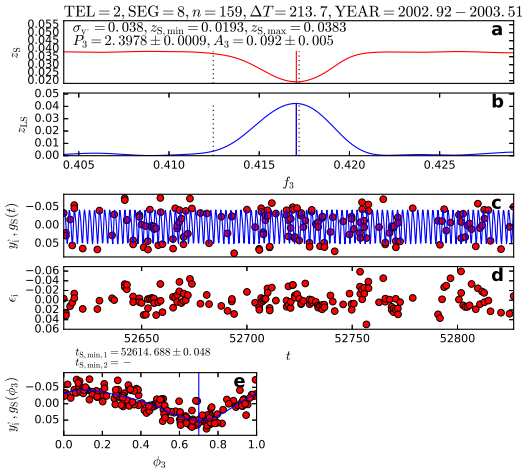


Fig. A.39. DATA_{2,8}. Otherwise as in Fig. 8

A.13. DATA_{2,8}

The $z_C(f_1, f_2)$ periodogram shows a cross shape, white arms and the best $g_C(t)$ model in the middle of the vertical white arm (Fig. A.37). The $\pm f_0/2$ and $\pm 3\sigma_{f_1, f_2}$ limits are so far from the $f_1 = f_2$ diagonal that no CASE₁ break down of the 2P-model takes place. The signal of the stronger $P_1 = 2.^d3969 \pm 0.^d0011$ periodicity dominates ($R_A = A_1/A_2 = 4.1$). The error ratio $\sigma_{P_2}/\sigma_{P_1} = 3.2$ means that the location of $1/P_2$ on the vertical white arm is uncertain (Eq. 58: Black ellipse). The white arms coincide with red lines denoting frequency level $1/P_3$ of the 1P-model. The differences $P_3 - P_1 = 0.^d0009 \pm 0.^d0014$ and $A_3 - A_1 = 0.^m001 \pm 0.^m007$ are insignificant. One red “x” symbol denotes a bootstrap model solution that is outside the red circle of Eq. 57. As in the previous analysis of simultaneous DATA_{1,6}, we arrive at the conclusion that this is a CASE₃ break down of the 2P-model. This means that the 1P-model is the conservative model, while the 2P-model is the liberal model.

Our Fig. A.38a shows a similar FK Com light curve as was observed during the simultaneous DATA_{1,6} (Fig. A.35a). A second order polynomial can follow the minor changes of the mean. The $z_C(t)$ model can not reproduce all light curve changes (Fig. A.38b), because the scatter of residuals is quite large in the end of the segment (Fig. A.38c). The green $g_1(t)$ light curve dominates in the $g_C(t)$ sum curve (Figs. A.38edf). The $g_1(\phi_1)$ and $g_2(\phi_2)$ light curves have only one minimum.

The 1P-method gives the best period $P_3 = 2.^d3978 \pm 0.^d0009$ (Fig. A.39a). The LS-method detects exactly the same period (Fig. A.39b) which is also nearly equal to the 2P-method best period P_1 . However, the 1P-method and the LS-method detect no signs of the weaker P_2 signal. The level of residuals is stable, but their scatter increases in the end of the data (Fig. A.39d). The $g_S(\phi_3)$ phase plot shows only one minimum (Fig. A.39e).

The conservative and the liberal models are different. Therefore, we give different results in Tables 7-8 and 9-10. Our analysis of DATA_{2,8} confirms the results obtained earlier for the simultaneous DATA_{1,6} (Sect. A.12).

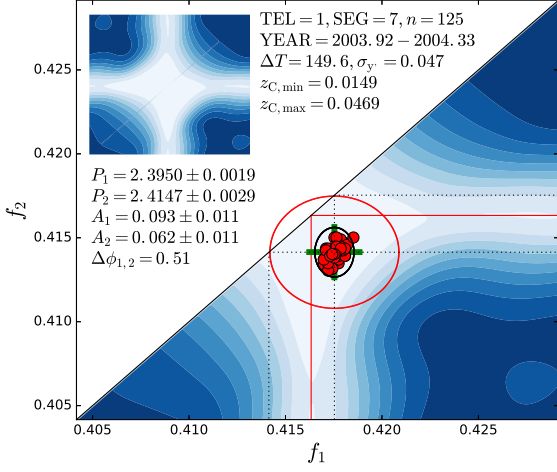


Fig. A.40. DATA_{1,7}. Otherwise as in Fig. 6

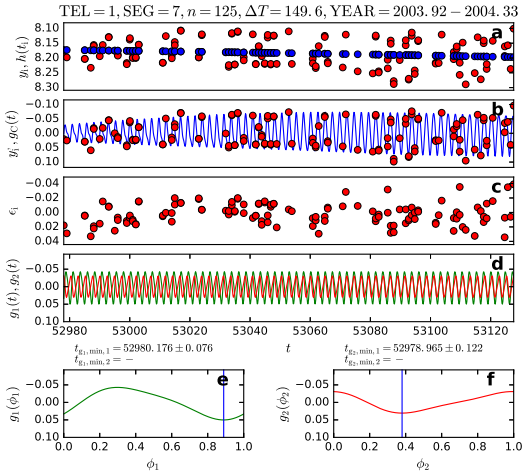


Fig. A.41. DATA_{1,7}. Otherwise as in Fig. 7

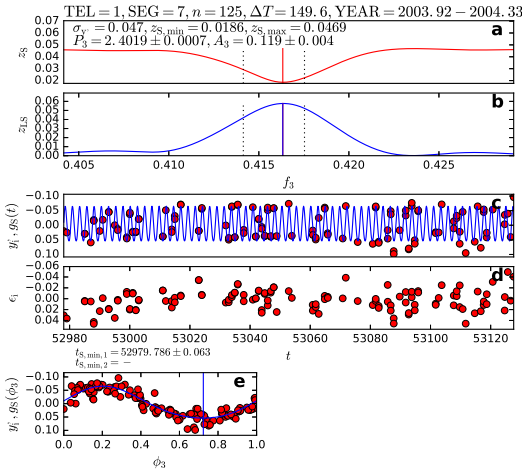


Fig. A.42. DATA_{1,7}. Otherwise as in Fig. 8

A.14. DATA_{1,7}

The $z_C(f_1, f_2)$ periodogram shows a cross shape, but the arms of this cross get bluer closer to the lower and the right edge (Fig. A.40). The best $g_C(t)$ model is in the upper end of the vertical arm. A CASE₁ break down of the 2P-model takes place, because the $\pm f_0/2$ limit hits $f_1 = f_2$. However, the $\pm 3\sigma_{f_1, f_2} 2$ limit does not hit $f_1 = f_2$. The red lines denoting the frequency level $1/P_3$ of the best period of the 1P-model coincide with the arms of the cross. The red lines are far from the dotted lines which means that the 2P-method and the 1P-method give different results. We conclude that the 1P-model is the conservative model and the 2P-model is the liberal model.

Small changes of the mean brightness are seen and the amplitude increases towards the end of the segment (Fig. A.41a). A second order polynomial h_i mostly follows the changes of the mean brightness. The $z_C(t)$ model can reproduce the light curve changes (Fig. A.41b). The level of residuals is stable, but the scatter is larger in the ends of the segment (Fig. A.41c). The amplitudes of the $g_1(t)$ and the $g_2(t)$ light curves are of the same order (Figs. A.41edf). Both of these curves have only one minimum.

The 1P-method detects exactly the same best period as the LS-method (Fig. A.42ab: blue vertical line overlaps red vertical line). The dotted vertical lines show that the 2P-method gives completely different results. Since the condition $A_1 \approx A_2$ is true (Eq. 35), the predicted observed light curve period is $[(P_1^{-1} + P_2^{-1})/2]^{-1}$ (Eq. 39). The 1P-method and the LS-method detect this spurious period. The $g_S(t)$ model follows the data (Fig. A.42c), except in the end of the segment when the scatter of residuals increases (Fig. A.42d). Only one minimum is seen in the $g_S(\phi_3)$ phase plot (Fig. A.42e).

The conservative and the liberal models are different, and we give different results in Tables 7-8 and 9-10. In the next section, we show that the simultaneous DATA_{2,9} confirms some of these results for DATA_{1,7}. There are also differences, because DATA_{2,9} is 73 days longer than DATA_{1,7}.

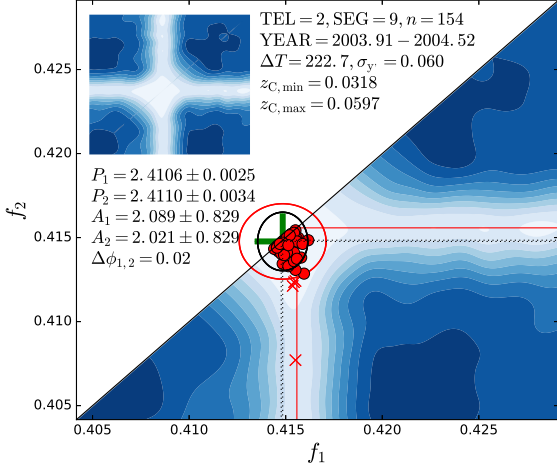


Fig. A.43. DATA_{2,9}. Otherwise as in Fig. 6

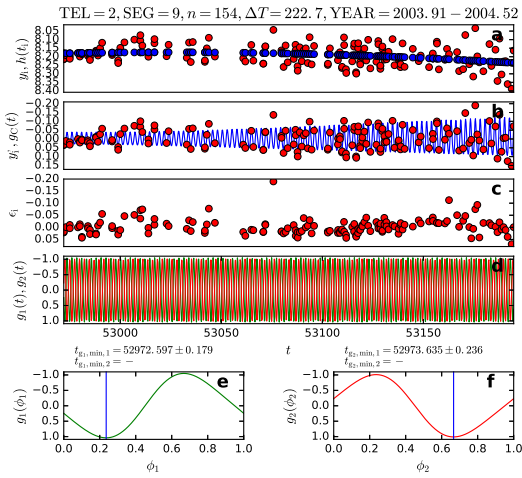


Fig. A.44. DATA_{2,9}. Otherwise as in Fig. 7

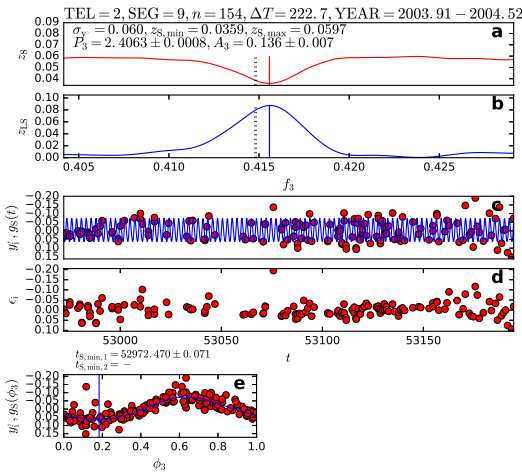


Fig. A.45. DATA_{2,9}. Otherwise as in Fig. 8

A.15. DATA_{2,9}

A cross shape is seen in the $z_C(f_1, f_2)$ periodogram (Fig. A.43). The arms of this cross are white. These arms overlap the red lines denoting the frequency level $1/P_3$ of the best period of the 1P-model. The $\pm f_0/2$ and the $\pm 3\sigma_{f_1, f_2}$ limits hit $f_1 = f_2$. Amplitude dispersion takes place. Four of the 50 first bootstrap model solutions are outside the red $\pm f_0/2$ circle (Fig. A.43: red “x” symbol). This is a clear CASE₁ break down of the 2P-model. Hence, the 1P-model is both the conservative and the liberal model.

The amplitude increases towards the end of the segment, and the second order a polynomial h_i can approximately follow the changes of the mean brightness (Fig. A.44a). The $z_C(t)$ model fits to the y_i data (Fig. A.44b). The level and the scatter of the residuals in Fig. A.44c are stable, but there are a few outliers which are probably flares. There is one such extreme outlier. Due to amplitude dispersion, the $g_1(t)$ and $g_2(t)$ light curves are unrealistic (Figs. A.44edf).

The 1P-method and the LS-method detect nearly the same best period (Fig. A.45ab: blue and red vertical lines nearly overlap). The 2P-method detects different periodicities. The above mentioned very large outliers are the reason for the high $z_{S,min} = 0.^m0359$ value. Regardless of this, the $g_S(t)$ model can follow the data (Fig. A.45c), and the residuals are more or less stable (Fig. A.45d). The $g_S(\phi_3)$ phase plot shows only one minimum (Fig. A.45e).

In this segment, the results in Tables 7-8 and 9-10 are the same, because the conservative and the liberal models are the same. The temporally overlapping DATA_{1,7} and DATA_{2,9} begin nearly at the same time, but the latter ends about two and a half months later. Regardless of this, the results for the periods agree quite nicely (see Fig. 10b).

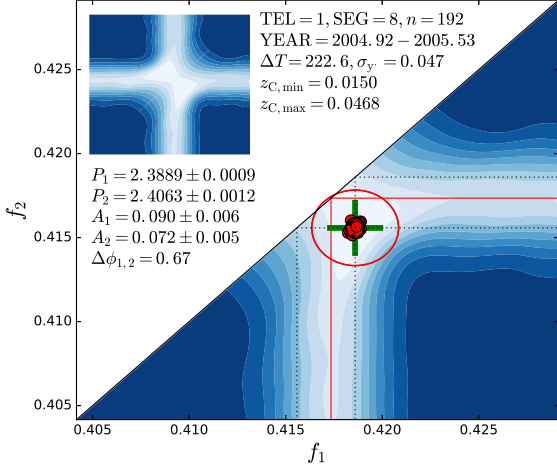


Fig. A.46. DATA_{1,8}. Otherwise as in Fig. 6

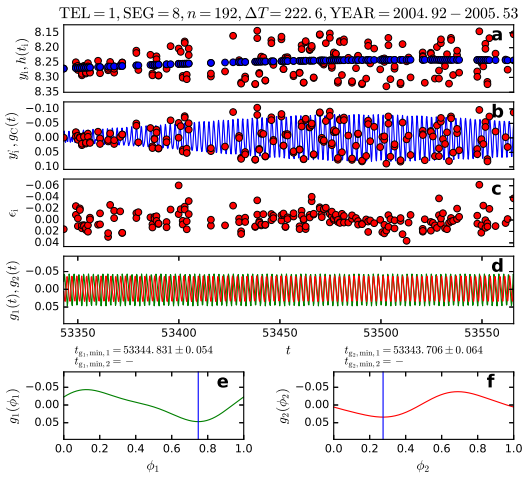


Fig. A.47. DATA_{1,8}. Otherwise as in Fig. 7

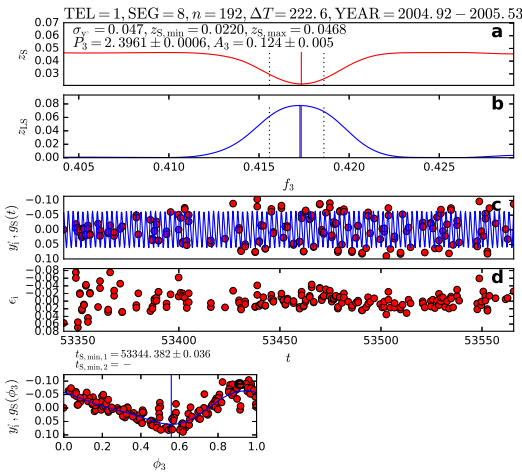


Fig. A.48. DATA_{1,8}. Otherwise as in Fig. 8

A.16. DATA_{1,8}

The $z_C(f_1, f_2)$ periodogram shows a hazy cross shape and the ends of the arms of of this cross are darker (Fig. A.46). The red lines denoting the frequency level $1/P_3$ of the best period of the 1P-model run through these arms. These red lines deviate a lot from the dotted lines denoting the frequencies $1/P_1$ and $1/P_2$ of the bests period of the $g_C(t)$ model. Although this model is not close to the diagonal, the $\pm f_0/2$ limit hits $f_1 = f_2$ and a CASE₁ break down of the 2P-model takes place. The $\pm 3\sigma_{f_1, f_2}$ limit, however, does not hit $f_1 = f_2$. This means that the 1P-model is the conservative model, while the 2P-model is the liberal model.

A second order polynomial h_i can easily follow the small changes of the light curve mean (Fig. A.47a). The brightness variations increase towards the end of the segment. The $z_C(t)$ model can reproduce these y_i changes (Fig. A.47b). The residuals are stable (Fig. A.47c), although there are few outliers that may be flares. The amplitudes of the $g_1(t)$ and $g_2(t)$ light curves are nearly the same, and both curves have only one minimum (Figs. A.47edf).

The best periods detected with the 1P-method and the LS-method are nearly the same (Fig. A.48ab: blue and red vertical lines nearly overlap). However, these periods are far from the best periods P_1 and P_2 detected with the 2P-method (Fig. A.48ab: dotted vertical lines). The amplitudes $A_1 \approx A_2$ (Eq. 35) predict the detection of $P^{-1} = (P_1^{-1} + P_2^{-1})/2$ (Eq. 39), and it is just this spurious periodicity that both the 1P-method and LS-method do detect. The $g_S(t)$ model fails to follow the large changes of the light curve amplitude (Fig. A.48c). For this reason, the residuals show a very large scatter in the beginning of the segment (Fig. A.48d). There is only one minimum in the $g_S(\phi_3)$ phase plot Fig. A.48e).

The conservative and the liberal models are different, and therefore the results are different in Tables 7-8 and 9-10. Unfortunately, there are no temporally overlapping TEL=2 observations for checking the results presented above.

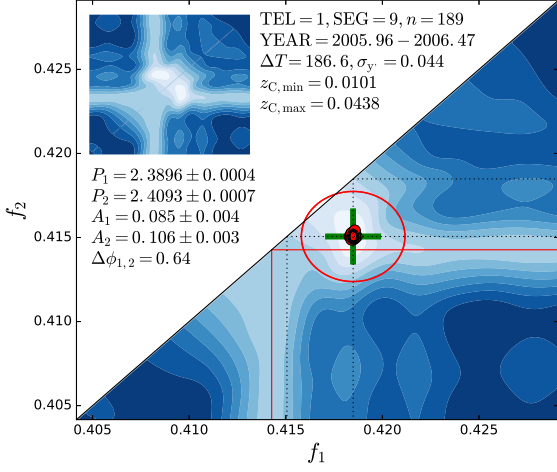


Fig. A.49. DATA_{1,9}. Otherwise as in Fig. 6

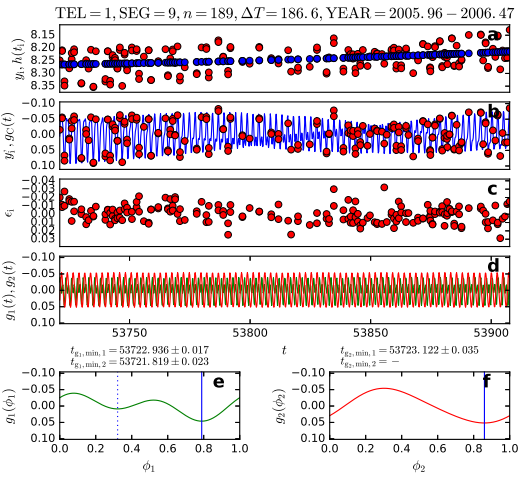


Fig. A.50. DATA_{1,9}. Otherwise as in Fig. 7

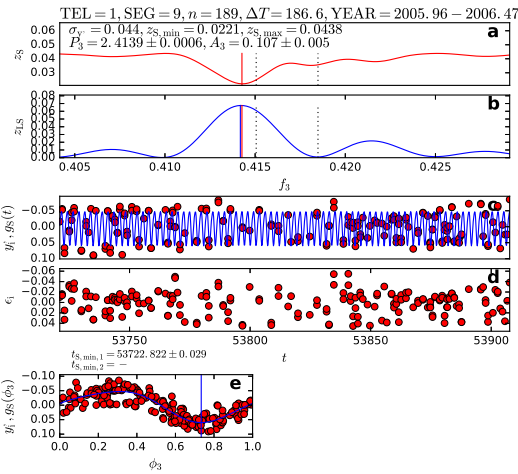


Fig. A.51. DATA_{1,9}. Otherwise as in Fig. 8

A.17. DATA_{1,9}

A broken hazy cross shape is seen in the $z_C(f_1, f_2)$ periodogram (Fig. A.49). The light blue arms of this cross coincide with the frequency level $1/P_3$ of the best period of the 1P-model. The continuous red and the dotted black lines deviate considerably which means that the best periods detected with the 2P-method and the 1P-method are different. The best $g_C(t)$ model is not close to the diagonal. However, this is a CASE₁ break down of the 2P-model, because the $\pm f_0/2$ limit hits $f_1 = f_2$. The $\pm 3\sigma_{f_1, f_2}$ limit certainly does not hit $f_1 = f_2$. In this segment, the 1P-model is the conservative model, while the 2P-model is the liberal model.

The small light curve mean changes can be modelled with a second order polynomial (Fig. A.50a). The amplitude decreases first and then increases. The $z_C(t)$ model fits nicely to these amplitude changes (Fig. A.50b). The residuals are stable (Fig. A.50c). Their mean $z_{C,\min} = 0.^m0101$ is comparable to accuracy of the data, although the observations seem to contain a few flares. The 2P-model can successfully follow the constantly changing light curve of FK Com for over six months. Neither one of the high amplitude $g_1(t)$ and $g_2(t)$ light curves dominates. The former curve has two minima (Figs. A.50edf).

The 1P-method and the LS-method detect nearly the same best period (Fig. A.51ab: blue and red vertical lines). The value of this period deviates considerably from the best periods P_1 and P_2 detected with the 2P-method (Fig. A.51ab: dotted vertical lines). The spurious P_3 periodicity is closer to the stronger P_2 periodicity, as predicted by Eqs. 45 and 46. However, these predicted frequency values are certainly correct only if $g_1(t)$ and $g_2(t)$ are sinusoids. This is not true in DATA_{1,9} because $g_1(t)$ is a double wave. The 1P-method and LS-method periodograms show no indication of the presence of the weaker P_1 signal. The residuals of the $g_S(t)$ model are large (Fig. A.51cd). This result could be expected because the 1P-model fails to adapt to the amplitude changes of the light curve. The $g_S(\phi_3)$ phase plot show only one minimum Fig. A.51e).

The results in Tables 7-8 and 9-10 are different for this segment, because the conservative and the liberal models are different. No temporally overlapping TEL=2 observations are available to check these results obtained for DATA_{1,9}.

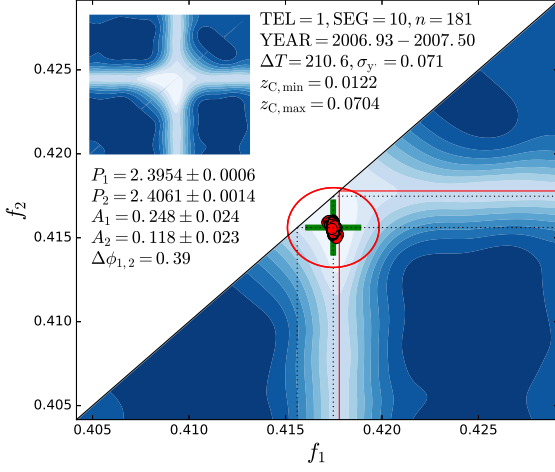


Fig. A.52. DATA_{1,10}. Otherwise as in Fig. 6

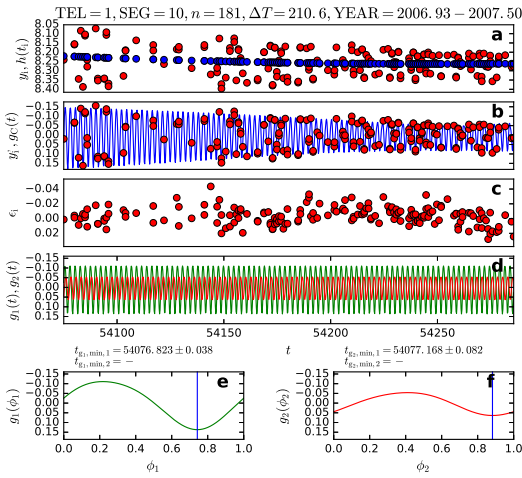


Fig. A.53. DATA_{1,10}. Otherwise as in Fig. 7

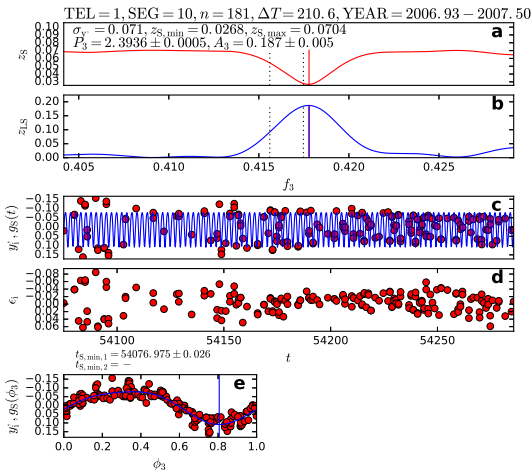


Fig. A.54. DATA_{1,10}. Otherwise as in Fig. 8

A.18. DATA_{1,10}

The $z_C(f_1, f_2)$ periodogram shows a cross shape and the arms of this cross become darker further away from the diagonal line (Fig. A.52). The red lines denoting the frequency level $1/P_3$ of the best period of the 1P-model run through these arms. These red lines are close to the dotted black lines denoting the frequency of the stronger $1/P_1$ period detected with the 2P-method. A CASE₁ break down of the 2P-model takes place because the $\pm f_0/2$ limit hits $f_1 = f_2$. Some amplitude dispersion is present, because the σ_{A_1} and σ_{A_2} values are about ten times larger than the typical values in Table 7. However, the distance between the diagonal line and the location of best $g_C(t)$ model is large enough for that the $\pm 3\sigma_{f_1, f_2}$ limit does not hit $f_1 = f_2$. For these reasons, the 1P-model is the conservative model, while the 2P-model is the liberal model.

The light curve amplitude is high in the beginning of the segment, but it decreases relatively fast during $\Delta T = 210.$ ^{d6} (Fig. A.53a). The changes of the mean brightness are moderate and can be modelled with a second order polynomial. The $z_C(t)$ model can again reproduce all light curve changes (Fig. A.53b). The mean level and the scatter of the residuals are stable (Fig. A.53c). We can model about seven months of the constantly changing light curve of FK Com, and this model reaches $z_{C,\min} = 0.^m0112$. The $g_1(t)$ signal dominates over the $g_2(t)$ signal. The amplitudes of these sinusoidal signals are high (Figs. A.53edf).

Exactly the same period is detected with the 1P-method and the LS-method (Fig. A.54ab: blue and red vertical lines overlap). As predicted by Eqs. 45 and 46, this period is close to the stronger period P_1 detected with the 2P-method (Fig. A.54ab: dotted vertical lines). The 1P-method and the LS-method detect no signs of the P_2 signal, although it has a high amplitude $A_2 = 0.^m118$. The 1P-model can not adapt to the significant amplitude changes of the light curve (Fig. A.54cd). This $g_S(\phi_3)$ model has only one minimum (Fig. A.54e).

The conservative and liberal models for DATA_{1,10} are not the same, and different results are given in Tables 7-8 and 9-10. There are no temporally overlapping TEL=2 observations to check these results obtained for DATA_{1,10}.

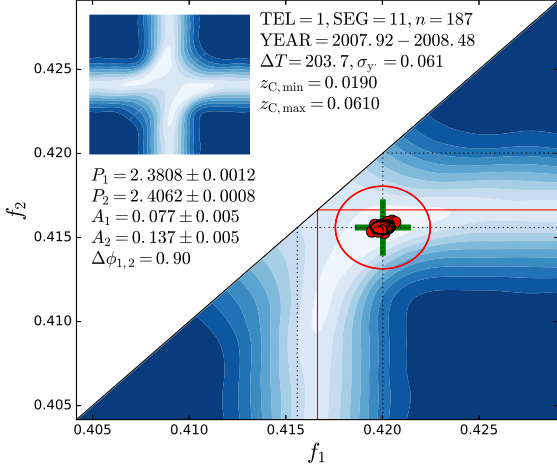


Fig. A.55. DATA_{1,11}. Otherwise as in Fig. 6

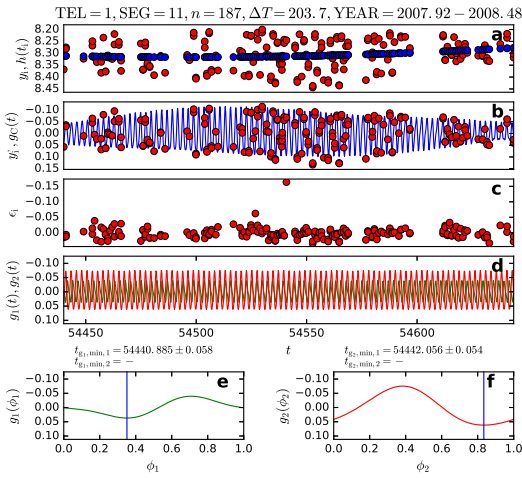


Fig. A.56. DATA_{1,11}. Otherwise as in Fig. 7

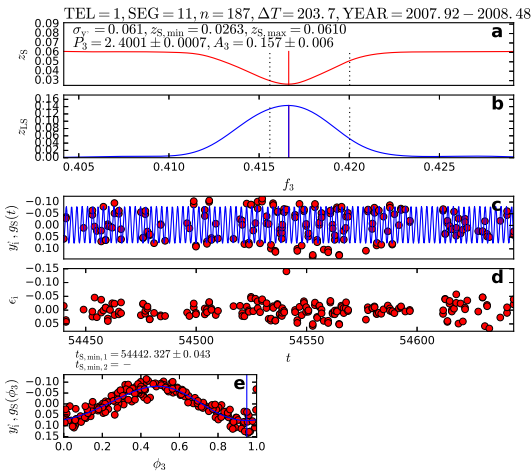


Fig. A.57. DATA_{1,11}. Otherwise as in Fig. 8

A.19. DATA_{1,11}

A hazy blue cross with light blue arms is seen in the $z_C(f_1, f_2)$ periodogram (Fig. A.55). The ends of these arms coincide with the red lines denoting the frequency level $1/P_3$ of the best period of the 1P-model. The location of these red lines deviates considerably from the locations of the dotted black lines denoting the frequencies $1/P_1$ and $1/P_2$ of the best periods detected with the 2P-method. There is no CASE₁ break down, because the $\pm f_0/2$ limit does not hit $f_1 = f_2$. The amplitude ratio is so low that the CASE₂ and the CASE₃ break down alternatives can also be ruled out. The $\pm 3\sigma_{f_1, f_2}$ black circle is very far from the $f_1 = f_2$ diagonal. The Q_F value in Table 6 is so extreme that we can be absolutely sure that the 2P-model is a better model than the 1P-model. We conclude that the 2P-model is both the conservative and the liberal model.

The light curve amplitude first increases and then decreases during $\Delta T = 203.^d7$ (Fig. A.56a). The second order polynomial can easily reproduce the minor changes of the mean brightness. The 2P-model fits to all light curve changes (Fig. A.56b). There is one exceptional outlier in Fig. A.56c and it could be a flare. This outlier is the reason for a bit higher $z_{C,\min} = 0.^m0190$ value, because the level and scatter of other residuals is otherwise stable. The $g_2(t)$ signal is about two times stronger than the $g_1(t)$ signal. Both of these high amplitude signals have only one minimum (Figs. A.56edf).

The 1P-method and the LS-method detect nearly the same best period (Fig. A.57ab: blue and red vertical lines). These two periods are between the two best periods P_1 and P_2 detected with the 2P-method (Fig. A.57ab: dotted vertical lines). They are also closer to the periodicity of the higher amplitude P_2 signal, as predicted by Eqs. 45 and 46. In short, the 1P-method and the LS-method detect a spurious period. The amplitude of the 1P-model is constant, and it fails to reproduce the light curve changes (Fig. A.57cd). The shape of $g_S(\phi_3)$ is sinusoidal (Fig. A.57e).

Since the conservative and liberal models are the same, the same results are given for DATA_{1,11} Tables 7-8 and 9-10. These results for DATA_{1,11} can not be checked with overlapping TEL=2 data.

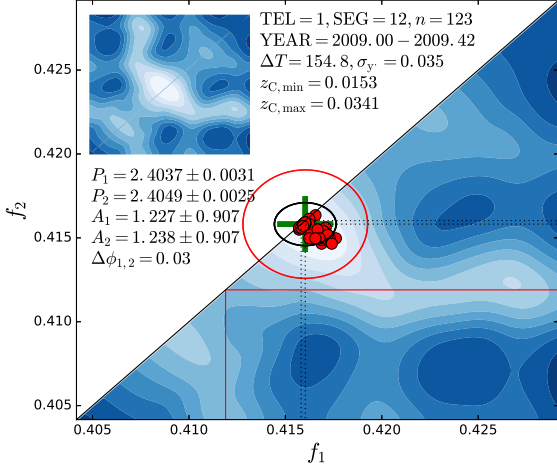


Fig. A.58. DATA_{1,12}. Otherwise as in Fig. 6

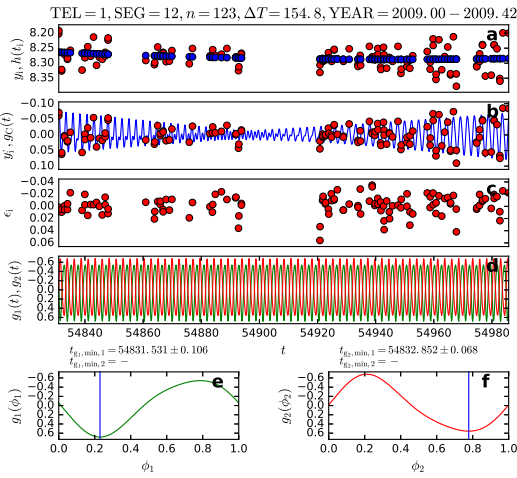


Fig. A.59. DATA_{1,12}. Otherwise as in Fig. 7

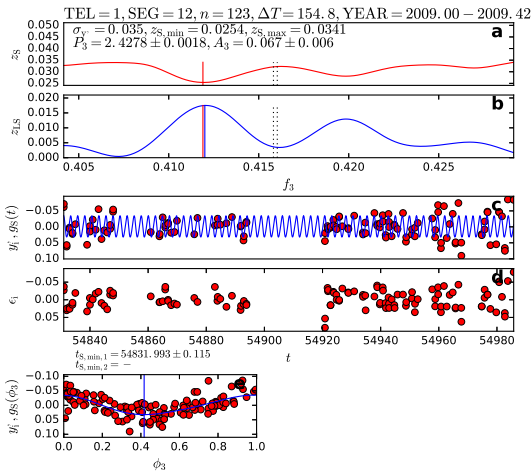


Fig. A.60. DATA_{1,12}. Otherwise as in Fig. 8

A.20. DATA_{1,12}

The $z_C(f_1, f_2)$ periodogram of Fig. A.58 is enigmatic. There is no cross shape, nor clear arms. The red lines denoting the frequency level $1/P_3$ of the best period of the 1P-model run through light blue areas having a much higher level than the white $z_{C,\min} = 0.0153$ level. This absence of arms indicates that the 1P-model is not the correct model for these data. However, the best 2P-model close to the diagonal line shows a clear CASE₁ break down with strong amplitude dispersion. Both the $\pm f_0/2$ limit and the $\pm 3\sigma_{f_1, f_2}$ limit hit $f_1 = f_2$. It seems that neither the 1P-model, nor the 2P-model, is a good model for these data.

This sample is smaller ($n = 123$) and shorter ($\Delta T = 154.8$) than many other samples. A second order polynomial can model the small changes of the mean brightness (Fig. A.59a). The light curve amplitude decreases in the beginning of the segment. The 2P-model suggests that this amplitude approaches zero in the middle of the segment and exactly when there is a gap in the observations (Fig. A.59b). After this gap, the amplitude increases rapidly. The scatter of the residuals is large at both sides of the above mentioned gap, as well as after this gap (Fig. A.59c). The sinusoidal $g_1(t)$ and $g_2(t)$ high amplitude signals are unrealistic (Figs. A.59edf).

The 1P-method and the LS-method detect nearly the same best period (Fig. A.60ab: blue and red vertical lines). This period is very far from the P_1 and P_2 periods detected with the 2P-method (Fig. A.60ab: dotted vertical lines). The 1P-model fails to reproduce the light curve changes and the residuals are large (Fig. A.60cd). The $g_S(\phi_3)$ light curve shows only one minimum (Fig. A.60e).

We have checked that if the photometry before and after the gap is plotted with phases computed with the period of $P_1 = 2.4049$, there is a phase shift of about half a rotation. This segment most probably represents the case $A_1 \approx A_2$ (Eq. 35), where an abrupt $\Delta\phi_b = 0.5$ phase shift of the minimum occurs when the sum of two periodic signals goes to zero. Unfortunately, the gap in the data coincides with the hypothetical time interval of zero amplitude, and the n and ΔT values are too small for separating the two real periodic signals from each other. We encounter some similar cases in Sect. 9.5, where the entire segments are divided into two parts, and these shorter parts are analysed separately.

We conclude that both the 1P-model and the 2P-model fail. However, we get an accurate estimate for the location of the $z_C(f_1, f_2)$ minimum in Fig. A.58. Therefore, we use the period value $P_3 = (P_1 + P_2)/2$ in both Tables 7 and 9. Note that we also give the $M \pm \sigma_M$ value in Tables 7 and 9, but we do not give any A_3 , $t_{S,\min,1}$ or $t_{S,\min,2}$ values in Tables 7-10, because both of the 2P-model and the 1P-model fail.

We have no simultaneous TEL=2 data to check these results for DATA_{1,12}.

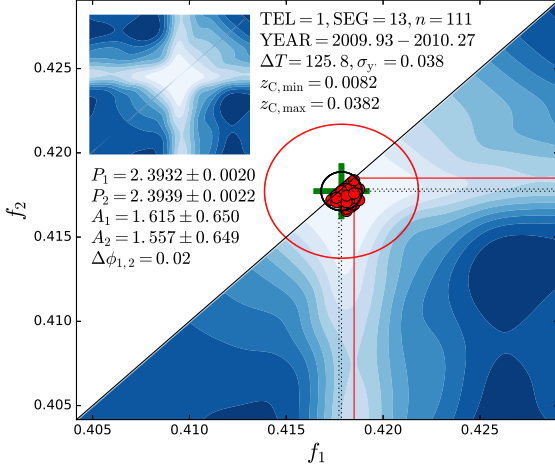


Fig. A.61. DATA_{1,13}. Otherwise as in Fig. 6

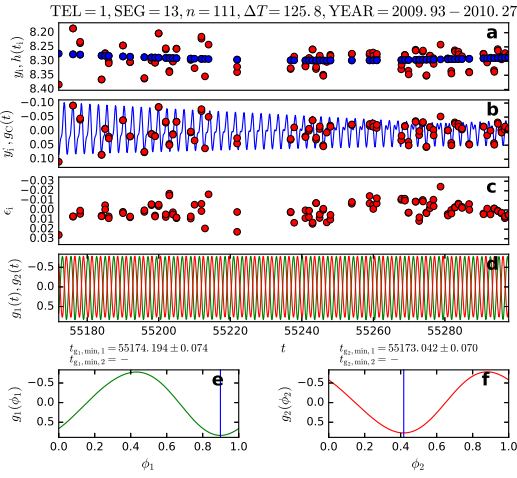


Fig. A.62. DATA_{1,13}. Otherwise as in Fig. 7

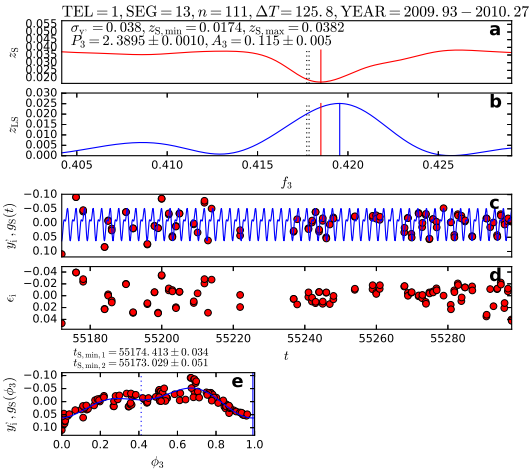


Fig. A.63. DATA_{1,13}. Otherwise as in Fig. 8

A.21. DATA_{1,13}

The $z_C(f_1, f_2)$ periodogram shows a hazy blue cross and light blue arms (Fig. A.61). The red lines denoting the frequency level $1/P_3$ of the best period of the 1P-model run through these arms. The best $g_C(t)$ model is so close to the diagonal line that this a clear CASE₁ break down, because the $\pm f_0/2$ and the $\pm 3\sigma_{f_1, f_2}$ limits hit $f_1 = f_2$. There is also strong amplitude dispersion. In this case, the conservative and the liberal model are the same: the 1P-model.

The light curve amplitude decreases during this relatively short segment (Fig. A.62a: $\Delta T = 125.8$). The small changes of the mean brightness can be modelled with a second order polynomial. The sample is small ($n = 111$) and there is a gap with only a few observations in the middle of the segment. The 2P-model can follow y_i amplitude changes (Fig. A.62b). The residuals in Fig. A.62c are very small ($z_{C,\min} = 0.0082$). The high amplitudes of the sinusoidal $g_1(t)$ and $g_2(t)$ signals make no sense (Figs. A.62edf).

The best periods detected with the 1P-method and the LS-method are different (Fig. A.63ab: blue and red vertical lines). The 1P-model can not adapt to the light curve changes, because residuals are larger in the end and beginning of the data (Fig. A.63cd). The $g_S(\phi_3)$ light curve has two minima (Fig. A.63e). Due to this double peaked shape, the LS-method detects a different period because the LS-model is a simple sinusoid.

Tables 7-8 and 9-10 give the same results for DATA_{1,13}, because conservative and liberal models are the same: the 1P-model. These results for DATA_{1,13} can not be checked with simultaneous TEL=2 data.